

**LITHOGRAPHICALLY MICROMACHINED SI/GLASS
HEAT EXCHANGERS FOR JOULE-THOMSON
COOLERS**

by

Weibin Zhu

A dissertation submitted in partial fulfillment
of the requirements for the degree of
Doctor of Philosophy
(Mechanical Engineering)
in The University of Michigan
2009

Doctoral Committee:

Professor Yogesh B. Gianchandani, Chair
Associate Professor Luis P. Bernal
Associate Professor Katsuo Kurabayashi
Associate Professor Euisik Yoon
Associate Professor Gregory N. Nellis, University of Wisconsin-
Madison

© Weibin Zhu

All rights reserved
2009

This dissertation is dedicated to my wife Feng Chen, who has always encouraged me to complete this challenge with unlimited support and love.

ACKNOWLEDGEMENTS

I would like to express my sincere gratitude and appreciation to my academic advisor Professor Yogesh B. Gianchandani for his support, encouragement and guidance throughout my masters and doctoral study at the University of Michigan-Ann Arbor. I thank him for introducing me to the MEMS area and providing me such a great opportunity to explore the cryogenic field. His patience and support helped me overcome many challenges in research and finish this dissertation. I also deeply indebted to my former and current committee members, Professors Khalil Najafi, Luis P. Bernal, Katsuo Kurabayashi and Euisik Yoon for their valuable discussion and insightful suggestions on my research work.

I sincerely appreciate Professor Sanford A. Klein and my committee member Professor Gregory F. Nellis, both from the University of Wisconsin-Madison, for their support and invaluable suggestions. I thank them for letting me participate in their group events and use their lab and equipment to finish our experiments. I am profoundly grateful to Michael Frank, Dan W. Hoch, Michael J. White, our colleagues from the University of Wisconsin-Madison, for their contribution and invaluable discussion on cryogenics. Very special thanks to Michael J. White for his help on both research and life when I was in Madison. I enjoyed those days and nights working in his lab and tackling problems side by side with him.

I would like to thank my former and current research group members, Shamus, Chester, Senol, Kabir, Tao, Bhaskar, Amar, Mark, Christine, Jong, Allan, Scott W., Scott G., Naveen and Karthik, and many students from other groups, Sang-Hyun, Sang-Won, Jae-Yoong, Neil, Jay, T. J., Andy, Burcu, Hanseup, Tzeno, Seow Yuen, Gayatri, Jianbai, Yuan, Wen-Lung, Yu-Wei, Jun Y., Meng-Ping, Linda, Yuhai, Xiaoyang, Dawen and Xin C., for all their support, encouragement, discussion and friendship. I would also like to thank Jun C., Zhijiang, Weihua, Shunjun, Angelo and many other friends along the way who are too numerous to name. Without them, my life in Ann Arbor would not have been so comfortable and enjoyable. I also want to thank my new friends met in Madison, including Kurt, Harrison, Jacob and Nick, for their support. Special thanks to many SSEL technical staff, including Ning, Katherine, Zeying, Greg, Brian, Tim and others for their help in clean room.

Additional thanks to all the technical and administrative staff from SSEL, WIMS and ME. My graduate study would not have been as smooth without their devoted service.

Finally, I sincerely thank my parents and my sister who have always cheered and encouraged me to reach every milestone in my life. This dissertation is also in memory of my grandmother who passed away in fall 2003 when I was taking the Ph.D. qualifying exam. Without her lifetime commitment to support me, I would not have achieved any of my goals and completed this program. And last but not least, I want to thank my wife Feng Chen for her enormous capacity to love and support. Without her, I could never have reached this day.

TABLE OF CONTENTS

DEDICATION	ii
ACKNOWLEDGEMENTS	iii
LIST OF FIGURES	ix
LIST OF TABLES	xv
LIST OF APPENDICES	xvi

CHAPTER

1. Introduction	1
1.1 Heat Exchangers for the Micromachined Joule-Thomson Coolers	3
1.1.1 Background of the Joule-Thomson Cycle.....	3
1.1.2 Advantages of Using Micromachined Heat Exchangers	5
1.1.3 Requirements for the Micromachined Heat Exchangers	7
1.1.4 State of the Art of the Micromachined Heat Exchangers	8
1.2 Overall Goals	11
1.3 Applications	15
1.3.1 Requirements for the Micromachined Joule-Thomson Coolers	15
1.3.2 Cryosurgery.....	17
1.3.3 Cooling Infrared Detectors in Space Applications	19
1.3.4 Night Vision Devices.....	20

1.4 Outline.....	20
2. Planar Design of the Micromachined Heat Exchanger	22
2.1 Design Concept.....	22
2.2 Numerical Model	26
2.2.1 Model Description	26
2.2.2 Optimization and Simulation Results	33
2.3 Device Fabrication	35
2.3.1 Fabrication Process	35
2.3.2 Related Fabrication Techniques.....	39
2.3.2.1 Wafer Bonding.....	39
2.3.2.2 DRIE Through-Wafer Etching.....	45
2.3.2.3 Electro-Chemical Discharge Machining (ECDM).....	50
2.3.2 Discussion in Fabrication.....	53
2.4 Experimental Results	54
2.4.1 Preliminary Tests	54
2.4.2 Self-Cooling Test.....	57
2.4.3 Discussion	59
3. Perforated Plate Design of the Micromachined Heat Exchanger	64
3.1 Design Concept.....	65
3.2 Numerical Model	69
3.2.1 Governing Equations	69
3.2.2 Model Description	74
3.2.2.1 Die Geometry.....	74

3.2.2.2 Thermal Conductivity	74
3.2.2.3 Laminar Flow Heat Transfer and Pressure Drop Correlations	75
3.2.2.4 Turbulent Flow Heat Transfer and Pressure Drop Correlations	77
3.2.2.5 Fin Effectiveness.....	78
3.2.2.6 Thermal Resistances	79
3.2.2.7 Axial Conduction	80
3.2.2.8 Parasitic Heat Loads	81
3.2.3 Design Geometries.....	82
3.3 Device Fabrication	82
3.3.1 Fabrication Process	82
3.3.2 Related Fabrication Techniques.....	85
3.3.2.1 KOH Etching on (110) Si Wafer	85
3.3.2.2 HF:HNO ₃ Glass Etching	88
3.3.2.3 Die-Level Si/Glass Stack Bonding	89
3.3.3 Discussion of Fabrication	92
3.4 Cryogenic Test Facilities	94
3.4.1 Schematics and Operation Modes.....	94
3.4.2 Major Components and Setups	99
3.4.3 Experimental Setup for Pt RTD Calibration.....	102
3.4.4 Improved Self-Cooling Setup	103
3.5 Experimental Results	104
3.5.1 Integrated RTD Calibration	104
3.5.2 Effectiveness Test	107

3.5.3 Self-cooling Test.....	110
3.5.4 Discussion	113
4. Flow-Controlled Joule-Thomson Cooling System	116
4.1 Concepts.....	116
4.2 Piezoelectric Microvalve	118
4.3 Experimental Setup.....	120
4.4 Experimental Results	123
4.5 Discussion.....	126
5. Conclusion and Future Work	128
4.1 Conclusion	128
4.2 Future Work	132
 APPENDICES.....	 135
 BIBLIOGRAPHY.....	 153

LIST OF FIGURES

Figure 1.1: Joule-Thomson cycle: (a) schematic diagram of the J-T cycle; (b) the T-s diagram of the J-T cycle with ethane as working fluid.	4
Figure 1.2: Photographs of micromachined coolers: (a) a two stage nitrogen/neon glass micro-cooler made by MMR, Inc. [MMR08]; (b) a micromachined ethylene Si/glass cold stage fabricated by Burger et al. [Bur01]; (c) four sizes of nitrogen micromachined glass J-T cooler [Ler06].	9
Figure 1.3: Benchmark of micromachined J-T coolers (modified from [Rad04]).	12
Figure 1.4: Benchmark of micromachined heat exchanger used in J-T coolers. Burger's cooler is treated as a J-T cooler to estimate the heat transfer per volume in its heat exchangers.	14
Figure 1.5: Photograph of the cryoablation of a cancerous tumor in the liver [Uni08].	17
Figure 1.6: Comparison of cooling performance and size of conventional J-T cryosurgical probes made of metals and existing micromachined coolers.	18
Figure 2.1: Fin rows structure of the planar micro heat exchanger.	23
Figure 2.2: Thermal conductivity of selected materials in the cryogenic temperature region [Fra04].	25
Figure 2.3: Fin row geometry of the planar design [Fra04].	28
Figure 2.4: Schematic of a generalized fin problem. Fluid flows through the fin and induces potentially large, axial temperature gradients in the x-direction when heat is also distributed from or to the base plate in the y-direction.	29
Figure 2.5: Cross section of two fin rows and base plate showing the energy flows.	30
Figure 2.6: Refrigeration as a function of mass flow rate for a fixed geometry and operating conditions. Note that as the mass flow rate increases, the refrigeration capacity of the cryogenic system first increases and then decreases.	34

Figure 2.7: Refrigeration load as a function of the base plate thickness for silicon, Pyrex, and a material with a conductivity of 30 W/m-K.	35
Figure 2.8: Fabrication process flow of the planar heat exchanger	36
Figure 2.9: Fabricated planar heat exchanger. a) The size of the planar micro recuperator is 60×15 mm ² with a total 2.5 mm thickness. The gap between each fin row is 51 μm. b) High pressure fin rows with 50 μm gap, fin size is 50×782 μm ² , 200 μm high. c) Low pressure fin rows with 345 μm gap. The fin size is the same as that of the high pressure fins.....	38
Figure 2.10: Polishing defects on the polished glass surface under microscope. The maximum diameter of the holes is more than 1 mm.....	40
Figure 2.11: Die-level glass fit bonding with commercial glass frit tape. Color of glass frit tape changes to dark green when the bonding is completed.	44
Figure 2.12: Wafer-level glass frit bonding. There are significant temperature gradients and cracks on the four inch wafer.	44
Figure 2.13: DRIE process when Si substrate is almost removed from the glass layer. The pattern is located in the center of the wafer.	46
Figure 2.14: Lateral Cross section A-A and Longitudinal cross section B-B. The lateral footing undercut X_c and longitudinal footing undercut Y_c are ideally symmetric on their cross section, thus $X_c = (W_t - W_b)/2$ and $Y_c = (L_t - L_b)/2$	47
Figure 2.15: SEM of fin rows after DRIE. a) Fin rows on low pressure side. b) Lateral undercut on a fin. c) Longitudinal undercut on the fins.....	47
Figure 2.16: Undercut beneath oxide layer. The oxide mask is transparent.....	48
Figure 2.17: Schematic diagram of the electrochemical discharge drilling setup. The material of the tool tip can be stainless steel, tungsten, platinum, etc.	50
Figure 2.18: SEM of an electrochemically drilled hole on a 350 μm thick Pyrex substrate.	51
Figure 2.19: Channel formed when the tool tip slides on the Pyrex substrate during the electrochemical discharge drilling	52
Figure 2.20: Photograph of ECDM setup	52
Figure 2.21: Inlet and outlet holes line up in a row on the Pyrex cap	53
Figure 2.22: Solid model of header/structural plate and planar heat exchanger.....	54
Figure 2.23: Ice bath test setup of the micro heat exchanger. The temperature measurements use Type E thermocouples.	55

Figure 2.24: Photograph of ice bath test setup (at UW-Madison).....	55
Figure 2.25: Photograph of test setup submerged in ice bath (at UW-Madison)	56
Figure 2.26: Helium flow rate measured by the inlet and exit flow meters as a function of the helium inlet pressure for the high and low pressure sides.	56
Figure 2.27: Helium exit temperature, relative to measured ice water temperature, as a function of flow rate (average measured by the inlet and exit flow meters) for the high and low pressure sides.	57
Figure 2.28: Self-cooling setup. Butane gas with regulated pressure is introduced from the inlet. The micro recuperative heat exchanger is mounted inside the header. The type E thermocouples are inserted into the high and low pressure taps to measure the gas temperature inside the tube (at UW-Madison).....	58
Figure 2.29: Temperature difference between the cold end and the inlet as a function of the orifice area for three different inlet pressures.	59
Figure 2.30: Temperature difference between the cold end and the inlet as a function of the inlet pressure for the 0.2mm ² orifice area.	59
Figure 2.31: Measured effectiveness based on hot side energy balance and the predicted effectiveness using the micro heat exchanger model as a function of the mass flow rate.	61
Figure 2.32: Measured and predicted low temperature (T ₃) for various values of parasitic heat loads as a function of the inlet pressure. The experiment is completed at ambient temperature at about 21 °C.....	62
Figure 3.1: Design geometries of (a) a single silicon plate, and (b) a single glass spacer.	65
Figure 3.2: Concept for (a) a single silicon plate, and (b) a single glass spacer.....	66
Figure 3.3: Mask layout of 10×10 mm ² die integrated with Pt RTDs.....	68
Figure 3.4: Silicon KOH mask and RTD mask layout of 10×10 mm ² die integrated with Pt RTDs.....	68
Figure 3.5: Location of nodes used for computational grid in heat exchanger numerical model.....	70
Figure 3.6: Energy balance diagram of (a) hot stream, (b) cold stream and (c) heat exchanger wall.	71
Figure 3.7: Four thermal resistances in serial for heat conduction between the hot and cold fluid streams.....	79

Figure 3.8: Fabrication process of the perforated plate Si/glass heat exchanger with Pt RTDs	84
Figure 3.9: Six (111) planes on a (110) wafer after KOH process. (a) the hole is self-terminated if the edges on the mask are too short; (b) the hole is etched through the wafer if the long edges on the mask are long enough.	86
Figure 3.10: Actual opening of the slots after KOH on a (110) wafer: (a) with mask and (b) without mask.	87
Figure 3.11: SEM photo of actual openings of the slot pattern after KOH.	87
Figure 3.12: Isotropic HF etching. x is the lateral undercut; t is the etch depth (wafer thickness in our case); W is the designed width; W_a is the actual width.....	88
Figure 3.13: Microscopic photo of a HF:HNO ₃ wet etching processed glass wafer bonded on a silicon substrate.	88
Figure 3.14: Heat exchanger boned by STYCAST 2850FT epoxy. The total length is about 2 cm (25 dies).....	90
Figure 3.15: A 1×1 cm ² heat exchanger (without Pt RTDs) fabricated by Si-Au eutectic bonding. The Dies with Pt RTDs are equally distributed across the entire length of the micro heat exchanger. The total length is about 1.6 cm (20 dies).	92
Figure 3.16: Flow schematic of the cryogenic test facility outside the dewar.....	93
Figure 3.17: Flow schematic of components inside the dewar. (a) Applied cooling mode. Helium gas is used as work fluid. $\Delta P_{12}=P_1-P_2$; $\Delta P_{34}=P_3-P_4$. (b) Self-cooling mode. Ethane is used as the work fluid.	94
Figure 3.18: (a) Side view and (b) top view of the cryogenic test facility..	97
Figure 3.19: Instruments inside the dewar.....	98
Figure 3.20: HC-2D compressor used in the cryogenic test facility (at UW-Madison) ...	99
Figure 3.21: Bronkhorst F-132M mass flow meter (at UW-Madison).....	99
Figure 3.22: Pressure regulator used in the experiments with inlet pressure lower than 80 psia (at UW-Madison).....	101
Figure 3.23: Pressure regulator used in the experiments with inlet pressure higher than 80 psia (at UW-Madison).....	101
Figure 3.24: A forty-three-die heat exchanger mounted on a pair of headers.	102
Figure 3.25: Setup for calibration of RTDs on a single die (at UW-Madison)	103

Figure 3.26: Photo of the experimental setup (inside the dewar) for self-cooling test (at UW-Madison)	104
Figure 3.27: Normalized resistance measurement of a Pt RTD on a 10 mm silicon perforated plate as a function of temperature. The temperature is simultaneously measured by a commercial PRT and a thermocouple. The measured resistance at room temperature (296.00 K from PRT, 295.79 K from thermocouple) is 4.287 KΩ. The sensitivity is 0.26%/K. Two measured lines are coincident.	105
Figure 3.28: Normalized resistances as a function of temperature for the Pt RTDs on the forty-three die 10 mm heat exchanger. The estimated temperature was calculated using Eq. (3.41). The legend shows which side of the heat exchanger the RTD is on, the number of dies the RTD is from the hot end of the heat exchanger.	107
Figure 3.29: Effectiveness measurement at cryogenic temperature range (237-252 K). Two independent sets of data are measured from thermocouples and PRTs. The effectiveness is defined as $(T_1-T_2)/(T_1-T_3)$ on high-pressure side and $(T_4-T_3)/(T_1-T_3)$ on low-pressure side.	108
Figure 3.30: The experimentally measured and numerically modeled temperature distributions at a) the lowest and b) the highest mass flow rates in self-cooling test for the forty-three die heat exchanger. Temperature distribution inside the heat exchanger is measured by integrated Pt RTDs.	109
Figure 3.31: Temperature drop at the orifice from inlet temperature as a function of pressure difference between inlet and outlet in the self-cooling test.	111
Figure 3.32: Transient temperature profile of the heat exchanger in J-T self-cooling test with 0.010 in. orifice.	112
Figure 3.33: Temperature drop at the orifice from inlet temperature as a function of heat load in J-T self-cooling test with 0.015 in. orifice.	112
Figure 4.1: Joule-Thomson cooling cycle with an active microvalve for gas expansion.	118
Figure 4.2: Piezoelectric microvalve design [Par08].....	119
Figure 4.3: Photos of (a) the piezoelectric microvalve and (b) valve seat structure. The overall size of the piezoelectric microvalve is $1\times 1\times 1\text{ cm}^3$	120
Figure 4.4: Photo of the flow modulation test for microvalve. (at UW-Madison).....	121
Figure 4.5: Schematic diagram and photo of test setup for the flow-controlled J-T cryogenic system inside the dewar.	122

Figure 4.6: Ethane mass flow rate as a function of pressure difference in valve characterization test and J-T tests. -30 V, 0 V, 30 V 60 V, 80 V and 100 V were used as input voltage. The mass flow rate is measured at room temperature in all tests.123

Figure 4.7: Temperature drop at the valve or orifice from inlet temperature as a function of pressure difference between inlet and outlet in the J-T test. Since the input voltage of the microvalve is -30 V to 100 V, the region between two dash lines is the temperature region that the J-T system can control at a given input pressure.124

Figure 4.8: Transient response of the J-T cycle when it is cooling down. The gas flow is shut off as the temperature reaches around 244 K at the HP outlet, which is very close to the microvalve. This is mainly due to the impurities freezing around the microvalve.125

LIST OF TABLES

Table 1.1: Comparison of micromachined heat exchangers for the J-T microcoolers	12
Table 2.1: Defined variables of planar design	28
Table 2.2: Different process conditions of Si bonding methods.....	42
Table 3.1: Summary of geometric parameters and operating conditions	82
Table 3.2: Properties of STYCAST 2850FT with catalyst 23LV.....	90
Table 3.3: Value of $C_{convert}$ of different gases at different pressures.....	101

LIST OF APPENDICES

Appendix A: Design, Fabrication and Tests of a 20 mm Perforated Plate Heat Exchanger	135
Appendix B: Misalignments and Defects in the KOH Process on a (110) Silicon Wafer	138
Appendix C: Pressure Drop Test of the Perforated Plate Heat Exchangers	143
Appendix D: Preliminary Results of a Cryosurgical Instrument Prototype	146
Appendix E: List of Publications Related to This Dissertation	152

CHAPTER 1

Introduction

In the past three decades, there have been widespread efforts to miniaturize cryogenic systems. Miniature cryogenic systems or coolers have potential impact on many different fields, such as cryosurgery, cooling infrared detectors in space applications, cooling night-vision devices for military purposes, cooling electronics for the improvement of signal to noise ratio and speed of systems, superconducting electronics, and more. Most of these applications require cryogenic temperatures below 200 K.

Thermodynamic cycles, including Joule-Thomson (J-T), Gifford-McMahon (G-M), pulse-tube, and Stirling cycles, are commonly used in cryogenic systems. Compared to other cooling techniques such as thermoelectric cooling, magnetic cooling, and others, thermodynamic cycles have high efficiency and can provide high cooling power. Among these, the J-T cycle is particularly suitable for miniaturization due to its simple structure and absence of cold moving parts. This thesis mainly focuses on J-T thermodynamic systems. In all instances, without alternative identification, the cryogenic systems or coolers described in this thesis will be referred to as thermodynamic cryogenic systems.

Cryogenic systems are usually fabricated with conventional metal processes

because most parts in these systems are made of metals such as oxygen-free high conductivity (OFHC) copper and stainless steel. The miniaturization is, therefore, limited by the resolution of those processes and the materials that can be processed. Recent developments in micromachining technologies have provided additional innovative methods to miniaturize the cryogenic system. The micromachined cryogenic system can be further scaled down in a mass production manner while its cooling performance can still meet the requirements of its corresponding applications. Because the materials used in micromachining technologies are generally lighter than metals, the overall weight of this system is thus reduced. Furthermore, integration of sensors and actuators, which requires more effort and cost in a conventional metal process, can be easily accomplished in the micromachining processes.

The heat exchanger, as the core component of miniature cryogenic systems, also can benefit from micromachining technologies. For example, microstructures inside the micromachined heat exchanger can significantly increase the heat transfer surface area and thus achieve higher efficiency than conventional heat exchangers with the same volume. In addition, materials such as silicon and glass, which are commonly used in micromachining technologies, provide better thermal properties than metals. Finally, sensors and actuators can be integrated into the heat exchanger in micromachining processes to achieve real-time measurements and temperature control. Several micromachined coolers [Lit82, Bur01, Ler07] including heat exchangers have been recently developed. In these systems, the overall cooling performance was investigated but detailed experimental analysis of the heat exchangers was not provided. Therefore, the design of their heat exchangers could not be validated. As the recuperative heat

exchanger design is the most important part of the J-T system, it requires considerable optimization and experimental validation based on design goals of its J-T system. This research effort proposes two generations of micromachined Si/glass heat exchangers used for miniature closed loop J-T cryogenic systems. Detailed design models, microfabrication processes and experiments provide insights into the heat exchangers in the J-T cryogenic systems.

The sequence of explanation in this chapter will include: Section 1.1, background of the J-T cycle, requirements and state-of-the-art of micro heat exchangers; Section 1.2, the overall goals of this effort; Section 1.3, several potential applications for a J-T system including this heat exchanger and Section 1.4. the outline of this thesis.

1.1 Heat Exchangers for the Micromachined Joule-Thomson Coolers

1.1.1 Background of Joule-Thomson Cycle

The Joule-Thomson cycle is widely used in many cryogenic applications. A schematic diagram of this cycle and its corresponding temperature-entropy (T-s) diagram for ethane are shown in Fig. 1.1. In this cycle, warm, high-pressure fluid at state (1) passes through a counter-flow recuperative heat exchanger, where it is pre-cooled by the low-pressure fluid returning from the refrigeration load. The cold high-pressure fluid leaving the heat exchanger at state (2) expands through a valve to state (3). The cold, low-pressure fluid is directed through the load heat exchanger where it is warmed by the refrigeration load to state (4) and then is fed back into the heat exchanger. The high-pressure inlet and low-pressure outlet of the J-T cycle can either link to a high pressure gas source and a ventilation system, respectively, to form an open J-T cycle, or connect to

a gas compressor to form a closed loop J-T cycle.

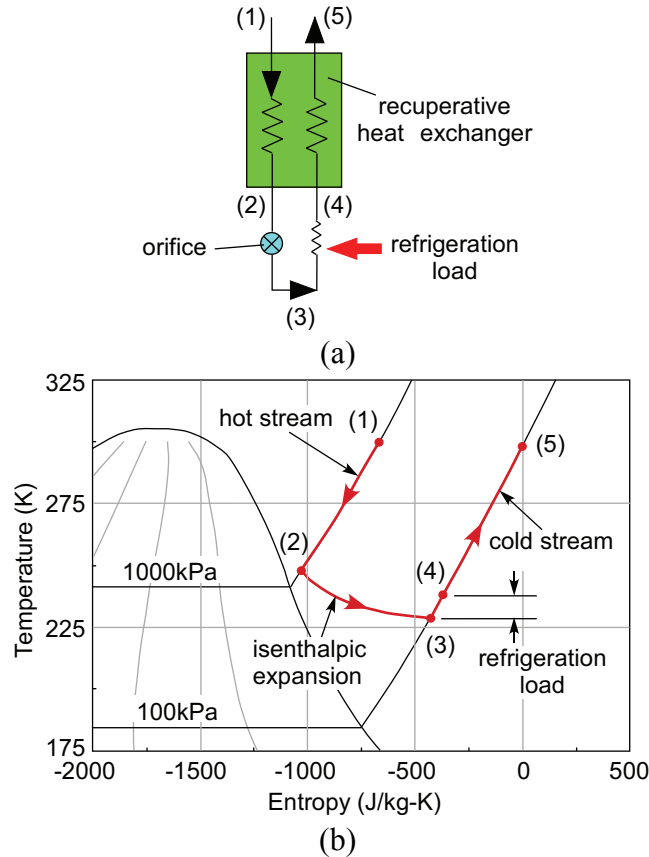


Figure 1.1: Joule-Thomson cycle: (a) schematic diagram of the J-T cycle; (b) the T-s diagram of the J-T cycle with ethane as the working fluid.

The J-T cooling cycle is particularly suitable for applications that demand fast cooling, moderate refrigeration capacity but with restrictions on size, space and structure. In addition, with a highly efficient counter-flow heat exchanger, the temperatures of fluid in both the inlet (state (1)) and the outlet (state (5)) of this cycle remain at room temperature. Bulky thermally insulated gas transfer lines are no longer necessary for connection between the J-T system and the gas supply. Finally, the J-T system has the potential for high reliability because there are no cold moving parts in the cycle. Accordingly, it is appropriate for applications that require high reliability for a long period of time during operation, for example, as in space applications. The structure of

the J-T cycle is simple enough to be fabricated with micromachining technologies and thus make the micromachined J-T cryogenic system possible.

1.1.2 Advantages of Using Micromachined Heat Exchangers

The smallest dimension of the channels in a typical micro heat exchanger is in the micrometer range. Another geometric characteristic of the heat exchanger is surface area density that is defined as the ratio of surface area to volume for one fluid (m^2/m^3). Compared to the traditional heat exchanger, micro heat exchanger has a large surface area density that is typically over $10000 \text{ m}^2/\text{m}^3$. Moreover, the surface area density increases as the channel size decreases in a heat exchanger. With silicon micromachined technologies, the channel size of the heat exchanger can be further scaled down to 10-50 μm range. Therefore, the surface area density of the micromachined heat exchanger can be dramatically improved. The micromachined heat exchanger has several advantages over the traditional heat exchanger.

1) The micromachined heat exchanger is more compact than the heat exchanger made by traditional metal processes because the extremely high surface area density in the micromachined heat exchanger substantially reduces the volume of the heat exchanger required for the same heat transfer power. For this reason, the total weight and volume of the material needed to manufacture the heat exchanger are significantly reduced. Furthermore, in a closed loop system, the total amount of fluid contained inside the system is reduced. This is very critical in some applications demands small size and weight of components, for example, space applications.

2) Lithographical process can achieve high-precision micro scale structures with a

relatively low cost in a mass production. A micro heat exchanger with accurately controlled geometries can be realistically manufactured, possibly even by more than one microfabrication processes. This provides more flexibility for design and fabrication of desired micro scale structures for high heat transfer efficiency. As will be discussed in this thesis, micromachining technologies allow us to design and fabricate highly efficient micro heat exchangers that provide unprecedented cooling capacities (on the scale of one watt or more) in the miniature J-T systems.

3) The micromachined structures can improve the overall heat transfer inside the heat exchanger due to high surface area density and new materials. Therefore, the effectiveness of the heat exchange is increased.

4) The dynamic response of the micromachined heat exchanger is much faster because the overall heat capacity is significantly reduced. Therefore, the system can reach steady state in a much shorter time (down to the minute range). Additionally, due to the thin interface between the two fluid streams, the transient temperature response of the fluid is also fast.

5) Sensors can be embedded into the heat exchanger for real-time measurements. Because the sensors can be integrated during the microfabrication process, the cost, size and weight of implementing sensors into the system are reduced.

In a J-T cooling system, the surface area and the channel size are not the only parameters that determine the performance the heat exchanger and the J-T system. As the channel size is reduced, the pressure drop across the heat exchanger is increased. When the pressure drop is too large, the cooling power provided by the J-T effect at the orifice or valve will be significantly reduced. Therefore, the surface density of the

micromachined heat exchanger for the J-T system is not necessarily over $10000 \text{ m}^2/\text{m}^3$ because this may require a very high input gas pressure due to the large pressure drop across the heat exchanger. The geometries of the heat exchanger have to be optimized to provide the maximum cooling power at a given working temperature. Details of this optimization will be discussed in Section 2.2 and Section 3.2.

1.1.3 Requirements for the Micromachined Heat Exchangers

In order for a micromachined J-T system to provide high cooling power at a cryogenic temperature, several major requirements for an efficient micromachined heat exchanger should be met.

1) Good stream-to-stream heat conductance between the high-pressure and the low-pressure channels. Materials and structures with high heat conductance between two streams are necessary. Moreover, structures with high heat transfer area to volume ratios are important for heat transfer between fluid and heat exchanger while pressure drops across the structures should be minimized.

2) Small stream-wise conduction inside the heat exchanger. Heat conduction along the fluid direction can reduce the temperature gradient between the cold end and the hot end. The temperature of the fluid before expansion is therefore high.

3) It is essential to select materials that have proper thermal properties to meet the heat transfer requirements and are compatible with the microfabrication process. Traditionally, Oxygen-Free High Conductivity (OFHC) copper and stainless steel are used to fabricate heat exchangers, but are not compatible with the microfabrication process. Fortunately, the thermal properties of silicon and Pyrex glass, respectively, are

reasonable substitutes for those of OFHC copper and stainless steel, and motivate the use of these materials for a micromachined heat exchanger. More details about the material selection will be discussed in Chapter 2.

1.1.4 State of the Art of the Micromachined Heat Exchangers

There are many different configurations for cryogenic heat exchangers used in the J-T cycle, including tubular exchangers, Giauque-Hampson exchangers, plate-fin exchangers, perforated plate exchangers, sintered metal powder exchangers, etc [Bar99]. However, not all of them are compatible with the micromachining technologies. Therefore, choosing an appropriate heat exchanger structure for microfabrication is critical.

In the early 1980s, Little reported a miniature glass J-T cooler (Fig 1.2a) that was lithographically fabricated [Lit82] and established MMR Inc. [MMR08] based on this technology. A planar counter-flow heat exchanger, which was constructed with groove structures on two glass substrates, was developed. With nitrogen gas, the system can reach 80 K with a cooling capacity of 250 mW when the inlet pressure is 100 atm. (10.1 MPa).

In the early 2000s, Burger et al. developed a silicon/glass cryogenic microcooler (Fig 1.2b) integrating the condenser, evaporator, flow restriction and counter-flow heat exchangers [Bur01]. Although the condensers and evaporator in this cooler are fabricated with silicon micromachining technologies, the heat exchanger is a tubular heat exchanger constructed with concentric glass tubes that are commercially available rather than with micromachining technologies. The system was tested with ethylene gas from

20 to 1 bar (2-0.1 MPa), and produced a cooling power of 200 mW at 169 K with a mass flow of 0.5 mg/s. Instead of operating in a single gas phase J-T cycle, this system operated in the vapor compression cycle, where the ethylene is condensed and evaporated. Subsequent experiments improved the system to reach 165 K [Bur01a].

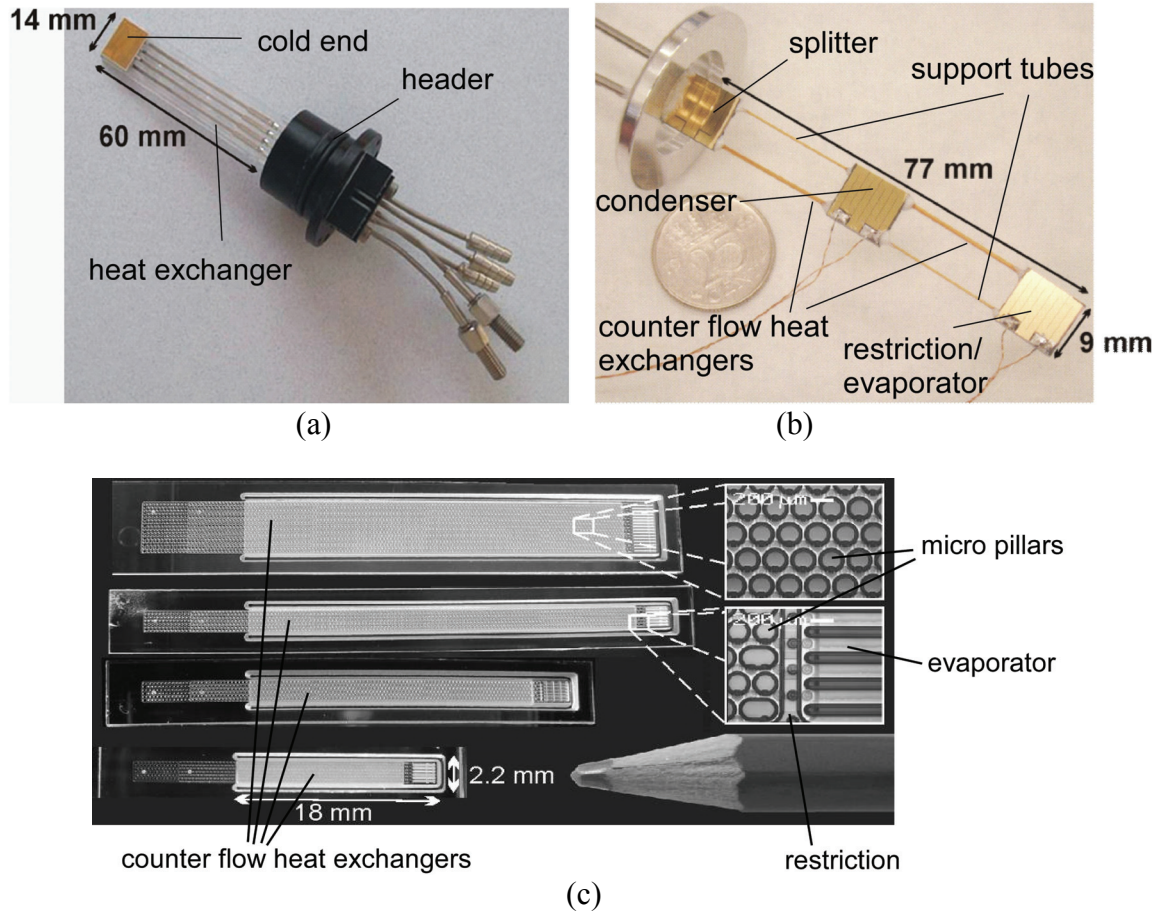


Figure 1.2: Photographs of micromachined coolers: (a) a two stage nitrogen/neon glass micro-cooler made by MMR, Inc. [MMR08]; (b) a micromachined ethylene Si/glass cold stage fabricated by Burger et al. [Bur01]; (c) four sizes of nitrogen micromachined glass J-T cooler [Ler06].

In 2006, Lerou et al. reported a micro J-T cryogenic cold stage (Fig 1.2c) fabricated with micromachining technologies [Ler06]. The planar heat exchanger in Lerou's cooler has an array of micro pillars fabricated inside the flow channels that increase the robustness and heat transfer area of the heat exchanger. Various sizes of this micro cold

stage are fabricated. It cooled down the system to 96 K with a cooling power ranging from 10 mW to 25 mW, when the inlet pressure of nitrogen is 80 bar (8 MPa).

In 2008, Bradley et al. reported a micro J-T cryocooler that supports on-chip cooling of high temperature superconducting electronics that require less than 5 mW of net refrigeration at about 80 K [Bra08]. The heat exchanger in this cryocooler is constructed with commercially available optical glass fibers. Gas mixture at 16-20 bar (1.6-2 MPa) inlet pressure will be used. In their design, a thermoelectric cooler is proposed to pre-cool the inlet fluid before it flow into the heat exchanger. Because this cooler is currently under development, the actual cooling performance of the cooler and its heat exchanger is not available. Therefore, it will not be included in the benchmarking of micromachined cryocoolers provided in the following sections.

The heat exchangers used in previously reported microcoolers were designed and optimized based on their target applications. However, detailed experimental analysis of the heat exchangers was not provided for validation of their heat exchanger designs. Only modest cooling power was achieved due to low mass flow rates. In addition, high inlet gas pressures (2-10 MPa) were used in their experiments to ensure that the cooling temperature and power were adequate. In fact, lack of efficiency in a heat exchanger can be compensated by a higher gas pressure, and the J-T system can still provide acceptable cooling. In the long term, the micromachined J-T cooler should be designed and fabricated to a closed loop system that includes a micromachined compressor. However, the gas pressure provided by this micro compressor can be limited to a range that is not higher than 1-2 MPa. Therefore, a highly efficient micromachined heat exchanger is desired to reduce the input gas pressure when providing enough cooling.

In order to facilitate precise temperature control, provisions for a feedback control scheme including real-time temperature sensing, control circuits and flow modulation can be added to the micromachined J-T system. While feedback control operation is beyond the scope of this thesis, the ability to achieve real-time temperature measurement using embedded sensors and flow modulation using microvalve will be demonstrated. More details about the real-time temperature measurement and flow modulation will be discussed in Chapter 3 and 4, respectively.

1.2 Overall Goals

The major focuses of this research effort are the design, fabrication and testing of micromachined Si/glass heat exchangers intended for use in miniature J-T cryogenic systems. The heat exchanger, which is fabricated in a lithography-compatible microfabrication process, should have high efficiency to provide high cooling power (in the W range) in the J-T cycle, when the inlet gas pressure is minimal (in the 1-2 MPa range). In addition, the heat exchanger must provide superb robustness and high reliability to be suitable for portable applications or space applications. The design specifications of our heat exchanger along with other existing micromachined J-T microcoolers are listed in Table 1.1. The specifications of Bradley's cooler listed in this table are the design goals as this cooler is currently under development. Figure 1.3 shows the refrigeration power as a function of temperature for different microcoolers and applications. Our target is to design and fabricate heat exchangers for J-T systems that can provide much higher cooling power than the existing microcoolers (1-10 watt), when the operating temperatures are from 200 K to 225 K.

Table 1.1: Comparison of micromachined heat exchangers for the J-T microcoolers

Author	Little	Burger et al.	Lerou et al.	Bradley et al.	Design goal of UM/UW J-T heat exchanger
Heat exchanger	glass channels	concentric glass tubes	glass pillars	glass fibers	Si/glass hybrid structure
Material	glass	Si/glass	glass	glass	Si/glass
Major fabrication	powder blasting	KOH wet etching	powder blasting dry etching/HF wet etching	commercially available optical fibers	Si dry/wet etching; HF glass wet etching
Effectiveness	unknown	unknown	unknown	unknown	>0.90
Overall size	$60 \times 14 \times 2 \text{ mm}^3$	$70 \times 9 \times 1.1 \text{ mm}^3$	$30 \times 2.2 \times 0.5 \text{ mm}^3$	$< 4000 \text{ mm}^3$	$35 \times 10 \times 10 \text{ mm}^3$
Integrated temperature sensing	No	No	No	No	Yes
Max. gas pressure	10 MPa	2 MPa	8 MPa	1.6-2 MPa	1-2 MPa
Cycle type/gases	J-T cycle, open loop/N ₂	vapor compression cycle, closed loop/ethylene	J-T cycle, closed loop/N ₂	J-T cycle, closed loop/gas mixture	J-T cycle, closed loop/ethane
Mass flow rate	2.5 mg/s	0.5 mg/s	1 mg/s	unknown	>250 mg/s
Performance in the J-T cycle	250 mW@80 K	200mW @ 169K	10-25mW @ 96K	9mW @ 80K (Target)	1-10W @ 200-225K (Target)

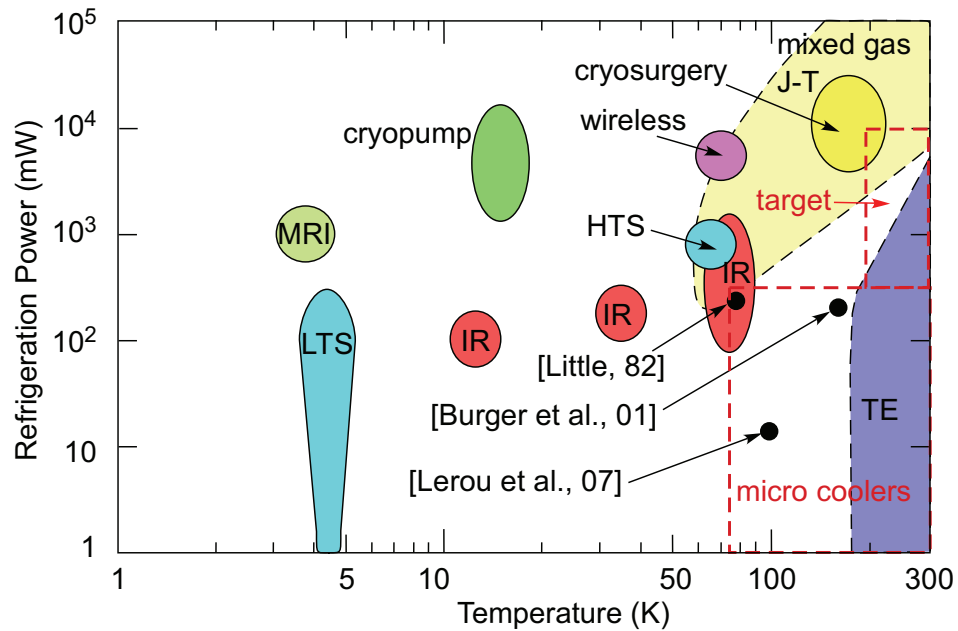


Figure 1.3: Benchmark of micromachined J-T coolers (modified from [Rad04]).

The glass heat exchangers in Little's and Lerou's J-T microcoolers can be categorized as plate-fin exchangers. The plate-fin exchanger is generally compatible with the surface or bulk micromachining technologies. The devices can be fabricated on a wafer or wafer stack and then diced to the target size. Carefully-designed glass structures were fabricated in both Little's (groove channels) and Lerou's (micro pillars) heat exchangers. Although the thermal conductivity of glass is large, a thin, but robust glass structure is able to provide enough heat transfer between the fluid streams to achieve high efficiency. Although the heat transfer between fluid streams and fin structures is large, silicon alone is not a suitable choice for a plate-fin exchanger due to its high thermal conductivity. It results in large axial conduction and thus small temperature gradient along the heat exchanger. A Si/glass hybrid planar structure was proposed in our initial stage of research to take advantage of the thermal properties of both silicon and glass. More details will be discussed in Chapter 2.

Perforated plate heat exchangers are also compatible with the micromachining technologies. The major challenge is to assemble the plates together with available bonding techniques. Traditionally, the plates are welded or soldered together, but this cannot be achieved when the heat exchanger is made of silicon or glass. However, this type of heat exchanger has very high efficiency and mass flow rate when the structure is very compact. A Si/glass perforated plate heat exchanger with high effectiveness was developed in the most recent stage of our research. The robustness and reliability of this design were significantly improved from the previous Si/glass planar design. Detailed design, fabrication and experiment results will be discussed in Chapter 3.

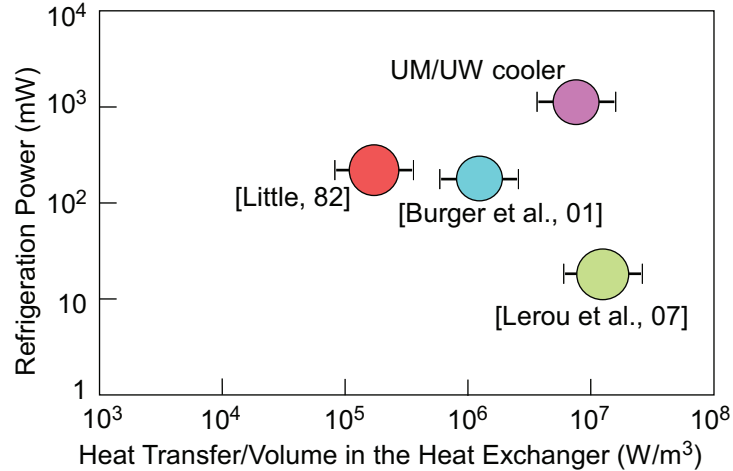


Figure 1.4: Benchmark of the micromachined heat exchangers used in the J-T coolers. Burger’s cooler is treated as a J-T cooler to estimate the heat transfer per volume in its heat exchangers.

Total heat transfer per unit volume in a heat exchanger is an important characteristic to describe the performance of the heat exchanger. Figure 1.4 shows the refrigeration power of the existing micromachined coolers as a function of heat transfer per unit volume in their heat exchangers. The estimated total heat transfer within the heat exchanger was calculated from mass flow rate, specific heat of the fluid (listed in Table 1.1) at the average temperature on the low-pressure side and the temperature difference between the inlet and outlet of the low-pressure side of the heat exchanger. Due to limited information found in the literatures, several assumptions were made for this calculation: a) the outlet temperature and pressure at the low-pressure side is 20°C and atmosphere unless specified; b) mass flow rate is constant in the J-T system, i.e. there is no external leakage; c) parasitic heat load in the heat exchanger is negligible for a simplified calculation. The volume of the heat exchanger in the calculation is estimated from the total size of the micromachined coolers. Figure 1.4 also shows the performance of our perforated plate heat exchanger. More details including design, fabrication and

experiments will be discussed in Chapter 3. As shown in Fig.1.4, the perforated plate heat exchanger can provide a large cooling power (in the watt range) when the heat transfer per unit volume is slightly less than Lerou's heat exchanger. Combining with the refrigeration power and the heat transfer per unit volume, our micromachined perforated plate heat exchanger demonstrates very promising performance and should be suitable for a wide range of cooling applications that require a large cooling power and a compact size.

1.3 Applications

Many applications demand a miniature J-T system. This section presents the general requirements for the micromachined J-T coolers in which our heat exchanger can be used, and three major applications, including cryosurgery, cooling infrared detectors in space applications and night vision devices. There are many other potential applications, including cryogenic electronics [Bru99], cooling superconductors [Rad04], measurement and characterization of materials and optical devices at cryogenic temperature [Mmr08], etc., that are beyond the scope of this thesis but invite future review.

1.3.1 Requirements for the Micromachined Joule-Thomson Coolers

There are several common requirements for a micromachined J-T cooler.

1) Low temperature: Many applications for miniature cryogenic systems require the system to achieve cryogenic temperature at 80 K or below while providing enough cooling power for their cooled objects. However, other applications require the system to operate at higher temperatures but provide more cooling power. For one example,

cryosurgery, it is well known that temperatures below 223 K (-50 °C) cause necrotic damage to pathological tissue [Gag76, Gag82, Bis93]. In this research work, we are targeting to a lower temperature range of 200-225 K.

2) Rapid cooling: A miniature J-T cooler can rapidly cool down the objects because the total thermal mass is reduced to a minimum. Moreover, a compact structure can potentially reduce the parasitic heat load and consequently further increase the cooling rate. In some applications that demand rapid cooling rates, this can be achieved by introducing more coolers, and thus, more total cooling power. However, this also increases the cost of manufacture and operation.

3) Compact size and light weight: The major reason for using a miniature J-T cooler is to reduce the size and weight to adapt to a variety of system needs. For example, space applications generally demand a highly reliable but very light and compact cryogenic system in order to reduce the cost of launching the system to the space. In this case, the total cost of launching the entire system dominates, and thus reducing size and weight of every component is critical. Other applications, such as cryosurgery and cooling night-vision devices, require the system to be portable. Cooling electronic circuits generally requires the system to be compact, and the cost of mass production to be as low as possible.

4) Sensor or actuator integration: In order to control the cryogenic system in a manner that the applications require, it is often necessary to integrate sensors or actuators in these compact systems. Temperature sensors, pressure sensors, flow sensors and active valves are commonly required components. Real-time measurements and control schemes are desirable.

1.3.2 Cryosurgery

In the past three decades, cryosurgery has been used to treat several types of cancers including prostate cancer, skin cancer, liver cancer. In this medical procedure, cancerous tumors are locally destroyed by exposing pathological tissues to repeated freeze/thaw cycles [Dob98]. Figure 1.5 shows a photograph of the cryoablation of a cancerous tumor in the liver. The ablated tissue is subsequently absorbed or sloughed by the body. By avoiding excision, operative blood loss and discomfort are minimized. Even in the cases where excision is required, the growth of tumor cells that might escape during resection can be prevented by a pre-treatment on the tumors with cryotherapy. Temperatures below -50°C are known to be necrotic for pathological tissue. In addition, a rapid cooling rate [Dob98, Gag85] between $25\text{-}50^{\circ}\text{C}/\text{min.}$ and multiple freeze-thaw cycles [Gag92] are preferred to decrease the likelihood of cell survival.

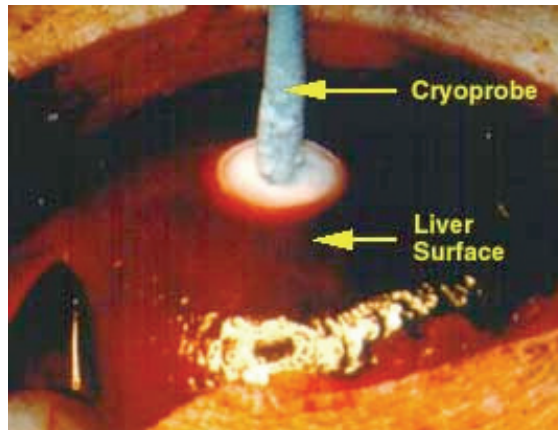


Figure 1.5: Photograph of the cryoablation of a cancerous tumor in the liver [Uni08].

Cryosurgery has been a standard treatment for cancerous tumors located in easily accessible areas of the body. Recent development of miniature cryoprobes with large refrigeration capacity [Cha93, May98, Dob94] and techniques for real-time monitoring using ultrasound or magnetic resonant imaging [Mat92, Rub93, Pea95] allow

cryosurgical techniques to be extended to the treatment of cancers in areas that are not readily accessible [Coh94]. In fact, the rationale for fabricating a micromachined J-T cryogenic system has been motivated in part by the need to miniaturize cryoprobes to a size that permits them to be inserted through a small incision. However, the performance of this system must not be compromised in this scaling effort because the freeze region that surrounds the cold end of the probe is controlled by the refrigeration power and surface temperature attainable by the tip of the probe.

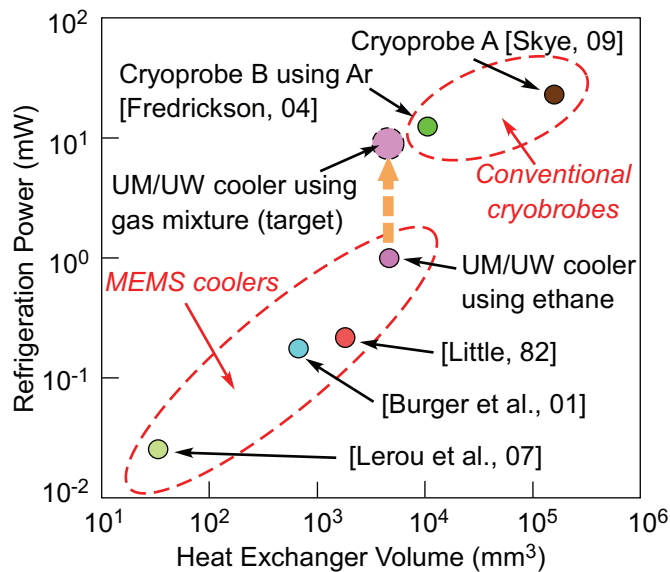


Figure 1.6: Comparison of cooling performance and size of conventional J-T cryosurgical probes made of metals and existing micromachined coolers.

Figure 1.6 compares the cooling power and size of the commercial cryoprobes and existing micromachined coolers. The cooling performance of the cryoprobe A manufactured by American Medical System, Inc. was measured by Skye at the University of Wisconsin-Madison while the gas mixture used in this system is known [Sky09]. The cooling power of the cryoprobe B manufactured by Endocare Inc. was measured by Frerickson at the University of Wisconsin-Madison [Fre04]. Argon gas at 2000 psia (13.8 MPa) is used in this system. Because the cooling power of a cryogenic system

varies at different temperatures and in different experimental conditions, this plot only provides a brief comparison between cooling performance and size of these existing coolers. In a J-T system, our micromachined heat exchanger is capable of providing cooling power in watt range while the size is one order magnitude smaller than the commercial probes. Most existing micromachined cryocoolers have limited cooling powers for this application although the size is even smaller. The cooling performance of our heat exchanger can be further improved by as many as one order magnitude by using optimal gas mixture at higher gas pressures. In the long term, this device will be very promising in cryosurgical applications.

1.3.3 Cooling Infrared Detectors in Space Applications

Infrared detectors are widely used for remote sensing in space satellites and airplanes [Col00, Kla00, Bra02]. In the last two decades, several NASA missions have been targeted monitoring of the earth's natural environment. For example, AQUA, the second mission of NASA's Earth Observing System, the Atmospheric Infrared Sounder (AIRS) has been used for temperature mapping of the earth. These detectors usually image the surface of the earth in near infrared (NIR) and mid -infrared (MIR) range. However, due to the low altitude orbits of these satellites, the large thermal flux emitted by the earth increases the noise. Consequently, a cryogenic system is necessary to cool down the detector to 150 K or below to improve the signal to noise ratio.

In space applications, the size and weight of the cryogenic system is critical as launching such systems is very expensive. A micromachined J-T system is desirable although the fabrication cost of such a single system is high. Furthermore, sensors and

actuators can be integrated into the system during the microfabrication. Installation of external temperature and pressure sensors into a compact cryogenic system can thus be bypassed.

1.3.4 Night Vision Devices

Night vision goggles using thermal imaging techniques are mostly used for military purposes. These devices use infrared detectors to gather infrared light and amplify it. Many can detect the targets at a temperature range of $-20\text{ }^{\circ}\text{C}$ to $2000\text{ }^{\circ}\text{C}$. In order to improve the signal to noise ratio and produce high resolution images, the advanced models generally utilizes a cooling system to reduce the temperature of the detectors below $0\text{ }^{\circ}\text{C}$. For this reason, a portable cooling system that can be mounted to the goggles would address pragmatic needs. This is very similar to cooling the infrared detector in space applications, but requires less cooling power and higher cooling temperatures, when the size and weight are small enough for portable applications. Also, the reliability requirements for such a portable device are different.

1.4 Outline

As mentioned earlier, the major goal of this research is to design and fabricate a highly efficient micro heat exchanger that is suitable for micromachining. The heat exchanger is used in the J-T cycle and can be potentially integrated into a micromachined J-T cooler. Chapter 2 describes a planar design of the recuperative heat exchanger for the J-T cooler. Design, modeling, fabrication and preliminary tests of this device are presented. Then, the experimental results and drawbacks of this design are discussed.

Chapter 3 describes a perforated plate design of the recuperative heat exchanger that may overcome some of the disadvantages of planar design and result in much better cooling performance. Design, model and fabrication of this heat exchanger are reported in detail. A comprehensive cryogenic test facility is developed and the experimental results from this test setup are reported. Chapter 4 explains a concept of integrating a heat exchanger and a normally open piezoelectric microvalve in a J-T system in order to provide precise flow and temperature control. The preliminary experimental results in this J-T system are reported. Conclusions and future work are discussed in Chapter 5.

CHAPTER 2

Planar Design of the Micromachined Heat Exchanger

In this chapter, a planar design of the micromachined Si/glass heat exchanger is described¹. Section 2.1 gives the conceptual details of the design. The planar, micromachined counter-flow heat exchanger uses rows of fins that are composed of high conductivity silicon that is anodically bonded onto a very thin base plate composed of low conductivity Pyrex. Heat is conducted through the thin Pyrex base plate from the hot stream to the cold stream. Section 2.2 summarizes a numerical model developed by collaborators from the University of Wisconsin-Madison and the optimization results we have compiled. Section 2.3 is a detailed discussion of the fabrication process of this heat exchanger and the existing challenges in the process. Section 2.4 provides the final experimental results with a discussion and recommendations for improvement of this design.

2.1 Design Concept

One of the critical challenges in developing a micromachined Joule-Thomson cooler is that the recuperative heat exchanger must maintain good stream-to-stream heat

¹ Portions of this effort were reported in abstract form in [Zhu05, Zhu06, Zhu07]

conductance while restricting parasitic stream-wise conduction losses. This results in a large enthalpy difference between the two streams and thereby achieves high cooling performance for the probe. Axial conduction can be very detrimental to the heat exchanger. The temperature of the fluid must drop very rapidly along the length of the recuperative heat exchanger. If axial conduction is not controlled, the refrigeration power delivered to the tip will be reduced dramatically.

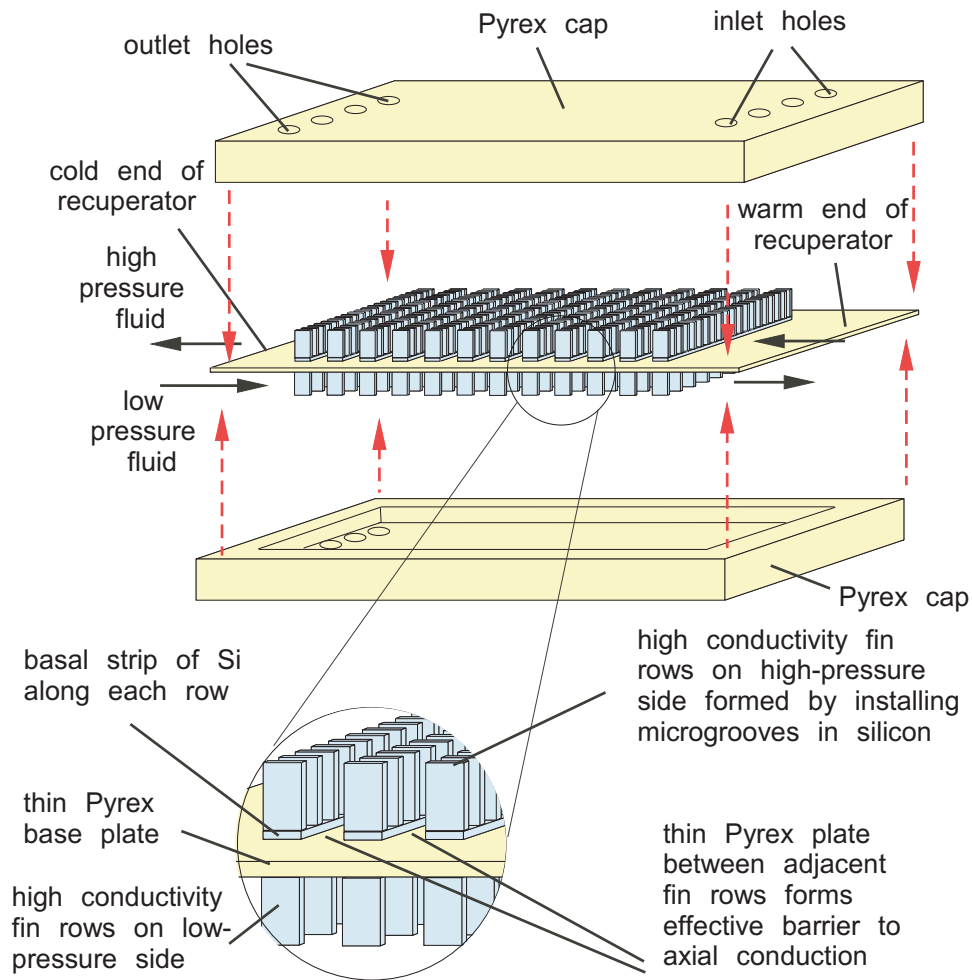


Figure 2.1: Fin rows structure of the planar micro heat exchanger.

The planar, micromachined recuperative heat exchanger shown in Figure 2.1 uses rows of fins that are composed of high conductivity silicon that is anodically bonded onto

a very thin base plate composed of low conductivity Pyrex. There is one array of fin rows on the high pressure side of the flat plate heat exchanger and a matching array on the low pressure side. The high- and low-pressure silicon fin rows communicate thermally across a thin layer of Pyrex while adjacent fin rows are thermally isolated by the Pyrex spacer along the flow direction in order to minimize the stream-wise conduction losses.

The major advantages of this planar heat exchanger design are listed as follows:

1) High surface area to volume ratio: A high aspect ratio silicon fin structure with a small feature that can be achieved by silicon dry etching technologies. Accordingly, a high surface area to volume ratio can be obtained to allow the heat exchanger to be very compact.

2) Low axial conduction: The Pyrex base plate has a relatively low thermal conductivity compared to silicon or other metals (approximately 1 W/m-K). The axial conduction between silicon fin rows that are separated by the Pyrex spacers will be minimal. Low axial conduction results in a high axial temperature gradient along the heat exchanger and thus a high effectiveness recuperative heat exchanger. This high effectiveness heat exchanger will result in a cooler that can provide more refrigeration power.

3) High heat transfer coefficient: The heat transfer coefficient is inversely proportional to the hydraulic diameter of the individual channels, which can be made very small through a microfabrication process.

4) Low pressure loss: Each fin row that is composed of multiple channels has a relatively large hydraulic diameter. This results in a relatively low pressure drop across

the heat exchanger.

5) Rapid cooling: The size and thermal mass of the heat exchanger will be very small because of the high surface area to volume ratio and the high heat transfer coefficients. As a result, the time needed to cool down a target to the required temperature is short.

6) Small discrete plate penalty: Each fin row base will be approximately isothermal in the axial direction due to the high thermal conductivity of silicon separated by the low thermal conductivity of Pyrex. This indicates that each fin row has a maximum thermal effectiveness of approximately 50%. Thus, the maximum theoretical effectiveness of the heat exchanger is related to the total number of fin rows in the heat exchanger. Since a large number of fin rows can be fabricated with microfabrication techniques, the penalty is kept to a minimum.

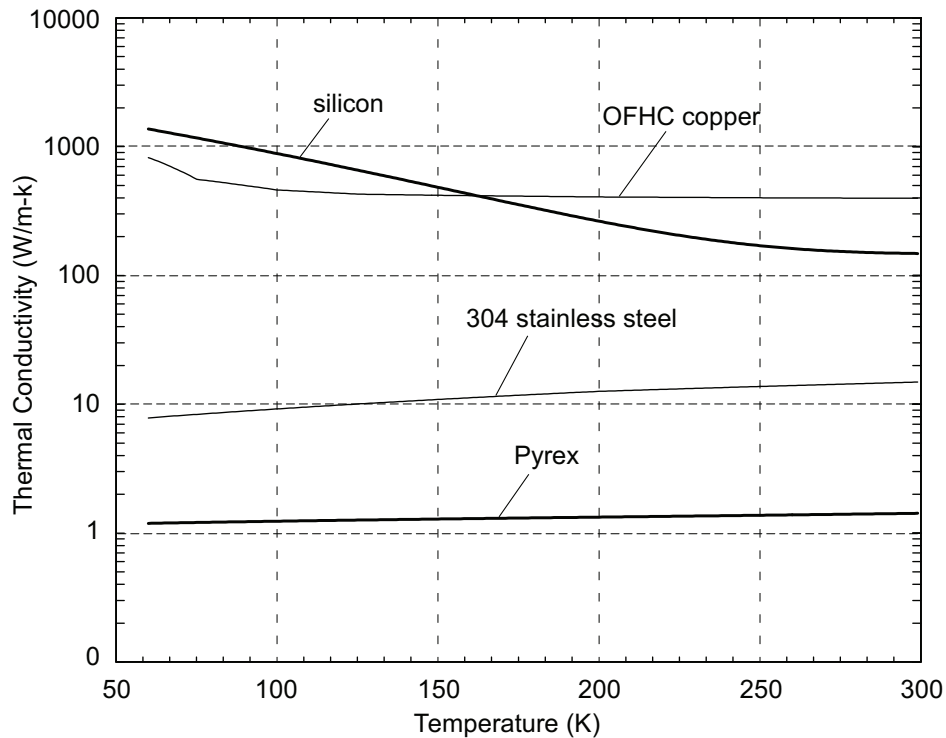


Figure 2.2: Thermal conductivity of selected materials in the cryogenic temperature region [Fra04].

7) No fluid-to-fluid seals: Because the two streams are isolated by the Pyrex base plate, fluid-to-fluid leaking will not occur between streams unless the base plate is damaged.

This design is in contrast to conventional cryogenic heat exchangers that use either perforated plate designs with oxygen-free high conductivity (OFHC) copper plates interleaved with stainless steel spacers or finned tube designs that use one or more finned tubes wound on a mandrel. Figure 2.2 shows the thermal conductivities of silicon and Pyrex compared to copper and stainless steel. Silicon has thermal conductivity that is similar to OFHC copper, and Pyrex has thermal conductivity that is an order of magnitude less than stainless steel; this combination of very high and low thermal conductivity suggests that a silicon and Pyrex composite heat exchanger would be attractive.

2.2 Numerical Model

2.2.1 Model Description

The planar miniature heat exchanger model was developed by Frank et al [Fra04]. from the University of Wisconsin-Madison and implemented using the computer program Engineering Equation Solver (EES) [Kle02]. This section summaries Frank's numerical model and presents its important simulation results. More details can be found in [Fra04]. The code simulates a composite silicon/Pyrex recuperative heat exchanger using a finite difference approach. The heat transfer associated with each heat exchanging fin is complicated and includes temperature changes in the fluid due to its finite capacity and two-dimensional conduction within the fin. The heat transfer problem has been

nondimensionalized and numerically solved; the results have been fit to a physics-based but approximate equation in order to characterize the performance of each fin in the heat exchanger model. The equations for each fin are numerically interfaced via appropriate energy balances and the resulting set of equations is solved simultaneously.

In Frank's model, a set of geometric parameters is defined for the heat exchanger as listed in Table 2.1. This includes the number of fin rows (G), the axial length of the fins (w), the axial length of the space between fins (w_{space}) and the thickness of the base plate (ΔBP). Different fin geometry on the high- and low-pressure side of the exchanger has to be specified, including the size of the gap between the fins within a fin row (s), the height of the fins (L), and the thickness of the fins (t). Because the low-pressure side of the heat exchanger tends to have a larger volume due to the lower density of the working fluid. Hence, a larger gap between channels in each fin row on the low pressure side is required. Moreover, the number of fins in each high pressure fin row (X_H) has to be specified in order to fully define the geometry and sets the overall width of the heat exchanger (w_{tot}).

$$w_{tot} = (s_H + t_H)X_H \quad (2.1)$$

where the subscript H stands for the high pressure side of the heat exchanger. Similarly, subscript L in those parameters stands for the low pressure side of the heat exchanger. Figure 2.3 shows some of the definitions for each fin row. Table 2.1 also gives the values for the baseline geometry in the simulation. All of the results in this section are based on this geometry. The geometry presented below is the preferred geometry after taking the entire design process into account. However, the actual geometries of the device are modified according to the microfabrication limits and will be discussed in Section 2.4

Table 2.1: Defined variables of planar design

Variable	Value	Description
\dot{m}	0.2 g/s	Mass flow rate
T_{in}	290 K	Temperature of incoming fluid
T_{ref}	150 K	Refrigeration temperature
$P_{H,l}$	1500 kPa	Pressure entering the high pressure side
G	60	Number of fin rows
w	782 μm	Axial length of fins
w_{space}	50 μm	Axial length of space between fin rows
ΔBP	100 μm	Thickness of the base plate
s_H	50 μm	Gap between high pressure fins
s_L	345 μm	Gap between low pressure fins
t_H	50 μm	Thickness of high pressure fins
t_L	50 μm	Thickness of low pressure fins
L_H	200 μm	Height of high pressure fins
L_L	200 μm	Height of low pressure fins
X_H	100	Number of high pressure fins in a row
L_{tot}	60 mm	Total Length of heat exchanging material
w_{tot}	15 mm	Total width of heat exchanging material
H_{tot}	2.5 mm	Total Height of heat exchanging material

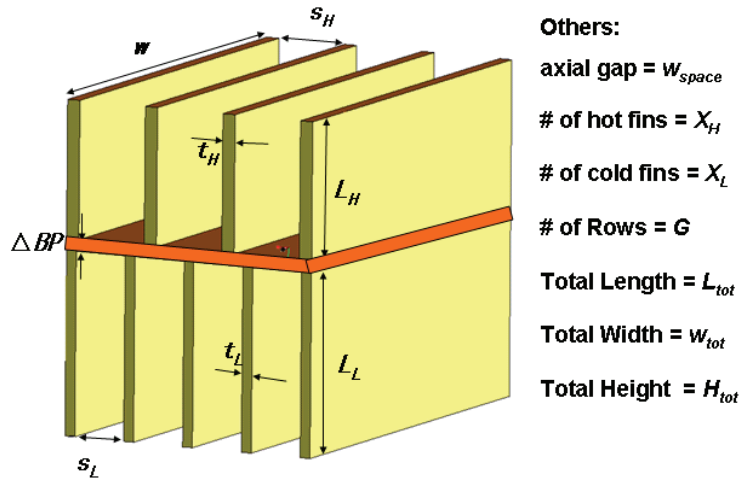


Figure 2.3: Fin row geometry of the planar design [Fra04].

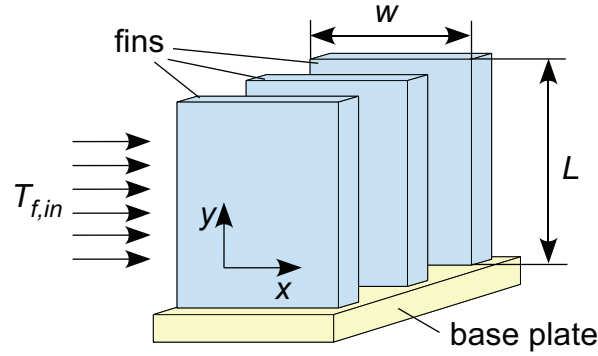


Figure 2.4: Schematic of a generalized fin problem. Fluid flows through the fin and induces potentially large, axial temperature gradients in the x -direction when heat is also distributed from or to the base plate in the y -direction.

The number of fins in each low pressure fin row (X_L) follows from the overall width of the heat exchanger which can be derived from Equation (2.2). The number of fins that can be installed in the low pressure side is related to this width and the low pressure fin geometry:

$$X_L = \frac{w_{tot}}{s_L + t_L} \quad (2.2)$$

The micromachined recuperative planar heat exchanger will utilize relatively long, thick fins that have an essentially uniform base temperature, as shown in Figure 2.4. These fins have a two-dimensional temperature distribution due to the finite heat capacity of the fluid and the resistance to heat transfer by conduction within the fin in both the x and y directions (see Figure 2.4). The fluid enters the fin with a uniform temperature ($T_{f,in}$), based on the assumption that the fluid completely mixes between fin rows. The fluid travels through the fin row in the axial direction (x). The fin accepts heat from the fluid and conduction occurs in both the axial and lateral directions (y). The base of the fin is assumed to be at a uniform temperature, essentially assuming that no temperature gradient can be developed axially in the Pyrex that separates the hot and cold fin rows.

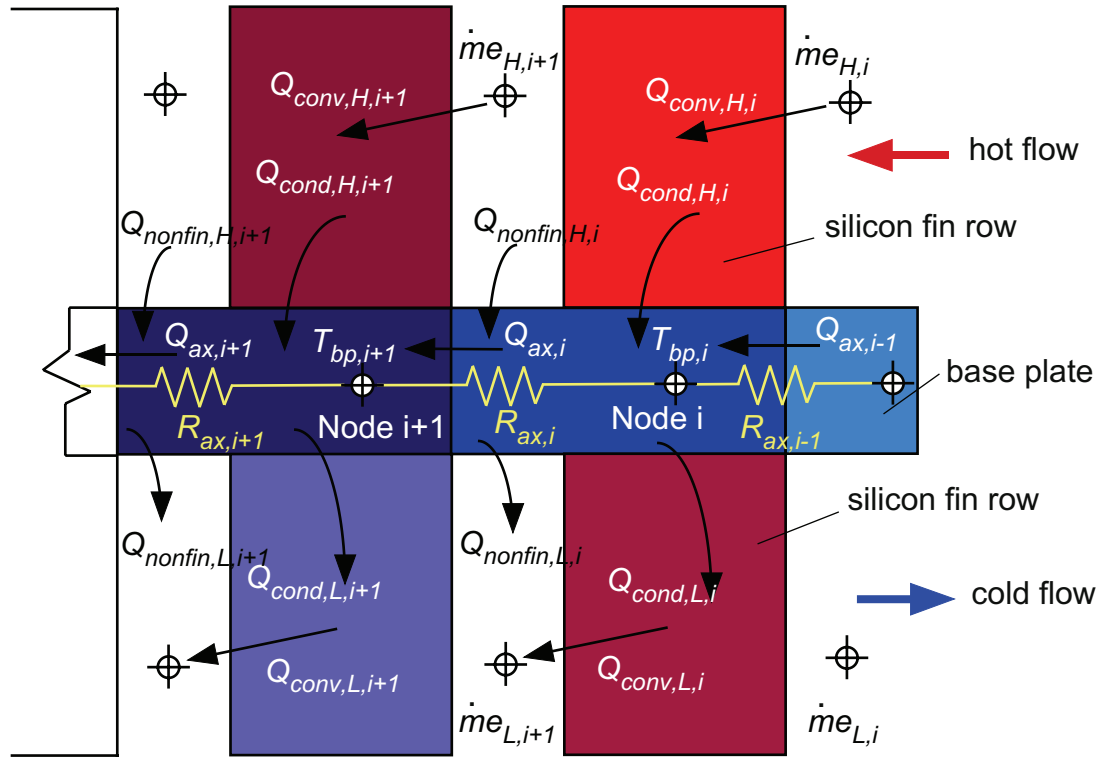


Figure 2.5: Cross section of two fin rows and base plate showing the energy flows.

The energy interaction between the fluid and Pyrex temperatures is governed by energy balances modeled using the grid shown in Figure 2.5. Energy is transferred into each node (i.e., each section of the base plate shown in Figure 2.5) as a result of conduction from the hot-side fin row, convection from the space between the fin rows on the hot side, and conduction coming from the adjacent fin row at a hotter location. Energy is transferred out of each node by conduction to the fin row on the cold side, conduction through the base plate to the adjacent fin row at a colder location, and convection coming from the space between the fin rows on the cold side. The surface area for heat transfer on each fin row is approximately 100 times as large as the surface area between the fin rows and consequently, the energy transfers related to the spaces between fin rows are ignored as they are negligibly small relative to the other terms.

Ultimately, the heat transfers that occur within each fin row can be modeled using the resistance network shown in Figure 2.5.

The energy balance for a node is therefore:

$$\dot{m}(e_{H,i} - e_{H,i+1}) + \frac{T_{bp,i-1} - T_{bp,i}}{R_{ax,i-1}} = \dot{m}(e_{L,i} - e_{L,i+1}) + \frac{(T_{bp,i} - T_{bp,i+1})}{R_{ax,i}} \quad \text{for } i=1:G \quad (2.3)$$

where R_{ax} is the resistance to axial conduction in the Pyrex, the e_H and e_L terms are enthalpies on the high and low pressure sides respectively, and G is the number of fin rows. The axial resistance can be determined in terms of the heat exchanger properties, as shown in Equation (2.4):

$$R_{ax,i} = \frac{2w_{space}}{(k_{bp,i} + k_{bp,i+1})w_{tot}\Delta BP} \quad \text{for } i=1:G \quad (2.4)$$

w_{space} is the axial distance between fins, and k_{bp} is the local thermal conductivity of the base plate material. The model assumes that the ends of the heat exchanger are adiabatic; it is also assumed that below each fin row the temperature is uniform translating into no axial temperature distribution in the base plate below each fin row. This assumption is valid because the thermal conductivity of the silicon fins is much higher than the thermal conductivity of the Pyrex base plate. This leads to the assumption that only the spaces between fins are used to conduct heat from row to row.

The pressure drop (δP) is calculated for the mixture passing through each fin row on the high and low pressure sides. By taking the hydrodynamic entrance length into consideration an average friction factor can be found for each fin row. First the hydrodynamic entrance length is found using the non-dimensional axial length defined below where x^+ is the hydrodynamic axial distance.

$$x^+ = \frac{x}{D_h \text{Re}} \quad (2.5)$$

Re is the local Reynolds number of the fluid. For rectangular ducts, Shah and London [Sha78] suggest a hydrodynamic entrance length of $L_{hy}^+ = 0.0328$. Two friction factors are determined, one for the entrance region, f_{ent} , and one for the developed region, f_{dev} . These two friction factors are averaged to estimate the actual average friction factor in a fin row. In the developed region, the friction factor is estimated using the equation for fully developed flow in rectangular channels from Shah and London:

$$f_{dev} = \frac{24 \cdot (1 - 1.3553\alpha + 1.9467\alpha^2 - 1.7012\alpha^3 + .9564\alpha^4 - .2537\alpha^5)}{\text{Re}} \quad (2.6)$$

where Re is the highest Reynolds Number of the fluid as it flows within the fin passages, and α is the non-modified aspect ratio of the channel. The friction factor in the developing region, f_{ent} , is estimated using two dimensional interpolation from a table proved by Shah and London for developing laminar flow in rectangular channels. These two friction factors are averaged using Equation (2.7)

$$f = f_{ent} \frac{w_{ent}}{w} + f_{dev} \frac{w - w_{ent}}{w} \quad (2.7)$$

The pressure drop can be found using the definition of the friction factor and adding an expansion/contraction loss for each row.

$$\delta P = \left(\frac{f \cdot w}{D_h} + 1 \right) \cdot \frac{\rho_{liq} \cdot v^2}{2} \quad (2.8)$$

In this equation, δP is the pressure drop associated with each fin row, ρ_{liq} is the liquid density of the work fluid and v is the local velocity of the mixture (calculated in Equation (2.9)).

$$v = \frac{\dot{m}\mu}{\rho D_h} \quad (2.9)$$

where ρ is the local density of the work fluid and μ is the local viscosity of the work fluid. At the hot inlet to the heat exchanger the work fluid will start in the gas phase and proceed into the two phase region as it is cooled. The liquid density is used in Equation (2.8) because it is conservative; it results in the largest pressure drop in the heat exchanger. The pressure drop in a two phase flow system is generally higher than in a single phase system but two phase pressure drop correlations are difficult to introduce because they are unstable. We use the liquid density throughout the heat exchanger for the pressure drop calculations as a conservative estimate.

2.2.2 Optimization and Simulation Results

The model was verified using several techniques. For example, that $T_{f,i}$ (the temperature of the fluid entering each hot fin row) is always greater than $T_{b,i}$ (the temperature of the Pyrex base of that fin row), and $T_{b,i}$ is always greater than $T_{f,c,i}$ (the temperature of the fluid entering the corresponding cold fin row). In this case, the heat always flows from the hot side to the cold side and the fin effectiveness calculations are self-consistent. In addition, all of the properties and variables that change in a continuous manner along the length of the heat exchanger were verified. For example, the velocity of the high pressure stream should slowly and smoothly, but monotonically, decrease as it gets colder.

In a real heat exchanger, as the mass flow rate (\dot{m}) increases, the refrigeration power should go from a negative number (at zero mass flow rate, the heat exchanger is just a conduit for conductive heat transfer to the load) and increase, eventually reaching a

maximum value after which the performance will decrease due to decreasing thermal effectiveness. A sample calculation was carried out using the model when assuming a reasonable geometry with a varying mass flow rate. The refrigeration as a function of mass flow rate is shown in Figure 2.6.

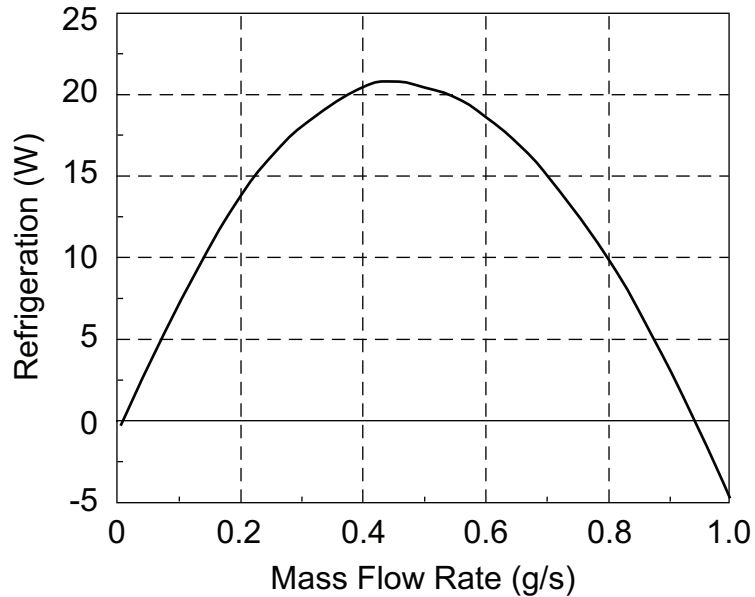


Figure 2.6: Refrigeration as a function of mass flow rate for a fixed geometry and operating conditions. Note that as the mass flow rate increases, the refrigeration capacity of the cryogenic system first increases and then decreases.

Initially, a 120 μm Pyrex plate as the base plate material was proposed. Pyrex was chosen because of its extremely low thermal conductivity, which minimizes the axial conduction along the length of the heat exchanger. However, the base plate must also allow heat transfer from the hot to the cold fluid in a direction perpendicular to the flow. If the material were a perfect insulator, the regenerator would not function. Our calculations showed that the refrigeration capacity with a 120 μm Pyrex base plate was not adequate for a surgical application because the Pyrex was preventing heat transfer between the hot and cold fluids. Thus, the thickness of the Pyrex may be reduced,

thereby, decreasing the thermal resistance of the Pyrex itself. Figure 2.7 shows the refrigeration load as the base plate thickness changes; both silicon and Pyrex base plates are considered in Figure 2.7 as both materials are easily joined and micromachined. The result for a material with an optimal constant thermal conductivity of 30 W/m-K is also shown in this figure.

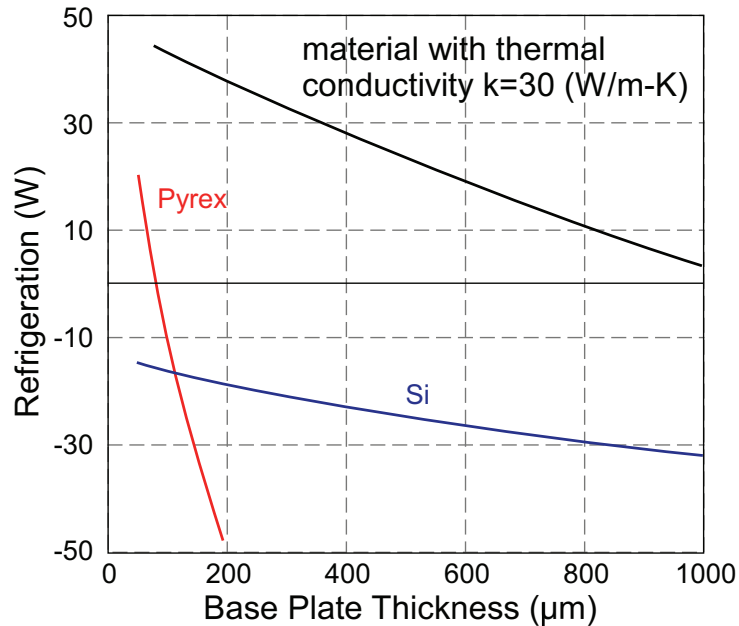


Figure 2.7: Refrigeration load as a function of the base plate thickness for silicon, Pyrex, and a material with a conductivity of 30 W/m-K.

2.3 Device Fabrication

2.3.1 Fabrication Process

There are five masks required for the process of this planar design shown in Figure 2.1. The fabrication process flow is illustrated in Figure 2.8

1) Two Si wafers of 200 μm thickness are bonded to a glass wafer of 100 μm thickness. The entire stack is loaded simultaneously into the bonding apparatus and heated to 400 °C, before a 500 V bonding voltage is applied. By sequentially reversing the polarity of the voltage source, both Si-Pyrex interfaces are bonded one-by-one.

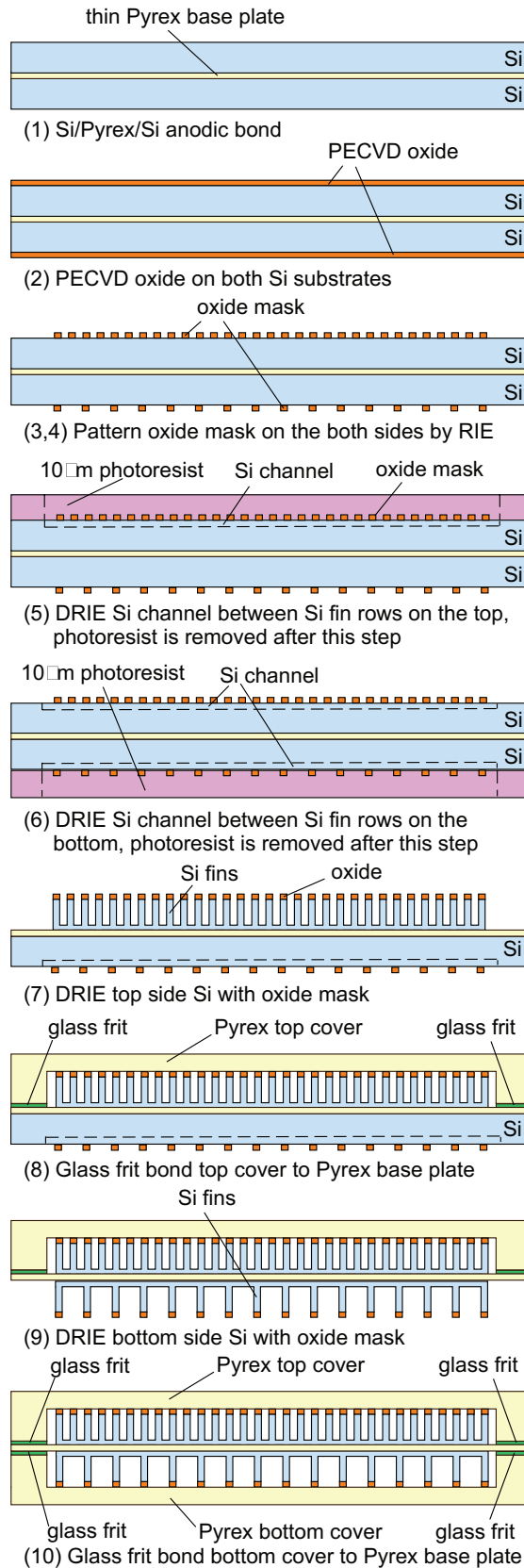


Figure 2.8: Fabrication process flow of the planar heat exchanger.

2) A 2 μm -thick layer of silicon dioxide is deposited on both sides of the Si surface using plasma enhanced chemical vapor deposition (PECVD). This layer and a subsequent layer of photoresist will serve as masks in a two-step deep reactive ion etching (DRIE) process.

3, 4) The oxide layers on both sides are patterned by reactive ion etching (RIE).

5) A 10 μm thick layer of photoresist is coated and patterned on the top side. A conformal thick resist layer is used to protect the oxide pattern in the next DRIE step. On the top side of the wafer, Si channels between each fin row are etched down 20 μm by DRIE before the photoresist is stripped. This etch will ultimately lead to the creation of the basal strip along each row that is illustrated in the magnified part of Figure 2.1. It is needed in part to compensate for a DRIE artifact that is explained in section 2.3.2.2, but also has the added benefit of strengthening the attachment of the fins to the glass base plate.

6) A 10 μm thick photoresist layer is coated and patterned on the bottom side. On the bottom side of the wafer, Si channels between each fin row are etched down 20 μm by DRIE. The photoresist is then stripped.

7) Fin rows on the top side are etched and defined by DRIE with an oxide mask. This is a high aspect ratio etch of 180 μm depth. The etch must clear the narrow regions between rows, etch between the tightly packed fins, and also clear the perimeter of the device, which has no masked features, and etches faster.

8) A glass cap (the fabrication of which is described separately, below) is bonded to the base plate with commercial glass frit tape (G1017, from Vitta Corp.) at 500 $^{\circ}\text{C}$ so as to construct a sealed chamber on the high pressure side. A significant challenge in this

step is the patterning of the tape, which cannot be done lithographically. In this effort, because of the large bonding area, the tape was cut and placed on the die manually.

9) A similar DRIE process is completed on the low-pressure side afterward.

10) Another glass cap is bonded onto the bottom side of the base plate using glass frit.

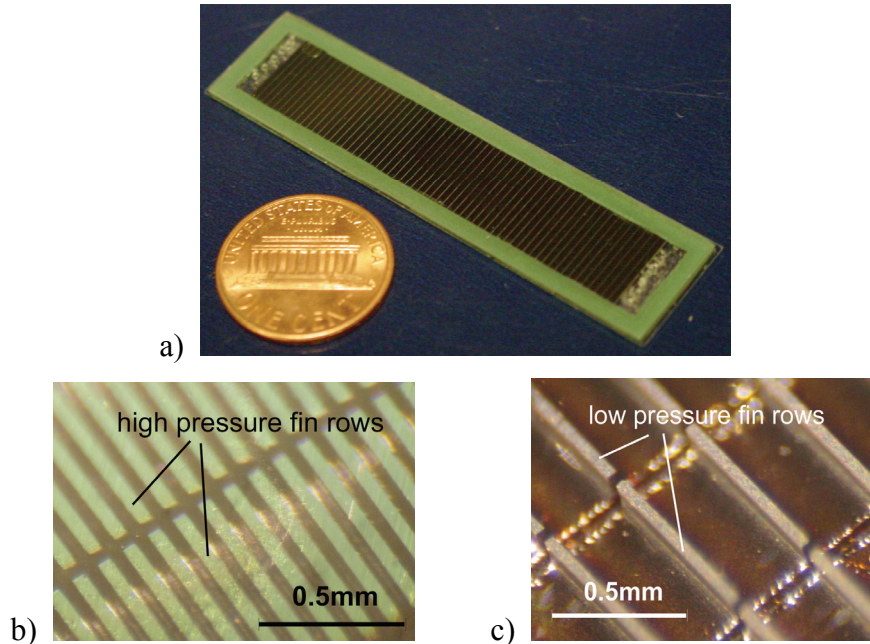


Figure 2.9: Fabricated planar heat exchanger. a) The size of the planar micro recuperator is $60 \times 15 \text{ mm}^2$ with a total 2.5 mm thickness. The gap between each fin row is $51 \text{ }\mu\text{m}$. b) High pressure fin rows with $50 \text{ }\mu\text{m}$ gap, fin size is $50 \times 782 \text{ }\mu\text{m}^2$, $200 \text{ }\mu\text{m}$ high. c) Low pressure fin rows with $345 \text{ }\mu\text{m}$ gap. The fin size is the same as that of the high pressure fins.

The glass caps are fabricated from 1.1 mm thick Pyrex wafers. The Pyrex wafer is coated with a $500 \text{ }\text{\AA}/5000 \text{ }\text{\AA}$ Cr/Au layer and then patterned with photoresist. Using the metal layer as a mask, the wafer is immersed in the HF:HNO₃ solution to create a recess that is $100 \text{ }\mu\text{m}$ deep. The photoresist and Cr/Au layer are removed after the wet etching. Inlet and outlet holes are drilled with an electrochemical discharge drilling method (see Section 2.3.2.3). This method provides a smooth and debris-free surface, but is a serial

method, and is not performed lithographically. An electrode needle is positioned in the proximity of the glass wafer while both are immersed in NaOH 30% wt. solution at room temperature. A bias of 33 V permits a 1100 μm thick glass plate to be perforated in about 10 s. Figure 2.9 shows a fabricated micro recuperative heat exchanger. The size of this device is $60 \times 15 \text{ mm}^2$ with 2.5 mm total thickness.

2.3.2 Related Fabrication Techniques

2.3.2.1 Wafer Bonding

In the microfabrication process of the planar heat exchanger design, several steps are involved in wafer-level or die-level bonding. These bonding steps are important to achieve hermetic seals in the bonding interfaces. As a result, the entire heat exchanger can remain leak tight at a very high working pressure.

Si/Glass/Si Anodic Bonding

A Si/glass/Si wafer bonding stack is required by the structure of the planar heat exchanger design in the initial stage of the microfabrication process. Since there is no commercially available wafer stack that meets our design requirement, bonding steps to produce such a wafer stack are necessary. Generally, these steps should be completed at the beginning of the process since otherwise the thin and fragile glass wafer is difficult to handle. A bonded wafer stack with more than 500 μm thickness is much easier to handle in the subsequent fabrication steps. Different from single Si/glass anodic bonding or glass/Si/glass stack anodic bonding, bonding a Si/glass/Si stack has its unique challenges due to the movement of sodium ions [Lee87, Kan90] during the anodic bonding process.

Two Si/glass interfaces are bonded in serial sequentially. During the first anodic bonding, the sodium ions accumulate on the unbonded surface of the glass wafer. These impurities will affect the bonding quality of the second anodic bonding on this surface and create a lot of bonding defects. To overcome these problem, two methods could be used to fabricate a 200/100/200 μm Si/glass/Si wafer stack. All wafers used in these processes are double side polished wafers.

a) A 500 μm thick glass wafer is anodically bonded to a 200 μm thick Si wafer. The wafer stack is then polished down to about 300 μm from the glass side such that the thickness of the glass layer is about 100 μm thick. The glass layer on the wafer stack is then anodically bonded to another 200 μm thick Si wafer. During the glass polishing step, the impurities created in the first anodic bonding step are removed from the glass substrate.

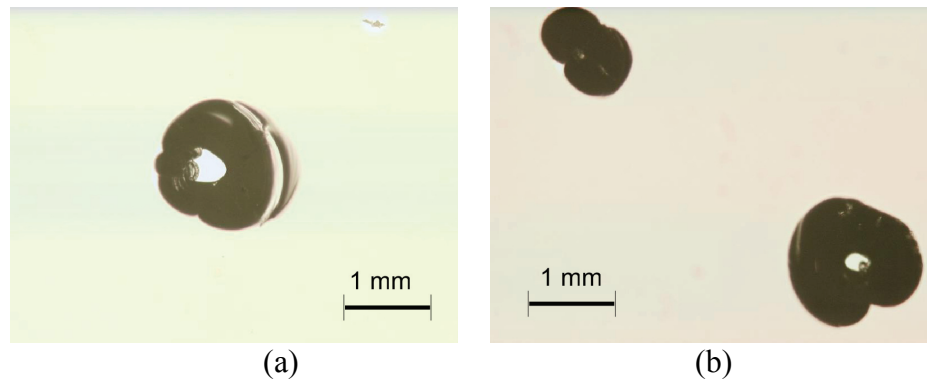


Figure 2.10: Polishing defects on the polished glass surface under microscope. The maximum diameter of the holes is more than 1 mm.

It is important to note, as a negative factor that the glass polishing step creates many polishing defects as well as mechanical stress on the substrate. The glass layer on the wafer stack polished by Alphaprecision Inc. produced many defects (Fig. 2.10) on the glass wafers. Many pin holes were generated during the polishing, some with diameter

larger than 1 mm. The holes significantly affected the subsequent anodic bonding step. Because the thickness is less than 100 μm after this polishing step, the 100 μm air gap in the holes will break down at 350-400 V during the anodic bonding. This resulted in low bonding quality around the pin hole. To compensate this, the anodic bonding time was lengthened much longer (>1 hour) in order to minimize the low bonding quality areas. The bonding results were acceptable after the modification. Additionally, if the through wafer pin holes on the glass layer locate within our design pattern, they can potentially cause leakage between the two fluid streams in the heat exchanger.

b) A 200/100/200 μm Si/glass/Si wafer stack is stacked together and anodically bonded. By alternating the applied voltage, the wafers are bonded in two different bonding steps. The cost of the 100 μm Pyrex glass wafer is high and it is very fragile. Extreme caution is required while cleaning and handling the wafers. However, since the wafer stack only needs to be loaded into the bonder once, this minimizes the possibility of breaking the glass wafer during the fabrication process. After the stack is bonded, the total thickness is about 500 μm . Due to the movement of sodium ions, a large number of sodium ions accumulate on the second bonding interface and create many bonding defects. The defects could not be easily recognized because the wafer stack is covered by non-transparent Si wafers on both sides. An infrared microscope can be used to identify the bonding defects. The bonding defects on the second bonding interface could cause the Si fin structure to peel off after the DRIE through wafer etching step due to the weak bond on those regions. As mentioned in the Section 2.3.1, the Si fin structure fabricated in the two-step DRIE process could minimize this weak bond problem. Since the fins in the same rows are connected together, the bonding area is much larger than the bonding

defects. Because of this differential, the fin rows are strong enough to attach to the glass substrate. However, the heat transfer near those bonding defects will be affected because the Si fins does not contact with the glass substrate well on those regions.

Since the second method proved to be a more reliable and robust process to bond the Si/glass/Si wafer stack, it was used in our last runs of the fabrication process.

Glass/Glass Die-Level Glass Frit Bonding

Although glass-glass bonding is commonly used in MEMS packaging and micro-fluidic systems, there are not many mature and commercially available wafer level or die level bonding methods and equipment being developed. Each bonding method is limited to a small range of applications. Many glass-glass bonding methods, such as glass/glass anodic bonding and direct bonding are required to apply high pressure to the substrates. This is not appropriate for our process since the processed wafer or die is very fragile.

Table 2.2: Different process conditions of glass bonding methods

Bonding method	Wafer interfaces	Temp (°C)	Bonding force/pressure	Voltage (V)	Surface roughness (nm)	Vacuum (mtorr)	Hermetic sealing	Precise gap
Anodic bonding	Pyrex/Si/Pyrex	400-500	0-150 N	100-1000	20	7.6×10^5 (1 atm)	Yes	Yes
Direct bonding	Pyrex/Pyrex	350	small	N/A	small	N/A	Yes	Yes
Eutectic bonding	Si/Au	363	1 MPa	N/A	-	-	Yes	No
Glass frit bonding	Si/Si, Si/Pyrex, Pyrex/Pyrex, etc.	400-600	1-20 psi	N/A	large	7.6×10^5	Yes	No

Intermediate layer bonding is also capable of obtaining good glass-glass bonding. Among them, glass-frit bonding is a broadly used method because a wide range of different glass frit products are commercial available. Table 2.2 shows bonding condition

of different glass-glass bonding methods. Among these bonding techniques, glass-frit bonding has relatively simple bonding conditions, i.e. low force applied to wafers, no voltage required, good particle tolerance, bonding pressure close to the atmospheric pressure, etc. Furthermore, commercially available low melting point glass compositions without contaminating the CMOS integrated devices make this wafer level packaging process most CMOS compatible.

Pyrex-Pyrex bonding is involved in process steps after through-wafer DRIE dry etching steps. In these DRIE process, the final Pyrex surface is not smooth enough after the Si is completely removed. On the edge of the wafer, residual Si remains on the areas that are covered by the clamps of the STS DRIE etcher. As a consequence, anodic bonding and direct bonding which have bad particle tolerance are inappropriate. In contrast, glass frit bonding does not require cautious surface pretreatment and has good particle tolerance, and is very suitable for our process.

Glass transfer tape as the intermediate layer is one the simplest method for glass frit bonding. A process using commercial glass frit transfer tape (G1017, from Vitta Corp.) to bond two glass substrates was developed. A programmable furnace is used in this process and the bonding process flow modified from a process recommended by the manufacturer is described below: 1) Two cleaned wafers are placed on the adhesive layer of the glass tape and are paired together. And then they are pressed with 1-20 psi for a period of approximately 10 minute. 2) The wafer stack is placed into the furnace and an approximately 1 kg metal piece is put on the wafer stack so that there is enough pressure on the wafer during the bonding. 3) The wafer stack is then heated to 520°C in 40 minutes. The temperate ramp rate of the furnace is programmable. 4) The temperature is

held at 520°C for 2 hours to make sure the glass frit is softened completely. 5) Finally, the wafer is left in the furnace overnight and cooled down to room temperature at a very slow rate.

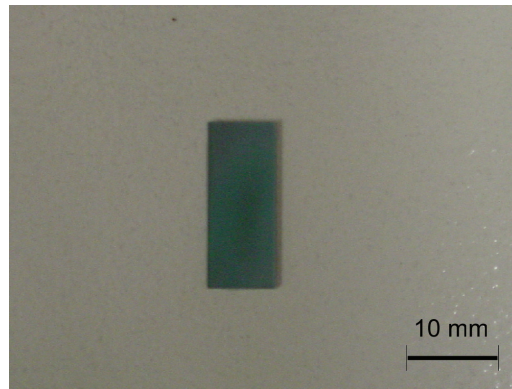


Figure 2.11: Die-level glass frit bonding with commercial glass frit tape. Color of glass frit tape changes to dark green when the bonding is completed.

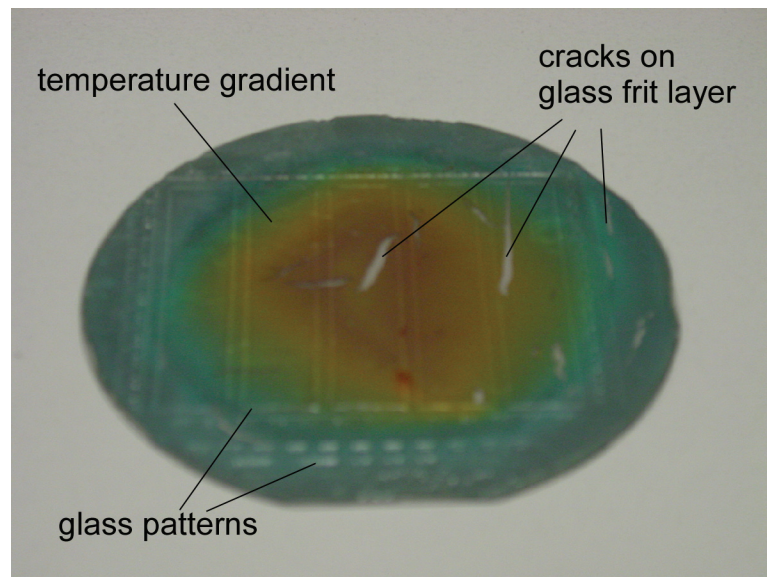


Figure 2.12: Wafer-level glass frit bonding. There are significant temperature gradients and cracks on the four inch wafer.

Figure 2.11 shows a sample that is successfully bonded and the color of the tape becomes dark green. However, the bonding on the wafer level with two hours holding is partially fail due to the existing temperature gradient. As shown in Fig.2.12, the color in

the center is orange which suggests that the holding temperature is much lower than the softening point of the glass frit tape, while the edge of the wafer is successfully bonded and the glass frit layer turns dark green. Furthermore, there are many cracks existing on the bonding area which are generated during glass frit tape separation. These cracks are expanded when the temperature is increased.

As a result of this glass frit bonding test, 1) the bonding of small samples has been successfully achieved. 2) there are significant temperature gradients on the wafer level bonding. The main reason is that the Pyrex substrate has a low thermal conductivity and the metal piece on the top of the wafer dissipate heat too fast so that the temperature in the center of the wafer is below the soften temperature of the glass frit tape. 3) Separating a glass frit tape with a large area is problematic. There are many unexpected cracks generated on the tape during this process. This results in enlarged cracks on the glass frit layer after the bonding process.

2.3.2.2 DRIE Through-Wafer Etching

Different from many of the Deep Reactive Ion Etching (DRIE) applications which etch deep channels or through holes on the wafer, our design requires etching many isolated islands (fin rows). Due to the large open area to be etched, the DRIE etch rate for our pattern is relatively low at about 2-3 $\mu\text{m}/\text{min}$. The initial design of fin rows contains rows of isolated fin structure. Each fin is separated from the other fins. There are several problems encountered during the DRIE process described as follows.

Micro-loading Effect

The non-uniform etch rate in plasma etching, so called micro-loading effect [Küh98, Cha00], is an important phenomenon and significantly affects our fabrication. This effect can be described as the interdependency between the etch rate and the aspect ratio, i.e. wide trenches etch faster than narrow trenches. In case of our through wafer etching, it is necessary to take into account an over-etch time to compensate this difference of etch rate. Figure 2.13 shows how the Si layer on the fin rows is etched through during the STS DRIE process. The Pyrex layer is exposed after the Si layer is etched away. The shape of the Si shrinking area shown in Fig. 2.13 also varies depending on the pattern location on the wafer.

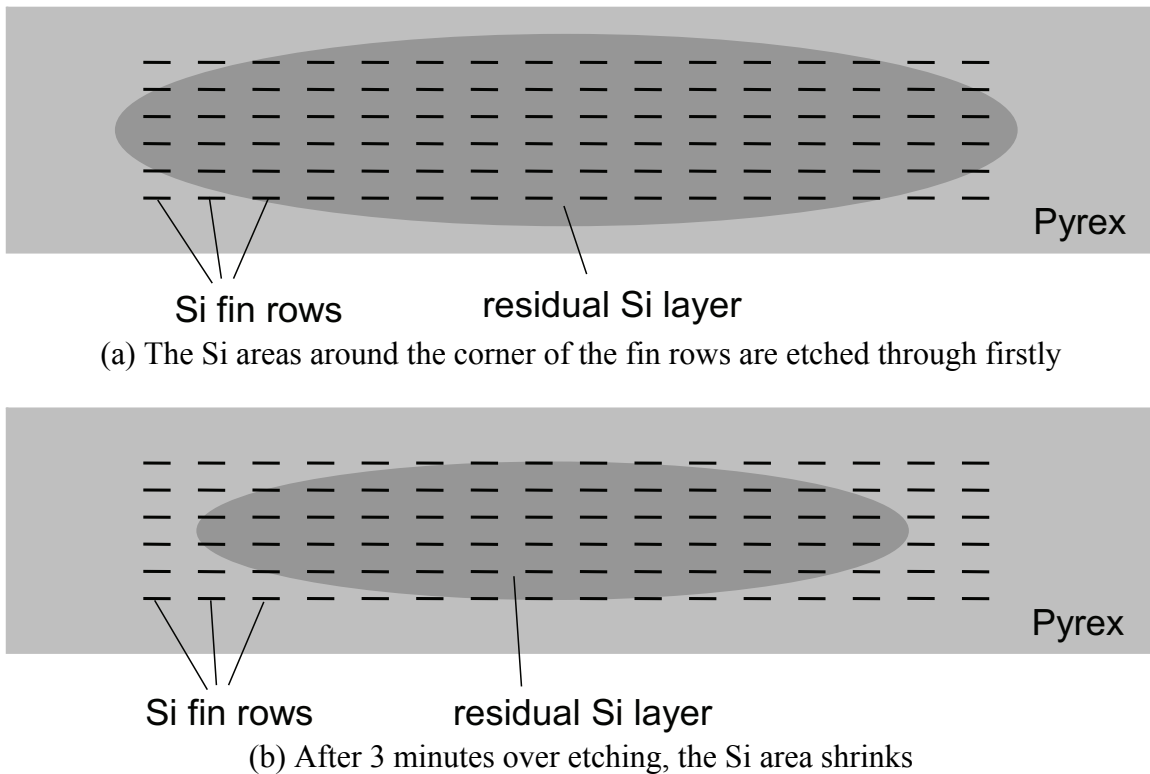


Figure 2.13: DRIE process when Si substrate is almost removed from the glass layer. The pattern is located in the center of the wafer.

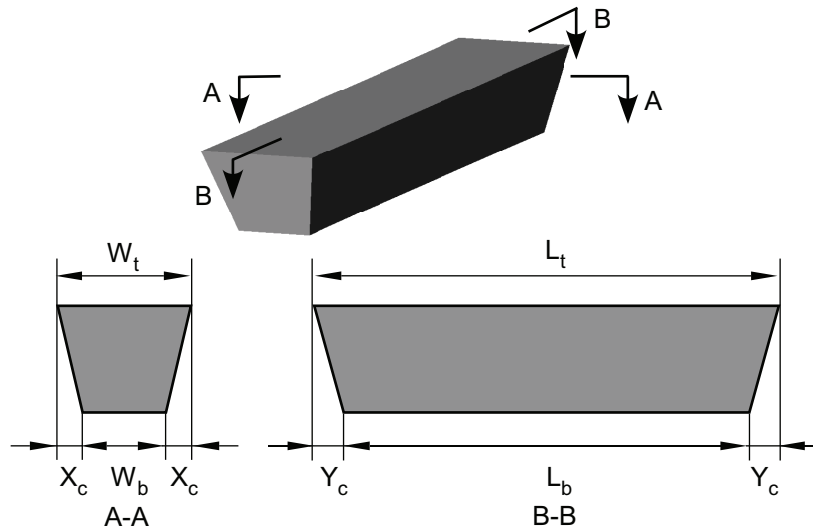
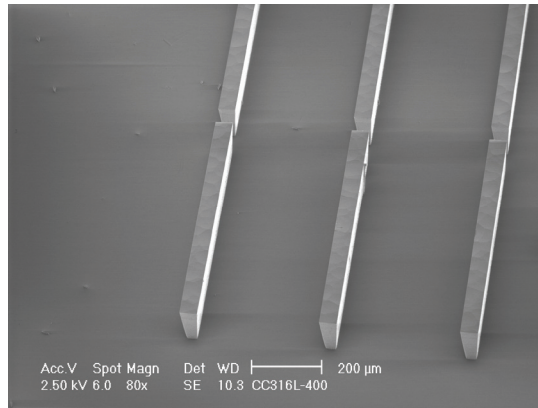
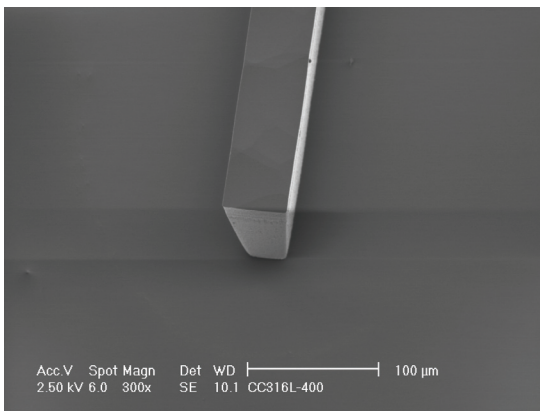


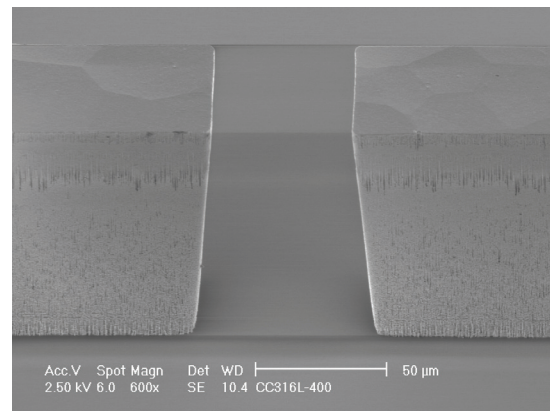
Figure 2.14: Lateral Cross section A-A and Longitudinal cross section B-B. The lateral footing undercut X_c and longitudinal footing undercut Y_c are ideally symmetric on their cross section, thus $X_c = (W_t - W_b)/2$ and $Y_c = (L_t - L_b)/2$.



a)



b)



c)

Figure 2.15: SEM of fin rows after DRIE. a) Fin rows on low pressure side. b) Lateral undercut on a fin. c) Longitudinal undercut on the fins.

Footing Effect

Furthermore, a lateral etching at the Si/Pyrex interface, called notching effect or footing effect [Ish99], occurs when the wafer is over-etched. Once the fins around the corner and the edge are etched through, the positive ions charge up on the Pyrex substrate on those areas and attack the fins from the bottom, which results in a footing undercut Xc on the bottom of the fins (See Fig.2.14.). If the over-etch time is too long, the fin structure will be damaged due to a large lateral footing effect Xc on the bottom.

Fig.2.15 shows the lateral and longitudinal footing effects on the fins after 10 minutes over-etch. The over-etch time has to be controlled less than 10 mins for every fin in order to avoid damaging the fins from the footing effect. Additionally, due to the micro-loading effect, the silicon near the corners is completely etched away faster than the silicon in the center of the pattern. Accordingly, the time between these two regions to be cleared away should be limited to less than 10 mins. In most cases, this can be guaranteed because the etch rate (2-3 μm) is fast enough. However, a further over-etching is not recommended after the silicon area in the center is cleared.

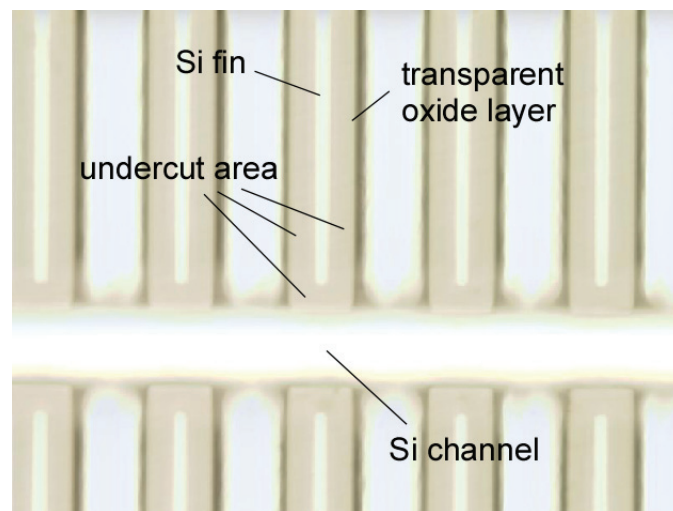


Figure 2.16: Undercut beneath oxide layer. The oxide mask is transparent.

Undercut Beneath the Oxide Layer

A 2 μm thick oxide layer is used for the DRIE etch mask. The undercut (Fig. 2.16) is more serious than the Al mask and photoresist mask since the dielectric layer is charged up by the plasma. There are many etching parameters such as temperature, etch time, SF_6 flow rate, RF power, etc. that affect the undercut. Serious undercut results in the oxide mask coming off after 10-30 mins of etch time.

Two-Step DRIE Process

Optimizing the DRIE chemistry is one of the significant challenges of the process for three reasons: a) the relatively large size of the device and the narrow widths of the fins demand high uniformity over a large area; b) the DRIE step must clear the narrow openings between rows and the wide spaces of the perimeter simultaneously; and c) the termination of the etch on the glass layer sandwiched between the two Si layers causes footing effect, which is the lateral spread of the etch profile once the insulating glass is exposed at the bottom of the trench. The two-step DRIE mentioned in section 2.3.1 is designed to fabricate separated grooves on the both sides, shown in Fig. 2.1, and compensate for the non-uniform etch rate due to the varying density of the features. Due to micro loading, the areas between fins and fin rows with small openings are usually etched more slowly than the area around the device with large openings. Since each fin row must be thermally isolated along the flow direction, the Si in the gap between fin rows must be completely etched away while the over-etch in the area around the device must be minimized to prevent the footing effect from damaging nearby fins. In the first DRIE step, the area between each fin row is etched down 20 μm , allowing this densely

packed region to be fully etched through during the second DRIE. Additionally, since the fins in the same row connect to each other at the bottom (see magnificent figure in Fig. 2.1), the bonding strength of entire fin rows is much stronger than a single fin. The large Si/glass contact area also minimizes the possibility of Si fin peeling off problem created by anodic bonding defects mentioned in the section 2.3.2.1.

2.3.2.3 Electro-Chemical Discharge Machining (ECDM)

Electrochemical drilling [Esa90, Fas99, Wüt05] on a glass wafer has been widely used in many MEMS applications. Good surface finishing on the substrate as well as low cost can be achieved by a simple electrochemical drilling setup.

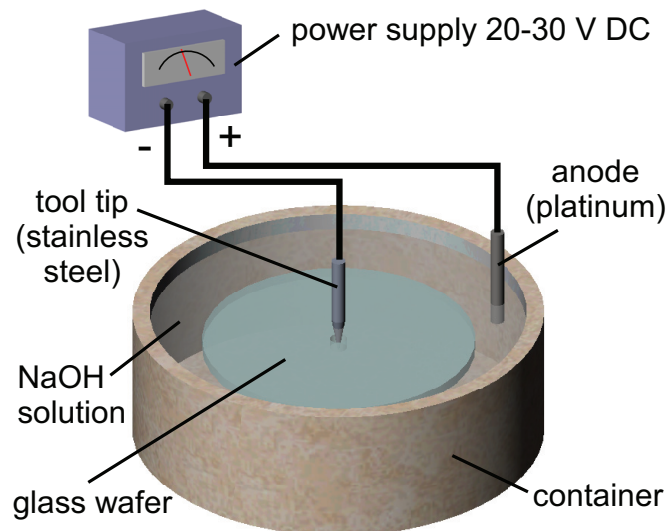
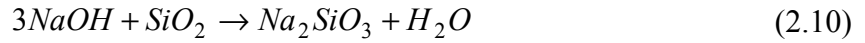


Figure 2.17: Schematic diagram of the electrochemical discharge drilling setup. The material of the tool tip can be stainless steel, tungsten, platinum, etc.

Mechanism

Figure 2.17 shows the schematic diagram of the electrochemical drilling method. The glass wafer is placed into the NaOH solution. By applying 20-30V DC to the electrode (Anode) and tool tip (Cathode), sparks are generated between the tool tip and

glass substrate, thereby eroding the glass. The etching of the glass is due not only to the thermal etching generated by the discharges, but also to the chemical etching by alkali solution. The etching reaction is:



The etching mechanism results in a smooth surface when the dissolution of the silicate is complete.

Fabrication and Results

Several inlet and outlet holes have to be drilled on each Pyrex cap in our process. The size of holes mainly depends on the size of the tool tip. 0.5 mm diameter tool tip is used in our case when 25V DC voltage is applied. The sidewall profile of the holes is shown in Fig.2.18. The size of the hole is about 0.7 mm.

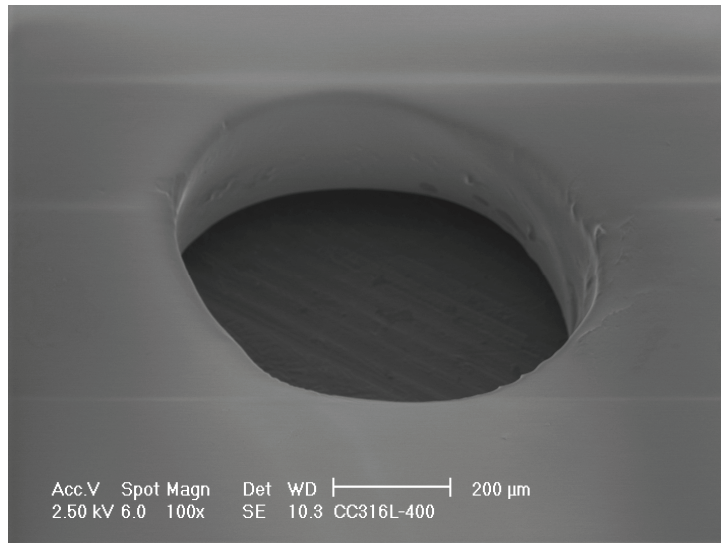


Figure 2.18: SEM of an electrochemically drilled hole on a 350 μm thick Pyrex substrate.

Prior to the drilling, the positioning of the tool tip has to be done manually. The tool tip is easy to slide on the glass surface sometimes which can result in a channel on

the substrate (Fig.2.19). Without precise position control, the holes can only be drilled roughly in a row. With a stable setup and position control units in the setup [Fas99], the sidewall profile can be improved while the tool tip sliding problem and positioning problem can be solved. For these reasons, our ECDM setup, shown in Fig. 2.20, is constructed from a 3-axis precise optical stage which provides precise position control in three directions. Fig. 2.21 shows the fabricated Pyrex glass cap with rows of holes drilled by ECDM.

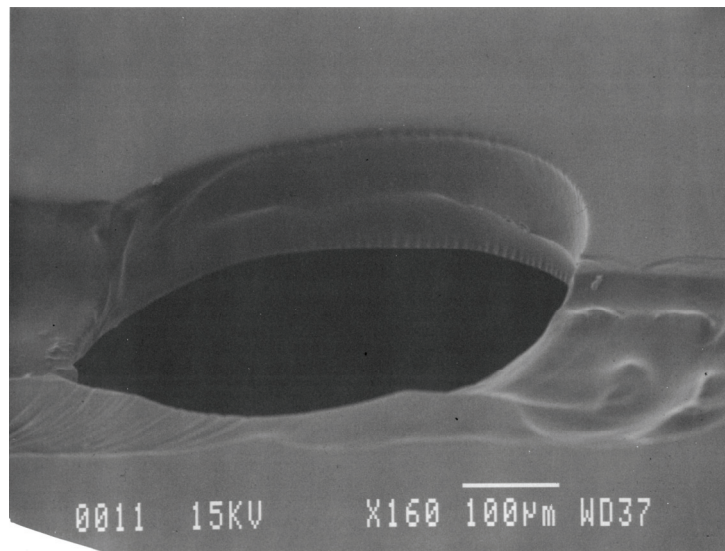


Figure 2.19: Channel formed when the tool tip slides on the Pyrex substrate during the electrochemical discharge drilling.

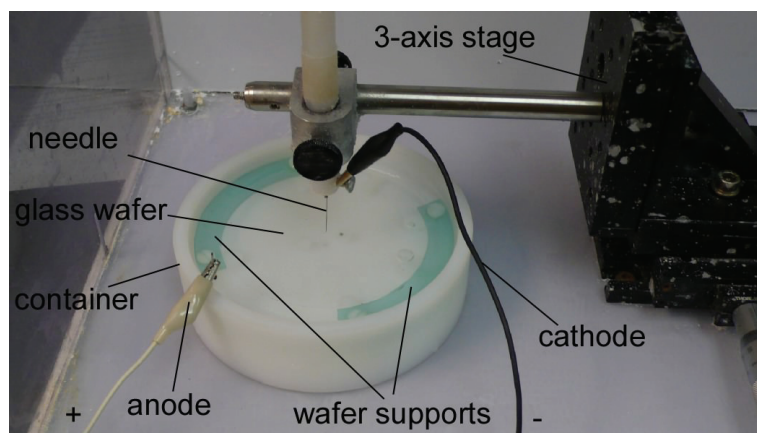


Figure 2.20: Photograph of ECDM setup.

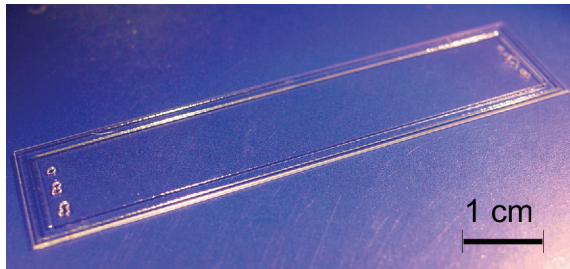


Figure 2.21: Inlet and outlet holes line up in a row on the Pyrex cap.

Summary

ECDM is a low-cost and high-yield solution for our glass etching process because of its fast etch rate and simple setup. There are several advantages listed as follow: 1)• simple setup and low cost; 2) fast etch rate; 3) good etching profile with appropriate parameters and position control; 4) no mask needed. In our design, the total number of holes that need to be drilled is limited to 50 per wafer. Other methods, such as laser drilling or glass wet etching, dramatically increase the manufacturing cost of the process. The inlet and outlet holes were successfully fabricated in our ECDM setup.

2.3.2 Discussion in Fabrication

As mentioned in Section 2.3.1.1 Si/glass/Si anodic bonding is a very critical step and ideally, no void or crack is allowed after the bonding. Any big void may result in fin structure damage during the DRIE step and a crack may lead to leakage between the two fluid streams while the device is being tested.

In addition, the DRIE process is another difficult step due to the reasons mentioned in Section 2.3.1.2. Although the two-step DRIE process is very effective in minimizing the negative aspects and achieving the structures we desire, the process itself is still not consistent due to the limits of the available equipment. In our process, wafer-level DRIE

etching proved to be substantially more problematic and inconsistent than die-level DRIE etching because of the much larger area to be etched on the substrate.

Finally, the footprint of the device is so large that a small defect produced on the wafer in some critical fabrication steps would result in the failure of the device and consequently affect the yield.

2.4 Experimental Results

In order to protect the heat exchanger from bending loads as well as to provide some reinforcement for the Pyrex structure against pressure loads during assembly of the test setup, the header design shown in Figure 2.22 was installed on each of test samples. The structural plate composed of low conductivity G-10 stretches across the entire heat exchanger and is clamped via several small bolts.

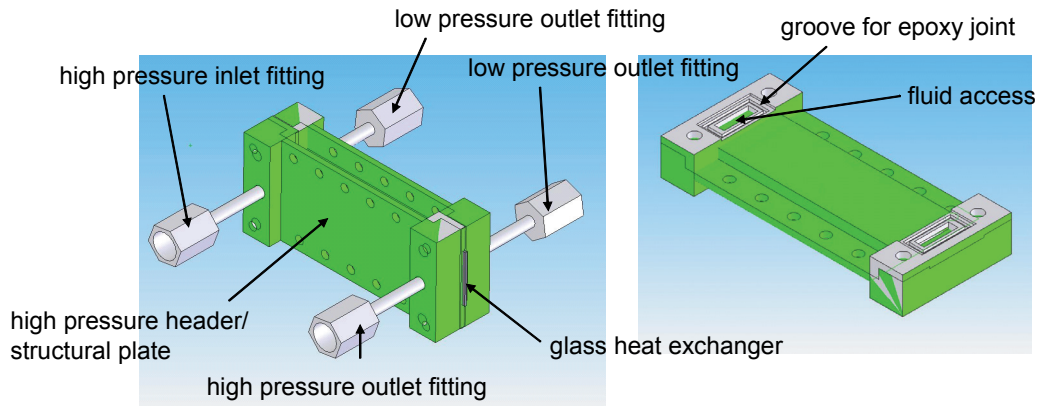


Figure 2.22: Solid model of header/structural plate and planar heat exchanger.

2.4.1 Preliminary Tests

The micro heat exchanger was first tested in an ice bath, with helium gas flowing through one side of the micro heat exchanger and ice water flowing through the other side. Figure 2.23 shows the schematic diagram of this setup and Figure 2.24 & 2.25

shows the photos of the setup. At the beginning of the test, the ice water inlet pressure was increased in order to match the helium inlet pressure, so that the pressures on either side of the heat exchanger were approximately balanced. This configuration provided essentially a constant, 0 °C heat sink on one side so that the thermal effectiveness could be evaluated in this simple limit and compared with the numerical model of the device.

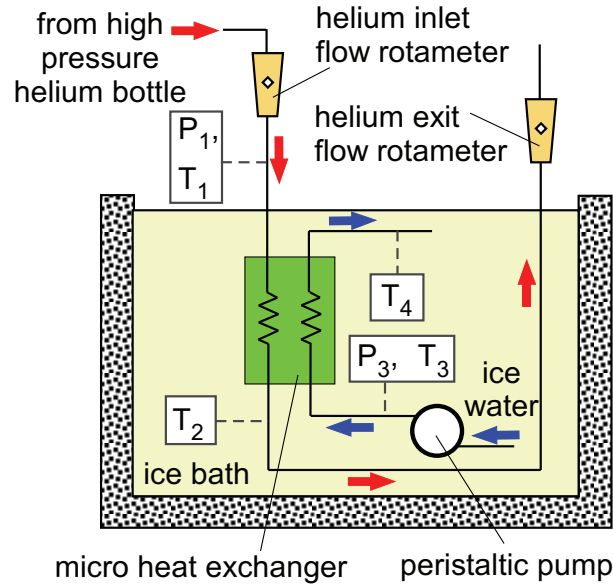


Figure 2.23: Ice bath test setup of the micro heat exchanger. The temperature measurements use Type E thermocouples.

penetrated thermocouples

planar heat exchanger

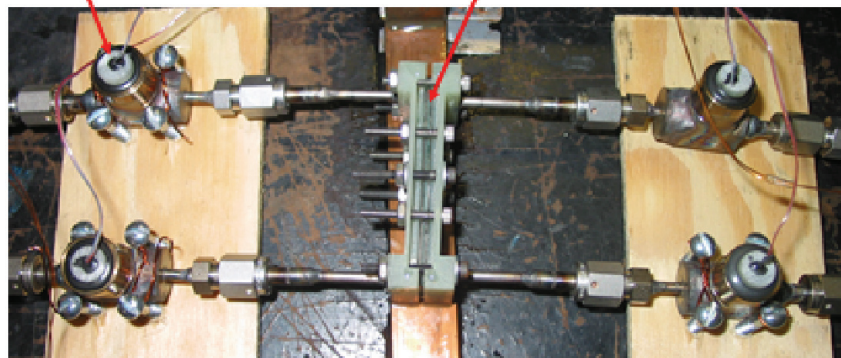


Figure 2.24: Photograph of ice bath test setup (at UW-Madison).



Figure 2.25: Photograph of test setup submerged in ice bath (at UW-Madison).

Figure 2.26 illustrates the inlet and outlet flow rate measured for the high and low pressure sides of the device. Note that the low pressure side of the micro heat exchanger allows much more flow for a given pressure difference due to the larger channels on the low pressure side. The inlet and exit flow rates should be the same as there was no leakage observed during the testing; however, the difference is nominally within the uncertainty of the rotameters that were used.

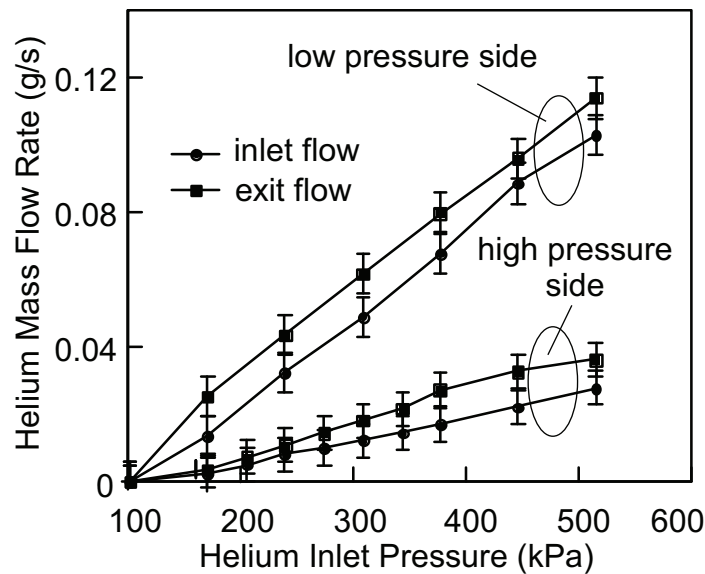


Figure 2.26: Helium flow rate measured by the inlet and exit flow meters as a function of the helium inlet pressure for the high and low pressure sides.

Figure 2.27 illustrates the helium exit temperature (relative to the ice water temperature) as a function of the helium flow rate (the average measured by the inlet and exit rotameters) for the two sides. The helium inlet temperature was between 17-19 °C for all tests and this leads the helium exit temperature to be an indicator of the thermal performance of the heat exchanger: a lower helium exit represents better performance. As expected, the high pressure side showed better performance than the low pressure side because the fin structure is denser. However, this difference is relatively slight because the dominant thermal resistance in the heat exchanger is the Pyrex plate.

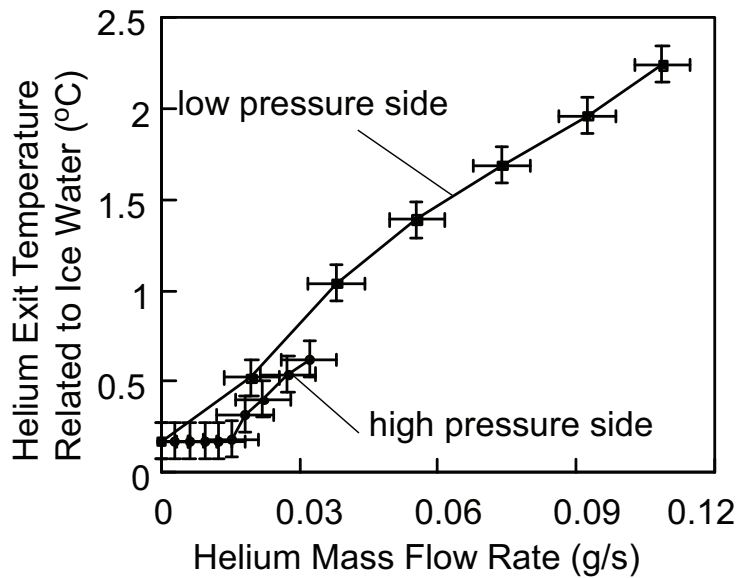


Figure 2.27: Helium exit temperature, relative to measured ice water temperature, as a function of flow rate (average measured by the inlet and exit flow meters) for the high and low pressure sides.

2.4.2 Self-cooling Test

In the self-cooling test, the device was installed into a macro-scale self-cooling system shown in Figure 2.28. In this experiment, the heat exchanger is placed in a cavity within a piece of Styrofoam insulation and surrounded by fiberglass insulation. The hot inlet is provided with a flow of butane from a high pressure bottle at room temperature.

The pressure, flow rate, and temperature (T_1) of this flow are measured. The high pressure butane passes through the heat exchanger where it is pre-cooled by the low pressure butane returning from the cold end. The butane is expanded through an orifice (a precision jewel installed in a blank gasket) located at the cold end of the system; by varying the size of the orifice it is possible to control the flow rate through the heat exchanger. The temperatures on either side of the orifice (T_2 and T_3) are measured using thermocouples that penetrate the butane stream.

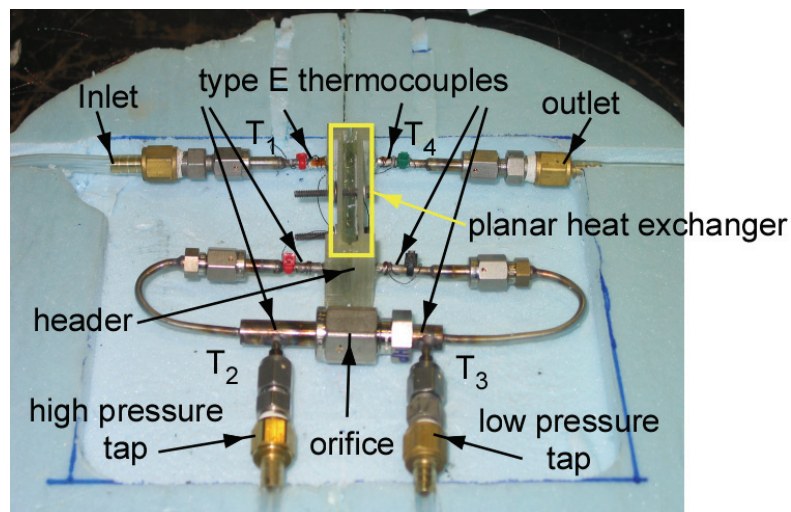


Figure 2.28: Self-cooling setup. Butane gas with regulated pressure is introduced from the inlet. The micro recuperative heat exchanger is mounted inside the header. The type E thermocouples are inserted into the high and low pressure taps to measure the gas temperature inside the tube (at UW-Madison).

Figure 2.29 illustrates the temperature difference between the cold end and the inlet as a function of the orifice area for three different inlet pressures. The optimal orifice size is 0.2 mm^2 . The temperature difference as a function of inlet pressure for this optimal orifice is shown in Figure. 2.30; the measured temperature difference matches the theoretical model assuming a parasitic heat load of 40 mW.

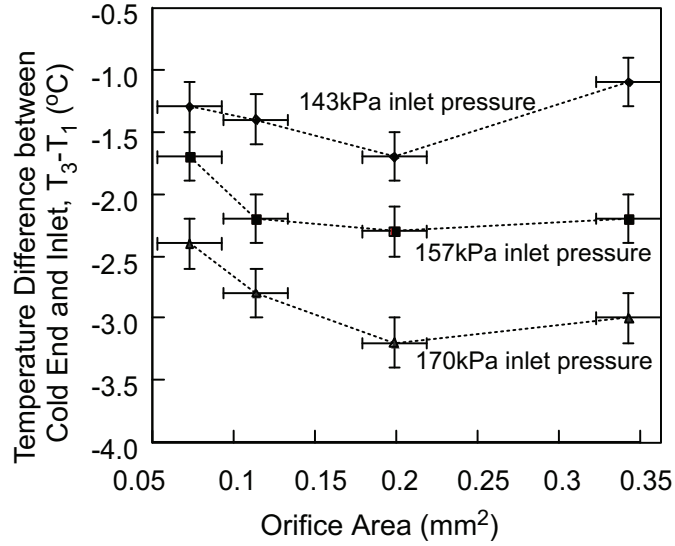


Figure 2.29: Temperature difference between the cold end and the inlet as a function of the orifice area for three different inlet pressures.

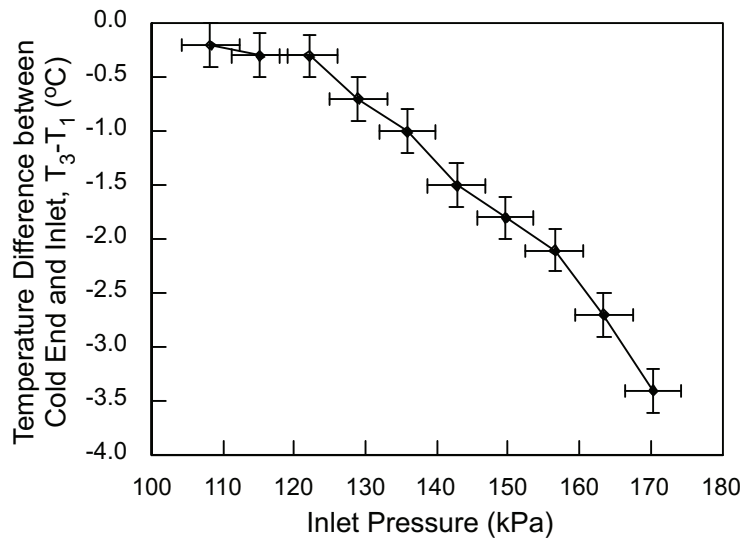


Figure 2.30: Temperature difference between the cold end and the inlet as a function of the inlet pressure for the 0.2mm² orifice area.

2.4.3 Discussion

In addition to the challenges in the various steps identified in the design and fabrication section, the development of the fabrication process has yielded a number of important lessons. At a very basic level, the fragility of the 100 μm thick glass plate requires it to be bonded to at least one Si wafer as early as possible in the process.

Another general challenge is the footprint of the device, which is so large that the possibility of a defect or non-uniformity is high. In the processing steps, as already discussed, the primary challenges include the double-sided bonding of the glass wafer; the DRIE sequence and its limitations related to overall uniformity, micro loading, and footing; the frit glass bonding; and the electrochemical etching. However, reasonable solutions exist for each of these challenges, and a feasible process for manufacturing heat exchangers in this manner has been developed.

The self-cooling data is limited to very small temperature differences relative to a practical device that is useful for cryosurgery. This is due to the following reasons:

1) The difference between the high and low pressures in the heat exchanger is limited by the structural integrity of the base plate. The pressure difference anticipated for a cryosurgical probe may be as high as 1400 kPa (200 psi) whereas the testing was limited to 70 kPa (10 psi) in order to avoid fracturing the base plate. Theoretically, this thickness of the base plate should be able to sustain larger pressure differences, but in practice this is not true. A thicker base plate would provide greater structural integrity, but the increased transverse thermal resistance would further reduce cooling power. This design concept is not ideal if the base plate is made of Pyrex and an alternative material with a higher conductivity (optimal value is about 30 W/m-K) must be found to make this concept practical.

2) The fin height of 200 μm is much smaller than the initial design target of 500 μm because of the fabrication limits. This results in both a 2.5 \times reduction in heat transfer area and a 5 \times increase in the pressure drop due to decreased flow area.

3) The structural integrity and hermeticity restrictions prevent installation in a thermal vacuum facility. Accordingly, there is a substantial parasitic heat load on the device that prevents it from achieving very low temperatures.

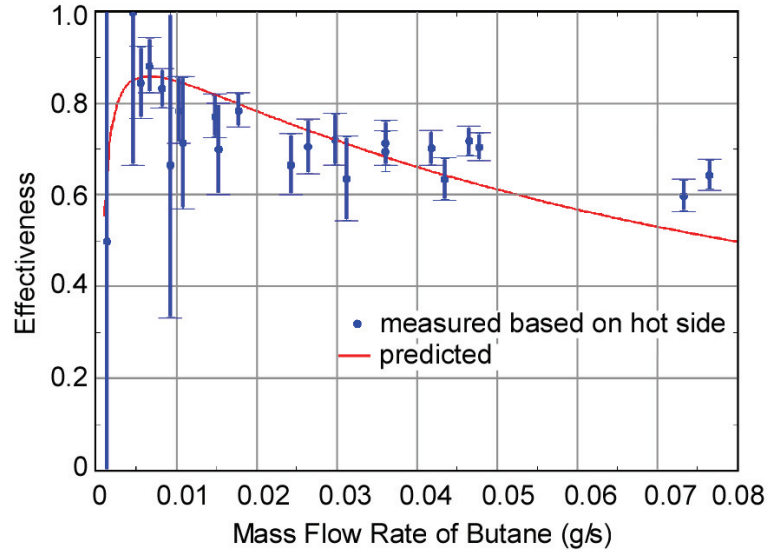


Figure 2.31: Measured effectiveness based on hot side energy balance and the predicted effectiveness using the micro heat exchanger model as a function of the mass flow rate.

The predicted and measured effectiveness [Inc96, Bar99] as a function of mass flow rate (based on the hot side energy balance) is illustrated in Figure 2.31. The effectiveness of the heat exchanger (ϵ) is defined as the ratio of the heat transferred within the heat exchanger to the maximum possible amount of heat that could have been transferred had the heat exchanger been perfect (i.e., the heat transferred if T_4 was equal to T_1). If we assume that the specific heat is constant across the length of the heat exchanger and there is no internal fluid leakage, the effectiveness can be computed based on either the hot- or cold-side balance (ϵ_h or ϵ_c , respectively) by Eq. (2.10) and (2.11):

$$\epsilon_h = \frac{\dot{q}_{h,net}}{\dot{q}_{max}} = \frac{\dot{C}_h(T_{h,in} - T_{h,out})}{\dot{C}_{min}(T_{h,in} - T_{c,in})} \approx \frac{T_1 - T_2}{T_1 - T_3} \quad (2.10)$$

$$\varepsilon_c = \frac{\dot{q}_{c,net}}{\dot{q}_{max}} = \frac{\dot{C}_c (T_{c,out} - T_{c,in})}{\dot{C}_{min} (T_{h,in} - T_{c,in})} \approx \frac{T_4 - T_3}{T_1 - T_3} \quad (2.11)$$

where $\dot{q}_{h,net}$ is the net heat transfer from the hot fluid; $\dot{q}_{c,net}$ is net heat transfer to the cold fluid; \dot{q}_{max} is the maximum possible heat transfer in the heat exchanger; $T_{h,out}$ is the hot fluid outlet temperature; $T_{c,out}$ is the cold fluid outlet temperature. The error bars in Fig.2.31 represent the theoretical errors based on the uncertainty in the thermocouple temperature measurements. Note that the error increases as the mass flow rate drops due to the smaller temperature differences that are required to compute the effectiveness. This measured result properly matches the theoretical model.

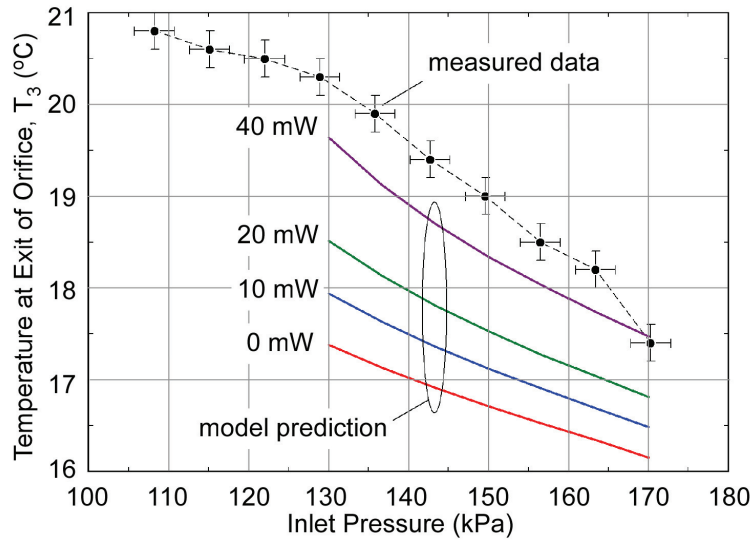


Figure 2.32: Measured and predicted low temperature (T_3) for various values of parasitic heat loads as a function of the inlet pressure. The experiment is completed at ambient temperature at about 21 °C.

The measured temperature at the exit of the orifice (T_3), together with the model prediction for various values of parasitic heat loads at the cold end, is shown in Fig. 2.32 as a function of inlet pressure. The measured data is close to model prediction of the 40 mW case.

As described above, the Pyrex base plate continues to limit the thermal performance of the device; the fundamental design concept is not ideal if the base plate is made of Pyrex. In order to improve the robustness of the planar design, the solution could be either to modify the support of the thin glass base plate or to find an alternative base plate material with a thermal conductivity close to 30 W/m-K, as shown in Fig. 2.7. Sapphire is an alternative base plate material that requires a further investigation.

CHAPTER 3

Perforated Plate Design of the Micromachined Heat Exchanger

In order to sustain much higher pressure needed by the J-T cycle and overcome the fabrication limits described in Section 2.4.3, a new heat exchanger design is desirable for a better cooling performance at high pressures. This chapter describes a Si/glass perforated plate heat exchanger design that is suitable for micromachining². Section 3.1 introduces the design concept and mechanism of this heat exchanger. This design utilizes a structure with silicon plates and glass plates alternatively bonded together to construct a perforated plate heat exchanger. Platinum resistance temperature detectors (Pt RTDs) are selectively integrated to the silicon plates for in-situ temperature measurement. Section 3.2 summarizes a numerical model of this heat exchanger developed by our collaborators from the University of Wisconsin-Madison. Section 3.3 describes the fabrication process of this heat exchanger and the existing challenges. Section 3.4 describes the experimental setups. A cryogenic test facility was designed and assembled at the University of Wisconsin-Madison for effectiveness measurements of this heat exchanger and self-cooling tests in a J-T cycle. The experimental results and evaluations are reported in Section 3.5.

² Portions of this effort were reported in abstract form in [Zhu07, Zhu08].

3.1 Design Concept

Perforated plate counter-flow heat exchanger is one of the most common heat exchanger structures. Figure 3.1 illustrates a Si/glass perforated plate structure that is suitable for micromachining. The concept is similar to most perforated plate heat exchangers: high conductivity plates (silicon) are alternated with low conductivity spacers (glass). With thicker Si or glass walls between the two streams, this structure potentially eliminates the problem of fragility of thin base plate in the planar design and can consequently sustain much higher pressure difference between the two streams.

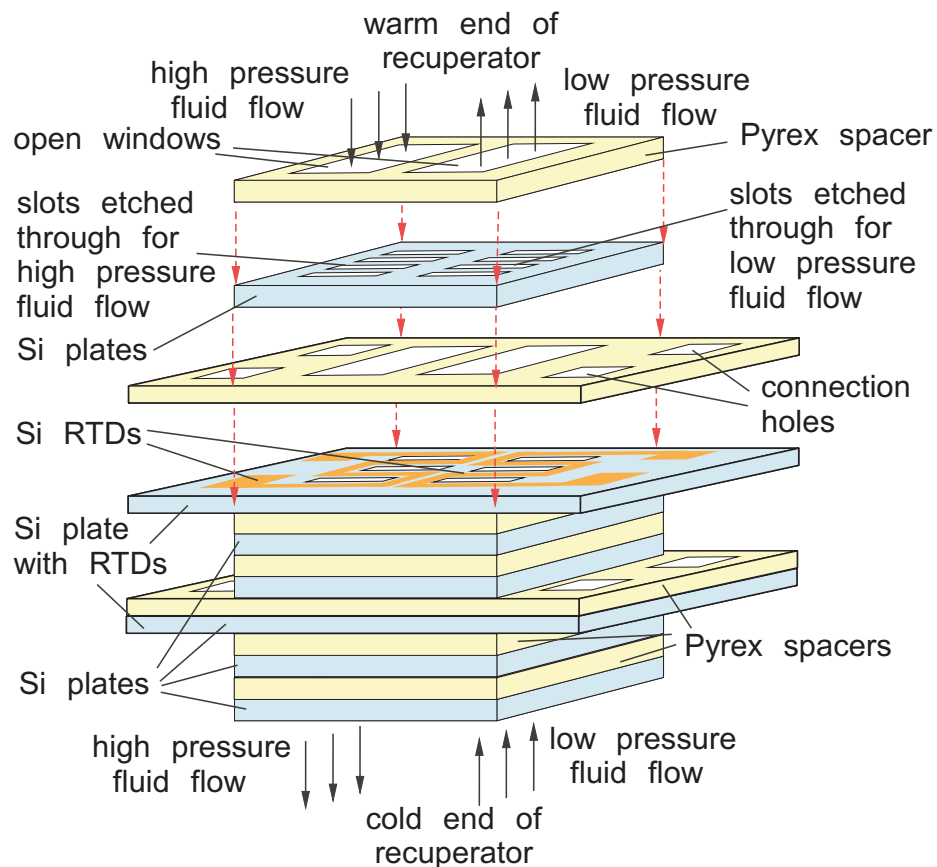
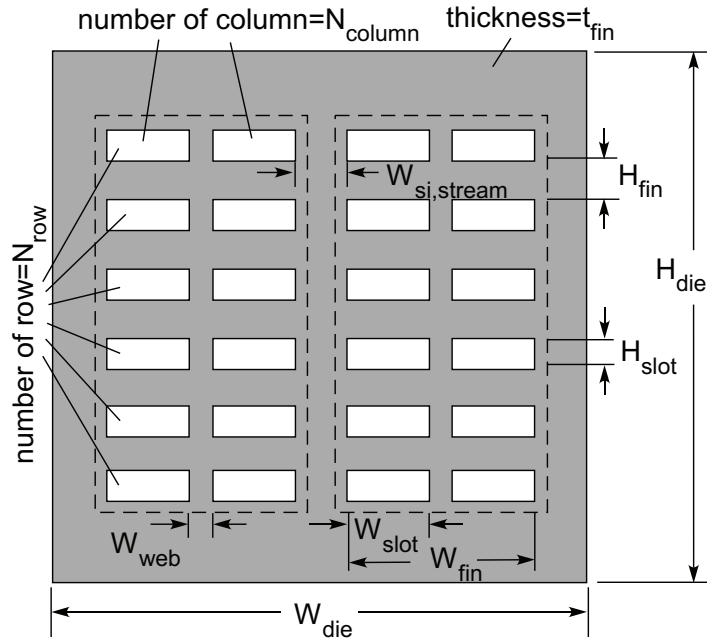
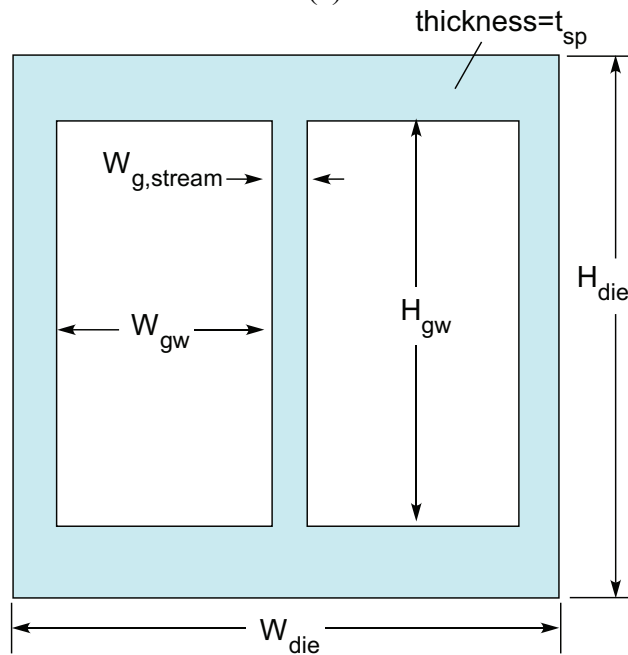


Figure 3.1: Concept for the micromachined perforated plate heat exchanger.



(a)



(b)

Figure 3.2: Design geometries of (a) a single silicon plate, and (b) a single glass spacer.

In this heat exchanger, narrow slots are machined into the silicon plate in order to provide the two streams with a large amount of surface area for heat exchange. A single silicon plate, as shown in Fig. 3.2a, is divided into two regions by the spacer. The high-

pressure region allows the high-pressure fluid to flow in one direction (from top-to-bottom in Fig. 3.1) while the low-pressure region allows the low-pressure fluid to flow in the opposite direction. A single spacer is shown in Fig. 3.2b. The high- and low-pressure regions are sealed from each other via joints between the plate and the spacer. The heat transferred from the high-pressure fluid into the silicon plate is conducted through the silicon plate into the low-pressure region where it is transferred finally to the low-pressure fluid. The glass spacers are used for thermal isolation between the silicon plates along the flow direction. As a result, a large temperature gradient in this direction is achieved.

There are many different slot pattern configurations on the silicon plates. For example, ideally, the two fluid regions can be concentric while the high-pressure region is in the center and the low-pressure region is in the outer. The orientations of the slot patterns could also be changed. The slot pattern shown in Fig. 3.2 is chosen for several reasons: 1) KOH wet etching process is used to replace the DRIE dry etching for fabricating the silicon slot pattern. The orientation of the slot pattern is therefore constrained by the crystal orientation of silicon. 2) Leakage between the two regions is a potential weakness of the perforated plate heat exchanger. The square configuration shown in Fig. 3.2 minimizes the bonding interface between the two regions, thus reduces the possibility of internal leakage between the two streams. 3) The silicon and glass plates are generally diced to rectangular or square dies. Compared to the circular configuration, this design can fully utilize the available space within a die.

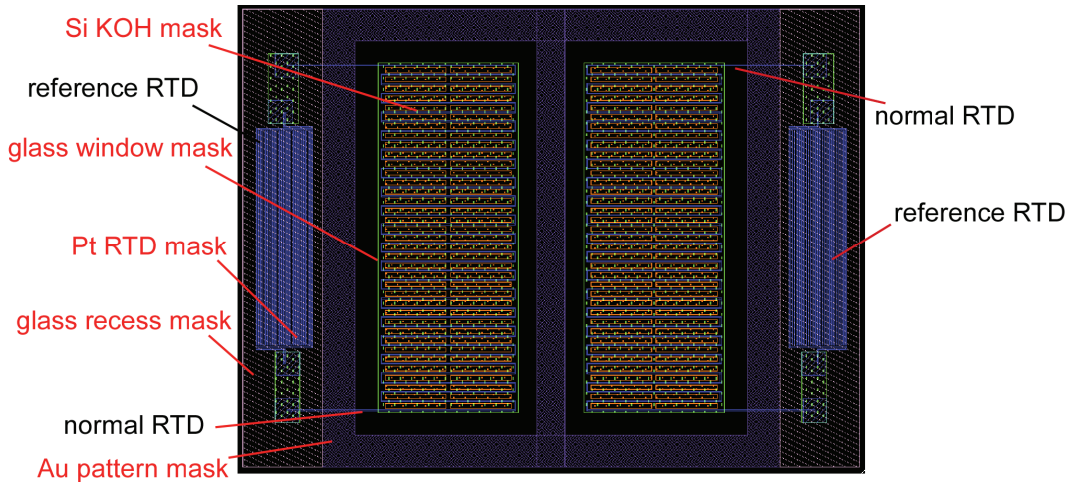


Figure 3.3: Mask layout of $10 \times 10 \text{ mm}^2$ die integrated with Pt RTDs.

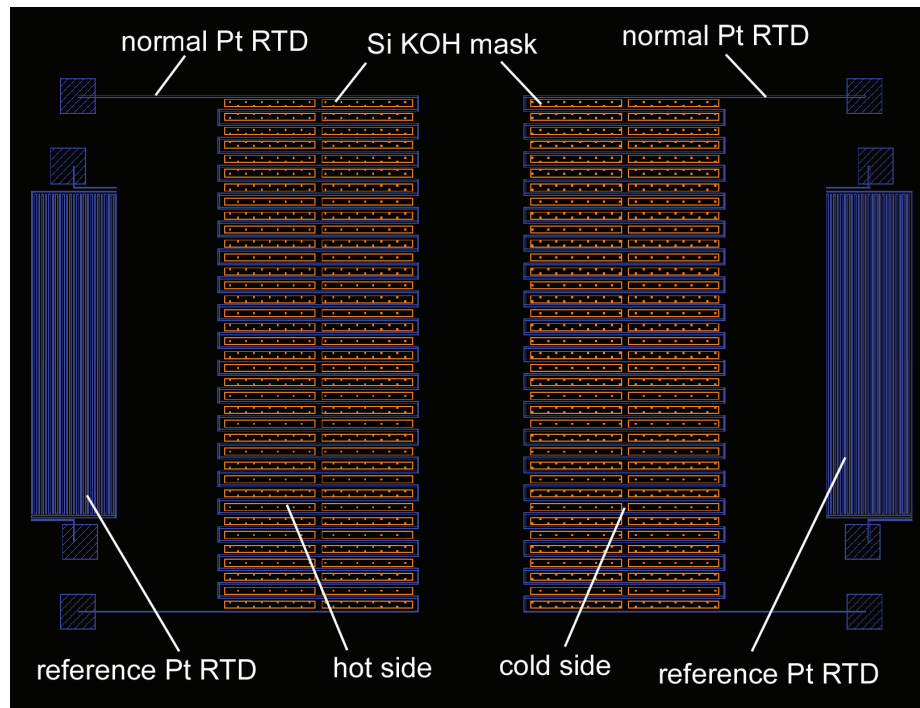


Figure 3.4: Silicon KOH mask and RTD mask layout of $10 \times 10 \text{ mm}^2$ die integrated with Pt RTDs.

Thin film Pt RTDs are deposited to the silicon plates and those plates are selectively placed into the heat exchanger stack. These Pt RTDs allow for precise in-situ temperature measurement inside both the high- and the low-pressure regions. The measured temperature distribution can be used for validating our numerical model as well

as diagnosing leakage or clog problem inside the heat exchanger in real time. In the silicon dies integrated with RTDs, there is one RTD on each side of the silicon pattern to measure the average fluid temperature on that region. There is another reference RTD located next to the slot pattern for temperature measurement on the side of the heat exchanger. Figure 3.3 shows the design mask layout of a die integrated with RTDs and Figure 3.4 shows only the mask layout for KOH process and the mask layout of Pt RTDs. Similarly, pressure sensors or flow sensors can be integrated into the silicon plates in the future.

3.2 Numerical Model

A numerical model was developed by our collaborators from the University of Wisconsin-Madison to estimate the performance of this perforated plate heat exchanger. The model was initially created by Hoch [Hoc06] based on the general model described by Nellis [Nel03]. A more comprehensive model was then written by White [Whi08] and will be summarized here (the context of White's model). More details, including the entire description of this model, computer code, case studies, etc., can be found in White's thesis [Whi08a]. All numerical models of this perforated plate heat exchanger were written in Engineering Equation Solver-EES [Kle02].

3.2.1 Governing Equations

In White's model, a standard heat exchanger model was developed in non-dimensional form and assumed the material thermophysical properties on each Si or glass plate are temperature independent because the fluid temperature difference across a

single plate within the heat exchanger is small. Figure 3.5 shows the computational grid in our heat exchanger numerical model.

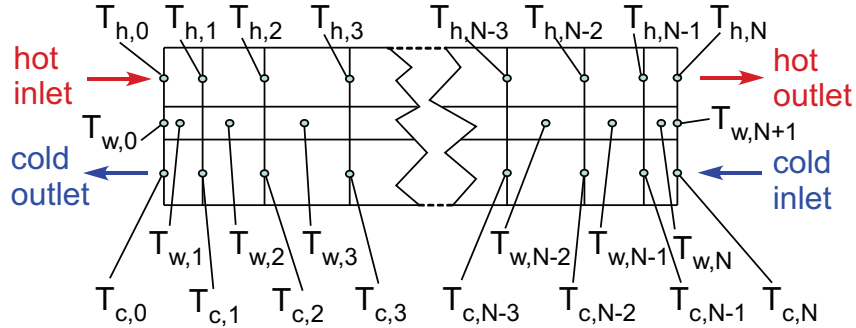


Figure 3.5: Location of nodes used for computational grid in heat exchanger numerical model.

The energy balance relationships at a node on (a) hot stream, (b) cold stream and (c) wall between both streams are illustrated in Figure 3.6. The energy balance equations for the hot stream, cold stream and wall in the i th section of the heat exchanger are shown in equations (3.1) to (3.3), respectively.

$$\text{Hot stream: } \mu_h \theta_{h,i-1} + \chi_h \Delta Z_i = \mu_h \theta_{h,i} + NTU_h \Delta Z_i \left(\frac{\theta_{h,i} + \theta_{h,i-1}}{2} - \theta_{w,i} \right) \quad (3.1)$$

where, μ_h is the hot side dimensionless capacity rate, $\mu_h = \dot{C}_h / \dot{C}_{\min}$, where \dot{C}_h is the hot side capacity rate, \dot{C}_{\min} is the minimum capacity rate of the two fluid streams; $\theta_{h,i}$ is the hot side dimensionless temperature at the i th node on the hot stream, $\theta_{h,i} = (T_{h,i} - T_{c,in}) / (T_{h,in} - T_{c,in})$, where $T_{h,i}$ is the hot side temperature at the i th node, $T_{h,in}$ is the hot fluid inlet temperature, and $T_{c,in}$ is the cold fluid inlet temperature; $\theta_{w,i}$ is the dimensionless temperature at the i th node on the wall between the hot stream and cold stream, $\theta_{w,i} = (T_{w,i} - T_{c,in}) / (T_{h,in} - T_{c,in})$, where $T_{w,i}$ is the temperature at the i th node on the wall; χ_h is the dimensionless term account for the parasitic heat load on the hot

stream, $\chi_h = \dot{q}_h / \dot{C}_{\min} (T_{h,in} - T_{c,in})$, where \dot{q}_h is the hot side parasitic heat load; ΔZ_i is the dimensionless width of an individual element, $\Delta Z_i = \Delta X / L$, where ΔX is the width of the element, L is the total length of the heat exchanger; NTU_h is the number of transfer unit on the hot stream, $NTU_h = U_h A_{s,h} / \dot{C}_{\min} = 1 / R_h \dot{C}_{\min}$, where U_h is the overall heat transfer coefficient on the hot stream, $A_{s,h}$ is the heat transfer surface area on the hot stream, and R_h is the stream-to-wall thermal resistance on the hot stream.

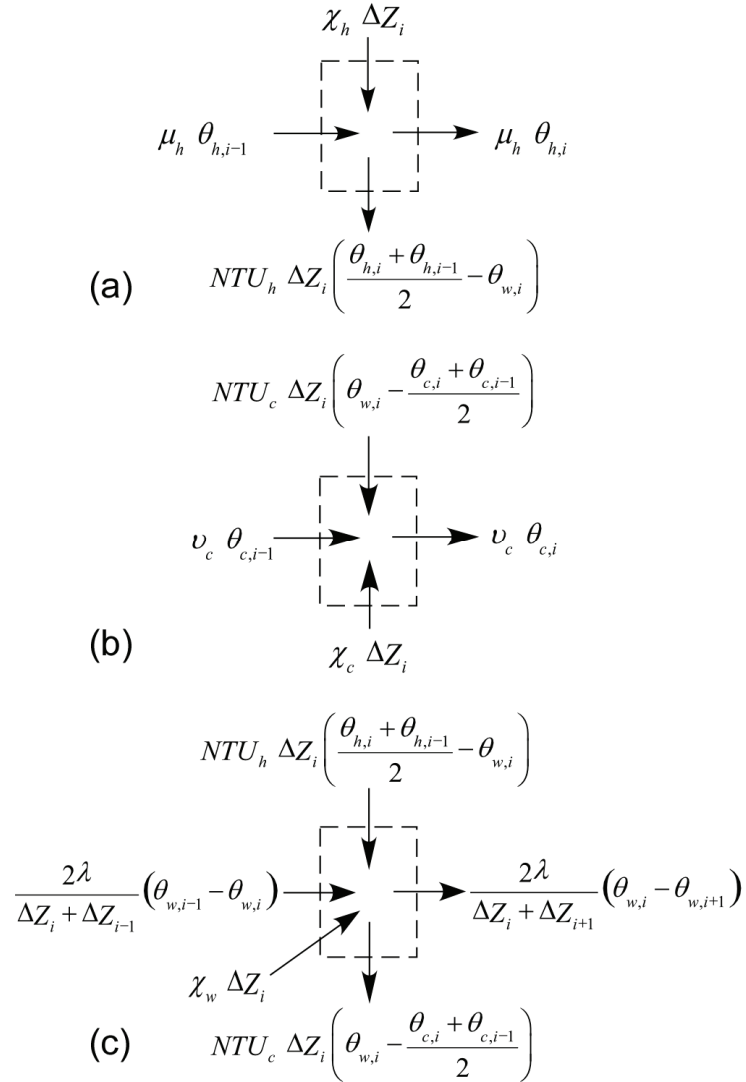


Figure 3.6: Energy balance diagram of (a) hot stream, (b) cold stream and (c) heat exchanger wall.

$$\text{Cold stream: } \chi_c \Delta Z_i + \nu_c \theta_{c,i} + NTU_c \Delta Z_i \left(\theta_{w,i} - \frac{\theta_{c,i} + \theta_{c,i-1}}{2} \right) = \nu_c \theta_{c,i-1} \quad (3.2)$$

where, ν_h is the hot side dimensionless capacity rate, $\nu_c = \dot{C}_c / \dot{C}_{\min}$, where \dot{C}_c is the cold side capacity rate; $\theta_{c,i}$ is the cold side dimensionless temperature at the i th node, $\theta_{c,i} = (T_{c,i} - T_{c,in}) / (T_{h,in} - T_{c,in})$, where $T_{c,i}$ is the cold side temperature at the i th node; χ_c is the dimensionless term accounting for parasitic heat load on the cold stream, $\chi_c = \dot{q}_c / \dot{C}_{\min} (T_{h,in} - T_{c,in})$, where \dot{q}_c is the cold side parasitic heat load; NTU_c is the number of transfer unit on the hot stream, $NTU_c = U_c A_{s,c} / \dot{C}_{\min} = 1 / R_c \dot{C}_{\min}$, where U_c is the overall heat transfer coefficient on the cold stream, $A_{s,c}$ is the heat transfer surface area on the cold stream, and R_c is the stream-to-wall thermal resistance on the cold stream.

$$\begin{aligned} \text{Wall: } & \chi_w \Delta Z_i + NTU_h \Delta Z_i \left(\frac{\theta_{h,i} + \theta_{h,i-1}}{2} - \theta_{w,i} \right) + \frac{2\lambda}{\Delta Z_i + \Delta Z_{i-1}} (\theta_{w,i-1} - \theta_{w,i}) = \\ & NTU_c \Delta Z_i \left(\theta_{w,i} - \frac{\theta_{c,i} + \theta_{c,i-1}}{2} \right) + \frac{2\lambda}{\Delta Z_i + \Delta Z_{i+1}} (\theta_{w,i} - \theta_{w,i+1}) \end{aligned} \quad (3.3)$$

where, χ_w is the dimensionless term account for parasitic heat load on the wall $\chi_w = \dot{q}_w / \dot{C}_{\min} (T_{h,in} - T_{c,in})$, where \dot{q}_w is parasitic heat load on the wall; λ is the dimensionless parameter of the axial conduction, $\lambda = k_w A_w / L \dot{C}_{\min} = 1 / R_{ac} \dot{C}_{\min}$, where k_w is the wall thermal conductivity, A_w is the cross sectional area for axial conduction, and R_{ac} is the axial thermal resistance.

In our numerical model of this perforated plate heat exchanger, each single silicon perforated plate is modeled as a simple heat exchanger with constant properties. The

governing equation (3.1)-(3.4) is therefore used to calculate the temperature distribution on each plate. This set of implicit equations is solved with a set of reasonable initial guess values in EES. The stream-to-stream heat transfer in the glass spacer is negligible because the glass spacers have much smaller surface area and lower thermal conductivity than the silicon plates. However, the heat transfer along the flow direction (axial conduction) on both the silicon and glass plates cannot be ignored because the thickness of these plates is small. Therefore, the wall boundary conditions on each silicon plate cannot be treated as adiabatic condition or constant temperatures.

Two new dimensionless parameters were defined to account for heat transfer to and from the ends of the heat exchanger. Similar to the parasitic heat loads, the dimensionless wall end conduction parameters were defined by dividing the specified edge conduction rates by the maximum possible stream-to-stream heat transfer rates. Equation (3.4) and (3.5) show these parameters on the hot and cold end of the heat exchanger, respectively.

$$\chi_{w,h} = \frac{\dot{q}_{w,h}}{\dot{C}_{\min}(T_{h,in} - T_{c,in})} = \frac{\lambda(\theta_{w,0} - \theta_{w,1})}{\Delta Z_0} \quad (3.4)$$

$$\chi_{w,c} = \frac{\dot{q}_{w,c}}{\dot{C}_{\min}(T_{h,in} - T_{c,in})} = \frac{\lambda(\theta_{w,N} - \theta_{w,N+1})}{\Delta Z_{N+1}} \quad (3.5)$$

where $\chi_{w,h}$ and $\dot{q}_{w,h}$ are the dimensionless and dimensional quantities of heat conducted to the hot end of the heat exchanger, respectively; $\chi_{w,c}$ and $\dot{q}_{w,c}$ are the dimensionless and dimensional quantities of heat conducted from the cold end of the heat exchanger, respectively.

3.2.2 Model Description

3.2.2.1 Die Geometry

Similar to the temperature calculation, the heat transfer and pressure drop correlations used in the design model are also implemented in dimensionless form. Figure 3.2 shows the major geometric parameters of a silicon die (silicon plate) and a glass die (glass spacer). According to the approach to calculate flow convection in a duct (slot in the silicon pattern), the aspect ratio of the slot α is defined as the ratio of the height of slot H_{slot} to the width of the slot W_{slot} :

$$\alpha = \frac{H_{slot}}{W_{slot}} \quad (3.6)$$

The concept of a hydraulic diameter was developed in order to define the characteristic dimension for flow through a duct with non-circular cross section. The hydraulic diameter, D_{hyd} , can be calculated using Eq. (3.7):

$$D_{hyd} = \frac{4A_{flow}}{P_{wetted}} = \frac{4(W_{slot}H_{slot})}{(2W_{slot} + 2H_{slot})} \quad (3.7)$$

where A_{flow} is the cross sectional area for fluid flow and P_{wetted} is the “wetted” perimeter of the cross sectional area for fluid flow.

3.2.2.2 Thermal Conductivity

Continuing within White’s model, when the temperature decreases from the room temperature to the cryogenic temperature, the thermal conductivity of a material usually changes by an order of magnitude or more. Consequently, it is inaccurate to assume that the thermal conductivity of each material inside the heat exchanger is constant. Even if

the average temperature in the heat exchanger is used, the error of the model is still significant.

Generally, the thermal conductivity of single crystal silicon depends on the crystal orientation. However, when the temperature is above 30 K, the thermal conductivities of the single crystal silicon in all orientations have less than 10% difference [McK70]. Since the heat exchanger will be used in temperature from 100 K to 300 K, the effect of crystal orientation is negligible. Doping and oxygen concentration, on the other hand, play a significant role on altering the thermal conductivity of silicon. Based on the comparison of thermal conductivity on different silicon samples [Tou70], a set of thermal conductivity data is included in the model. Similarly, thermal conductivity data at the cryogenic temperature range is not available for BOROFLOAT® borosilicate glass, which was used as the glass spacer in our process. An estimated thermal conductivity curve derived from Cryocomp™ is used in the model. More details of the thermal conductivities of silicon and BOROFLOAT glass in this model are available in [Whi08a].

3.2.2.3 Laminar Flow Heat Transfer and Pressure Drop Correlations

In the laminar flow, the laminar frictional pressure drop ($\Delta P_{friction,lam}$), the pressure drop due to fluid contraction ΔP_{cont} and expansion ΔP_{exp} as the fluid flows in and out of the slot pattern are three major pressure drop. These three pressure drops can be calculated in Eq. (3.8)-(3.10).

$$\Delta P_{friction,lam} = f_{app,lam} \rho \frac{x}{D_{hyd}} \frac{V_m^2}{2} \quad (3.8)$$

$$\Delta P_{cont} = \rho K_{cont} \frac{V_m^2}{2} \quad (3.9)$$

$$\Delta P_{\text{exp}} = \rho K_{\text{exp}} \frac{V_m^2}{2} \quad (3.10)$$

where $f_{\text{app},\text{lam}}$ is the fully developed friction factor for rectangular slot, ρ is the fluid density, x is the axial distance along the slot, V_m is the mean fluid velocity in the slot, K_{cont} is the contraction loss coefficient and K_{exp} is the expansion loss coefficient. Both K_{cont} and K_{exp} is conservatively assumed to be one in our model so that the pressure drop is not underestimated. Therefore, the total pressure drop can be calculated in Eq. (3.11):

$$\Delta P_{\text{tot},\text{lam}} = \Delta P_{\text{cont}} + \Delta P_{\text{friction},\text{lam}} + \Delta P_{\text{exp}} \quad (3.11)$$

The Nusselt number for fully developed laminar flow through a rectangular slot is sensitive to the thermal boundary conditions applied. Furthermore, the silicon slot pattern cannot be simply defined as constant wall temperature or constant wall heat flux. Because the thickness is so small and the temperature along this direction (x direction) is close to a constant temperature, but the temperature distribution on the direction along the long edges of slots (y direction) is very significant. Assuming a constant heat flux is also incorrect because of this temperature gradient along the slot patterns. In our model, the Nusselt number is calculated by Eq. (3.12) which is modified from the parallel plate Nusselt number correlation.

$$Nu_{T,m,10\text{mm}} = 6.88 + \frac{0.024(x_{10\text{mm}}^*)^{-1.14}}{1 + 0.0358(x_{10\text{mm}}^*)^{-0.64} \text{Pr}^{0.17}} \quad (3.12)$$

where $x_{10\text{mm}}^*$ is the thermal dimensionless length and can be calculated in Eq. (3.13), Pr is the Prandtl number of the fluid.

$$x^* = \frac{x}{D_{\text{hyd}} \text{Re} \text{Pr}} \quad (3.13)$$

where Re is the Reynolds number of the fluid.

3.2.2.4 Turbulent Flow Heat Transfer and Pressure Drop Correlations

Turbulent flow may be developed in some silicon plates in the heat exchanger. Based on the experimental investigations on the critical Reynolds number from transition from laminar to turbulent flow by Kakac et al. [Kak87], the critical Reynolds number in the slot pattern is estimated to be 3000, when the aspect ratio of these slots is near 0.05 and the entrance of the slot is abrupt. The total pressure drop can be calculated by Eq. (3.14).

$$\Delta P_{tot,turb} = \Delta P_{cont} + \Delta P_{friction,turb} + \Delta P_{exp} \quad (3.14)$$

where the turbulent frictional pressure drop can be calculated by Eq. (3.15)

$$\Delta P_{friction,turb} = f_{fd,turb} \rho \frac{x}{D_{hyd}} \frac{V_m^2}{2} \quad (3.15)$$

The friction factor for the fully developed turbulent flow can be calculated in Eq. (3.16)-(3.17) recommended by Kakac. The Nusselt number then can be calculated in Gnielinski equation, shown in Eq. (3.18), regardless the boundary condition.

$$f_{fd,turb} = (1.0875 - 0.2225\alpha) f_c \quad (3.16)$$

$$f_c = 4 \left(\frac{1}{1.7372 \ln \left(\frac{Re}{1.964 \ln(Re) - 3.8215} \right)} \right)^2 \quad (3.17)$$

$$Nu_{fd,turb} = \frac{(f_{fd,turb} / 8)(Re - 1000) Pr}{1 + 12.7 \sqrt{f_{fd,turb} / 8} (Pr^{2/3} - 1)} \quad (3.18)$$

No correlation for the apparent friction factor was found for developing turbulent flow. Equations (3.16)-(3.18) are then used for iterative calculation in EES for an

estimation of the Nusselt number in this case. However, the friction factor should be replaced to $f_{app,turb}$ in these equations.

The heat transfer coefficient, htc , can be calculated in Eq. (3.19).

$$htc = \frac{Nu \cdot k}{D_{hyd}} \quad (3.19)$$

where the Nusselt number is calculated by Eq. (3.12) for laminar flow or Eq. (3.18) for turbulent flow.

3.2.2.5 Fin Effectiveness

Fin effectiveness is defined as the ratio of the actual rate of heat transfer from the fins to the maximum possible rate of heat transfer, shown in Eq. (3.20). The fin discussed in this chapter is the silicon beam that is between two slot openings.

$$\varepsilon_{fin} = \frac{\dot{q}_{fin,act}}{\dot{q}_{fin,max}} = \frac{\dot{m}_{fluid} Cp_{fluid} (T_{fluid,in} - T_{fluid,out})}{\dot{m}_{fluid} Cp_{fluid} (T_{fluid,in} - T_{fluid,base})} \quad (3.20)$$

where \dot{m}_{fluid} is the fluid mass flow rate, Cp_{fluid} is the fluid specific heat at constant pressure, $T_{fluid,in}$ is the fluid temperature at the slot inlet, $T_{fluid,out}$ is the fluid temperature at the slot outlet, $T_{fin,base}$ is the temperature at the base of the fin. However, $T_{fluid,out}$ is generally unknown and ε_{fin} cannot be calculated by Eq. (3.20). Nellis and Klein [Nel06] found that the fin effectiveness is a function of three non-dimensional parameters and can be numerically calculated by Eq. (3.21).

$$\varepsilon_{fin} = 1 - \exp\left[-a(\beta)NTU^{(b(\beta)+c(\beta)\ln(NTU))}\right] \quad (3.21)$$

where NTU is the number of heat transfer units and can be determined in Eq. (3.22); β is the fin constant and can be determined in Eq. (3.23), $a(\beta)$, $b(\beta)$, $c(\beta)$ can be

determined in a set of numerical equations with constant parameters [Whi08a]

$$NTU = \frac{2W_{fin}t_{fin}htc}{\dot{m}_{fluid}Cp_{fluid}} \quad (3.22)$$

where W_{fin} is the width of the fin, shown in Fig. 3.2a, t_{fin} is the thickness of the fin in flow direction, thus thickness of the silicon wafer.

$$\beta = W_{fin} \sqrt{\frac{2htc}{k_{fin}H_{fin}}} \quad (3.23)$$

where H_{fin} is the height of the fin, shown in Fig. 3.2a, k_{fin} is the thermal conductivity of the fin material.

3.2.2.6 Thermal Resistances

In White's mode, the total thermal resistance of a single die is determined in order to calculate the heat transfer rate between the hot and the cold streams. Figure 3.7 shows the four thermal resistances on a single dies

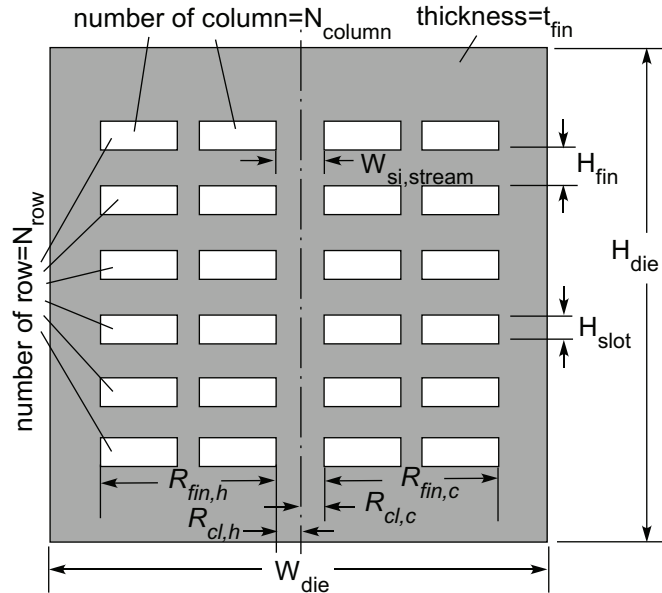


Figure 3.7: Four thermal resistances in serial for heat conduction between the hot and cold fluid streams.

The fin resistances on the hot side $R_{fin,h}$ and the cold side $R_{fin,c}$ can be calculated in Eq. (3.24)-(3.25).

$$R_{fin,h} = \frac{1}{\varepsilon_{fin,h} \dot{m}_{fluid,h} C_{p,fluid,h}} \quad (3.24)$$

$$R_{fin,c} = \frac{1}{\varepsilon_{fin,c} \dot{m}_{fluid,c} C_{p,fluid,c}} \quad (3.25)$$

The center strip resistance on both the hot side $R_{cl,h}$ and the cold side $R_{cl,c}$ can be calculated in Eq. (3.26), since the pattern is symmetrical along the center line.

$$R_{cl,h} = R_{cl,c} = \frac{(W_{si,stream} / 2)}{k_{si} t_{fin} H_{die}} \quad (3.26)$$

where k_{si} is the silicon thermal conductivity, the dimensions $W_{si,stream}$, t_{fin} , H_{die} are shown in Fig. 3.7.

As a result, the total resistance of the silicon plate can be calculated by the sum of these four resistances, and shown in Eq. (3.27). The total heat transfer rate between the two streams on one single die can be determined in Eq. (3.28)

$$R_{tot,die} = R_{fin,h} + R_{cl,h} + R_{cl,c} + R_{fin,c} \quad (3.27)$$

$$\dot{q}_{tot,die} = \frac{(T_{fluid,h} - T_{fluid,c})}{R_{tot,die}} \quad (3.28)$$

where $T_{fluid,h}$ and $T_{fluid,c}$ are the fluid temperature entering the hot and the cold side, respectively.

3.2.2.7 Axial Conduction

The axial conduction in the heat exchanger can significantly degrade the performance in the J-T cycle. The axial conduction resistances of a silicon perforated

plate and a glass spacer are calculated in Eq. (3.29) and (3.30), respectively.

$$R_{ac,si} = \frac{t_{fin}}{k_{si} A_{si,cond}} \quad (3.29)$$

$$R_{ac,sp} = \frac{t_{sp}}{k_{sp} A_{sp,cond}} \quad (3.30)$$

where $A_{si,cond}$ and $A_{sp,cond}$ are the surface area of the silicon perforated plate and the glass spacer normal to the direction of axial heat flow, respectively, t_{sp} is the thickness of the glass spacer, k_{sp} is the thermal conductivity of the glass spacer and is evaluated at the average wall temperature for the spacer.

3.2.2.8 Parasitic Heat Loads

Three major parasitic heat loads are included in this model: radiation from the vacuum vessel wall \dot{q}_{rad} , thermal conduction from the measurement leads of Pt RTDs \dot{q}_{wire} and ohmic dissipation in the Pt RTDs \dot{q}_{ohmic} .. The model implements these heat loads into each side on a single die so that the heat transfer and temperature distribution inside each die are more accurate. Radiation inside the heat exchanger is believed to have small effect on the temperature distribution and is therefore negligible in our model. Eq. (3.31) and (3.32) is used to calculate the total parasitic heat load on the hot $\dot{q}_{phl,h,j}$ and the cold $\dot{q}_{phl,c,j}$ side of the j th die, respectively.

$$\dot{q}_{phl,h,j} = \dot{q}_{rad,h,j} + \dot{q}_{wire,h,j} + \dot{q}_{ohmic,h,j} \quad (3.31)$$

$$\dot{q}_{phl,c,j} = \dot{q}_{rad,c,j} + \dot{q}_{wire,c,j} + \dot{q}_{ohmic,c,j} \quad (3.32)$$

where subscript h represents the hot side, subscript c represents the cold side, subscript j represents the j th die in the heat exchanger from the hot end of the heat exchanger.

3.2.3 Design Geometries

Based on the model described before, the optimal design geometries that can be realistically fabricated in a micromachining process were determined. Table 3.1 shows the major geometries of a silicon perforated plate and a glass spacer for a heat exchanger with $10 \times 10 \text{ mm}^2$ cross section (die size). According to Hoch's model [Hoc06], our perforated plate heat exchanger can provide up to 5-10 W at a temperature range of 150-200 K at a mixed gas pressure of 2 MPa when there is no parasitic heat load.

Table 3.1: Summary of geometric parameters and operating conditions

Si plate			Glass spacer		
Description	Variables	Dimension	Description	Variables	Dimension
Width of die	W_{die}	9770 μm	Width of die	W_{die}	9770 μm
Height of die	H_{die}	9770 μm	Height of die	H_{die}	9770 μm
Width between stream on Si die	$W_{\text{si,stream}}$	1500 μm	Width between stream on glass die	$W_{\text{g,stream}}$	700 μm
Width of Si slot	W_{duct}	1400 μm	Width of glass window	W_{gw}	3700 μm
Height of Si slot	H_{duct}	50 μm	Height of glass window	H_{gw}	8150 μm
Width of Si web	W_{web}	10 μm	Thickness of glass spacer	t_{sp}	300 μm
Width of each Si fin row	W_{fin}	2900 μm			
Height of each Si fin row	H_{fin}	50 μm			
Thickness of Si die	t_{fin}	500 μm			
Number of slot column	N_{column}	2			
Number of slot row	N_{row}	74			

3.3 Device Fabrication

3.3.1 Fabrication Process

A four-mask, eleven-step fabrication process [Zhu07, Zhu08] is required for fabricating this heat exchanger and described below (Fig. 3.8).

1&2) The Si slot patterns are etched through by a double-side KOH process on (110) Si wafers [Mad97, Chi99]. This process can provide four vertical (111) sidewalls out of six and is suitable for batch fabrication since the minimum feature of the slot patterns is as large as 50 μm . More details about this process will be discussed in the

next section. This wet etching process is more cost effective and suitable for our process than plasma dry etching. A 500 μm thick double-side polished (110) Si wafer is patterned with LPCVD oxide/nitride layers on both sides. A symmetrical lithographic mask is used in this step. With oxide/nitride as the etching mask, the wafer is dipped into KOH solution. Slot patterns are simultaneously etched through from both sides and vertical side walls are formed on long edges of the slots in this KOH process. The oxide/nitride masks are then striped and 100 nm thick new oxide layers are deposited on both sides as insulation layer. Accurate backside alignment is necessary in this step.

3) Pt RTD deposition. 5 nm/100 nm Ti/Pt thin film is deposited and patterned (in a lift-off process) on only one side to form Pt RTDs on the Si substrate. Dies without thin film Pt RTD are also fabricated in the same process by masking Ti/Pt deposition with a photoresist layer (in the same lift-off process).

4-6) The glass windows are fabricated with a two-step HF:HNO₃ wet etching process from a 300 μm thick Pyrex wafer. Cr/Au layers are used in this wet etching process. In the first step of glass etching, 20 μm deep recesses are etched on one side and a new Cr/Au layer is sputtered on the same surface and good sidewall coverage on these shallow recesses is achieved.

7&8) In the second step of glass etching, the Cr/Au layers on both sides are patterned with a symmetrical mask. The wafer is then simultaneously etched from both sides in the HF:HNO₃ solution and finally etched through when the glass windows are formed.

9&10) The patterned Si wafer and glass wafer are then anodically bonded together. The wafer stack is then diced into many small dies.

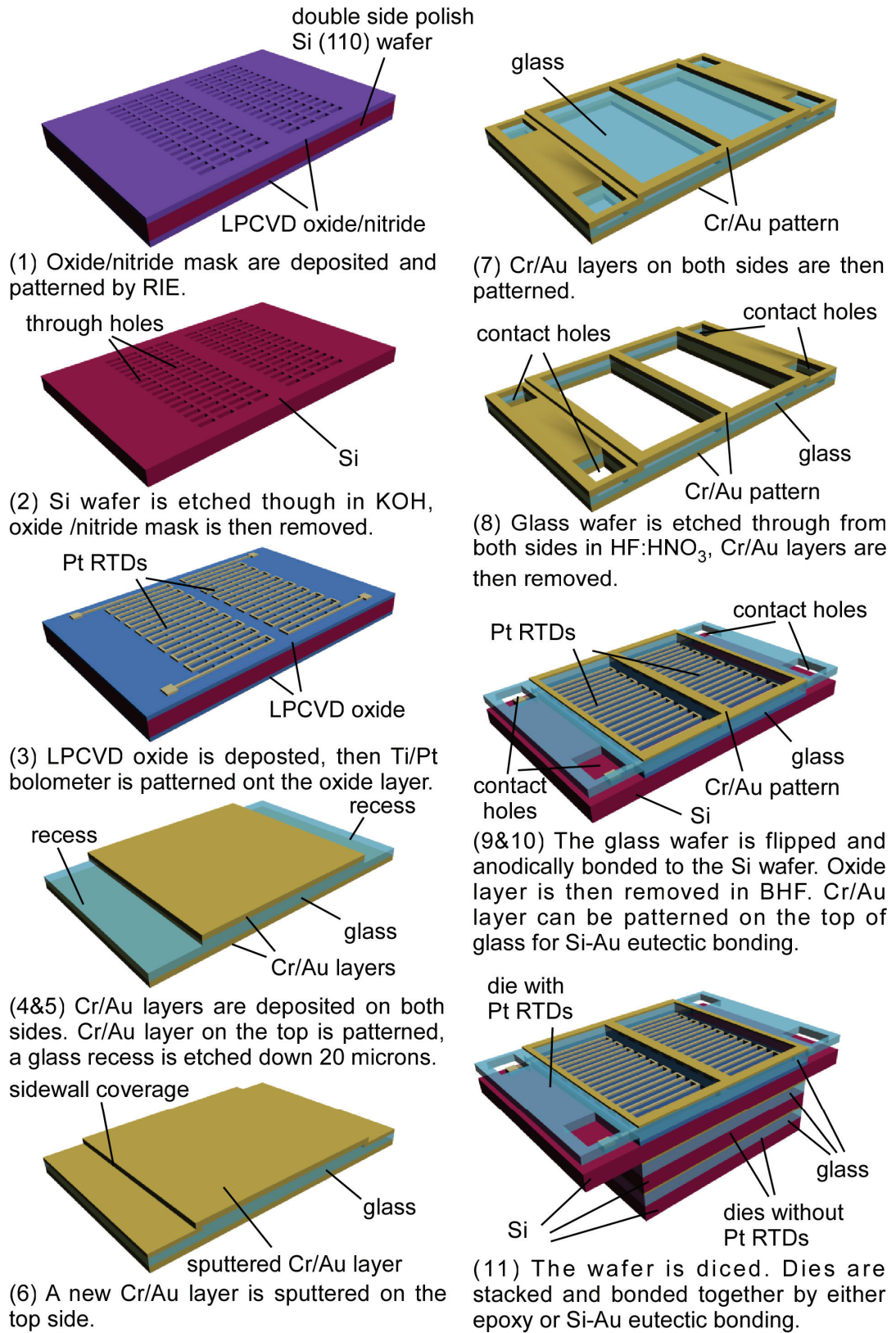


Figure 3.8: Fabrication process of the perforated plate Si/glass heat exchanger with Pt RTDs.

11) Two different methods are used for bonding the Si/glass stack: a) Epoxy STYCAST 2850FT (Emerson & Cuming, Inc., Billerica, MA, USA) is used to separately bond Si/glass dies . b) Si-Au eutectic bonding [Wol94, Mit05] is used to simultaneously bond the Si/glass heat exchanger stack. Details of these two methods will be discussed in section 3.4.2.3.

Although several heat exchangers were successfully fabricated, some were not leak tight. As will be discussed in the next section, the quality of the Si-Au eutectic bonding is not consistent due to the limitations of available equipment. And a heat exchanger that has more than 25 dies is difficult to fabricate with such a method. All the leak tight heat exchangers tested in our experiments were fabricated using epoxy. To this point, the epoxy method has proved to be reliable and the heat exchanger has been tested numerous times at pressures up to 1 MPa for six months without any leakage detected.

3.3.2 Related Fabrication Techniques

3.3.2.1 KOH Etching on (110) Si Wafer

In order to fabricate the silicon slot pattern on a standard 500 μm thick silicon wafer, an etching technique that could form high-aspect-ratio trenches perpendicular to the silicon substrate is desired. DRIE dry etching, which was used in the through-wafer silicon etching for the planar heat exchanger, can produce such tranches. However, the DRIE process is a very high-cost, low-efficient process. Furthermore, similar to the fabrication for planar design, the uniformity issue across the wafer is still a potential challenge for slot patterns due to its large total opening area. KOH anisotropic etching is a low-cost alternative way to fabricate the slot pattern. This process is based on the fact

that Si has different etch rates in different crystal planes in a KOH solution. (111) crystal plane is etched much slower than (110) and (100) planes. Traditionally, numerous MEMS applications utilize KOH etching on (100) silicon wafers to form microstructures with four non-vertical sidewalls [Mad99]. However, this is not suitable for our slot pattern because the aspect-ratio of our slot pattern is about 1:10 (50 μm width: 500 μm depth) and the four (111) planes will self-terminate in the KOH process. A larger slot pattern could be used to avoid the self-termination in (100) silicon KOH process, but the opening area at the bottom side will be cut to about a quarter. This modification will reduce the total number of slot rows on a silicon die and consequently, the slot pattern is no longer optimal for the heat exchanger performance.

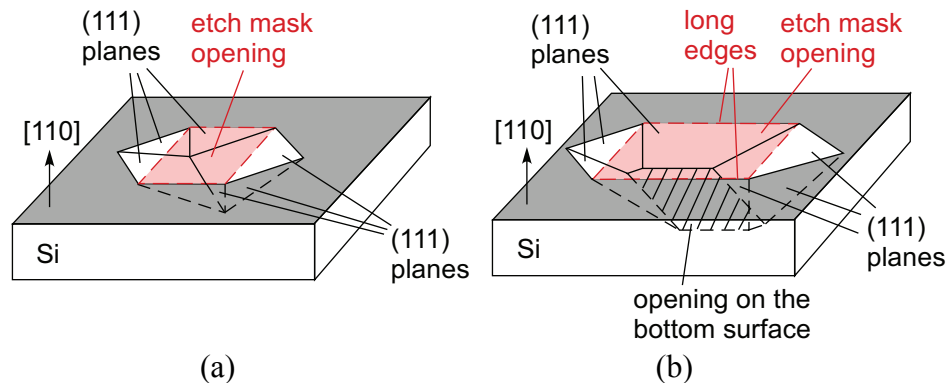


Figure 3.9: Six (111) planes on a (110) wafer after KOH process. (a) the hole is self-terminated if the edges on the mask are too short; (b) the hole is etched through the wafer if the long edges on the mask are long enough.

Given that the silicon slot pattern in our design has two long edges (1400 μm) and two very short edges (50 μm), a novel KOH process on (110) silicon wafers was developed to fabricate a pattern with vertical sidewalls. Fig. 3.9 shows six (111) planes in (110) silicon wafer after KOH etching. The etch stops on six (111) planes because the etch rate on those planes is very slow ($<0.01 \mu\text{m}/\text{min}$). The transparent red areas in Fig. 3.9 are the openings of the etch masks. Of the six (111) planes, four planes are

perpendicular to the (110) surface; these four planes are either parallel or have an angle of 109.47° with each other. The other two (111) planes that intersect (110) surface with an angle 35.26° . When the opening on the mask is small or the edges are short, these two (111) planes intersect with an angle 109.47° as shown in Fig. 3.9a. When the opening is big enough or the long edges on the mask are long enough, these two planes do not intersect before the hole is etched through.

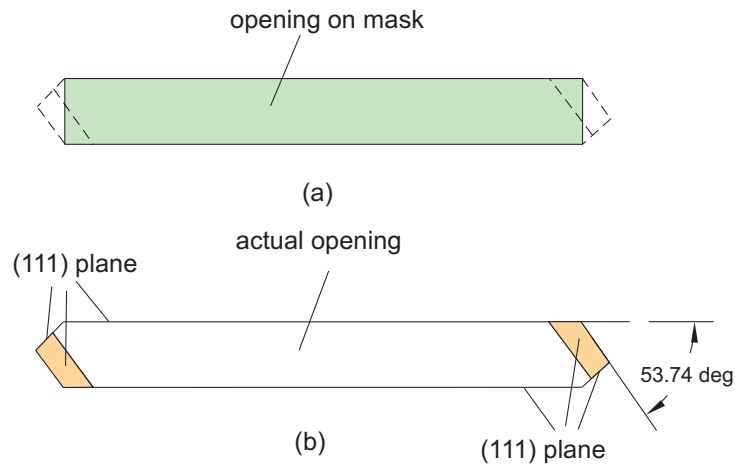


Figure 3.10: Actual opening of the slots after KOH on a (110) wafer: (a) with mask and (b) without mask.

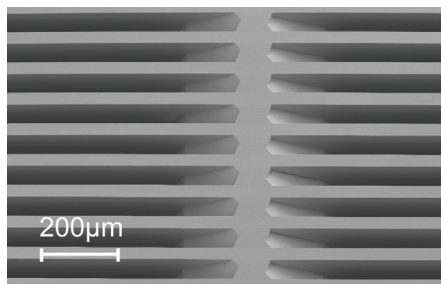


Figure 3.11: SEM photo of actual openings of the slot pattern after KOH.

In order to obtain the slot pattern, the pair of long edges on the etch mask should align with a pair of vertical (111) planes in order to produce a vertical sidewall on these two edges. Generally, this can be achieved by aligning the long edges parallel to the primary flat of the (110) silicon wafer. Fig. 3.10 shows schematic diagrams of the top

views of a rectangle mask and the actual opening after the KOH process. The relationships between each (111) plane is the same as those shown in Fig. 3.10b. Therefore, with perfect alignment between the mask and primary flat ([111] direction) on the (110) wafer, the actual opening along the long edge is slightly longer than the original opening on the mask. More details about misalignments and defects in the KOH process are discussed in Appendix B. Figure 3.11 shows the SEM of the fabricated slot patterns after KOH.

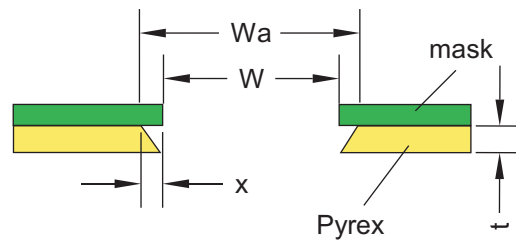


Figure 3.12: Isotropic HF etching. x is the lateral undercut; t is the etch depth (wafer thickness in our case); W is the designed width; W_a is the actual width.

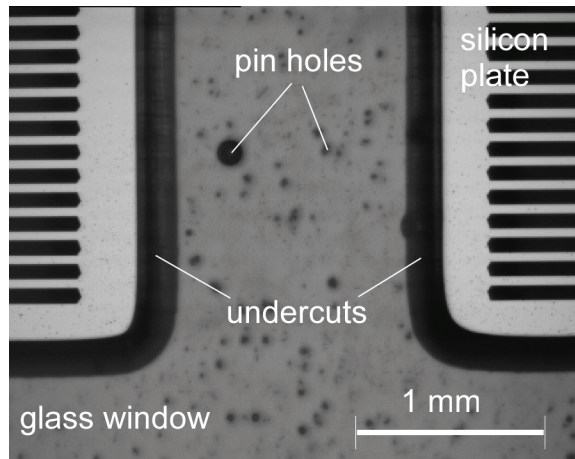


Figure 3.13: Microscopic photo of a HF:HNO₃ wet etching processed glass wafer bonded on a silicon substrate.

3.3.2.2 HF:HNO₃ Glass Etching

HF:HNO₃ solution is commonly used for etching glass wafers in various MEMS applications. Because HF wet etching is isotropic, the lateral undercut beneath the mask

is unavoidable in this process. Our process requires an optimal HF wet etching process for 300 μm deep etching when the lateral undercut is minimized. In Fig. 3.12, the lateral undercut x varies depending on the batch of wafers and HF solutions. The ratio of etch depth to lateral undercut t/x is no less than 1:1.2. With the thickness of the wafer between 250 to 300 μm , the lateral undercut is estimated to be around 350 μm . Hence, the actual glass window is increased 700 μm in each edge. Fig. 3.13 shows a microscopic photo of a fabricated glass spacer bonded to a silicon substrate. The etch process was limited to 30 min in order to avoid causing the Cr/Au mask layer to peel off. Pin holes on the glass wafer, which result in voids in the subsequent anodic bonding step and affect the bonding quality, are minimized by using a thick Cr/Au mask layer.

3.3.2.3 Die-Level Si/Glass Stack Bonding

The last step of the fabrication process is to assemble the Si/glass dies together to form a long heat exchanger. In the design stage, the Si/glass dies were designed to large misalignment such that it is sufficient to align the dies along the diced edges in the final assembly step. However, bonding a Si/glass stack composed of 20-50 Si/glass dies is still challenging. As the total thickness of the stack is 16-40 mm, a conventional commercially available bonder cannot be used for this bonding process. Two methods were developed to bond the stack and will be discussed as follows.

STYCAST Epoxy Bonding

Epoxy is commonly used to bond substrates as an intermediate layer. This method has low cost and requires no mask. Before the epoxy is cured and hardened, the epoxy

can easily fill the gaps or holes on the substrates. As a result, this method can tolerate impurities and defects on the substrates. However, because the heat exchanger has to sustain very high pressure at low temperatures, the epoxy used in our process has to be very strong at a wide range of low temperatures while maintaining minimum thermal stress. STYCAST 2850FT epoxy with catalyst 23LV (Emerson & Cuming, Inc., Billerica, MA, USA) is used in our process. This epoxy is widely used in cryogenic applications and has proved to be very reliable in cryogenic temperatures. Several relevant properties of this epoxy are listed in Table 3.2.

Table 3.2: Properties of STYCAST 2850FT with catalyst 23LV

Properties	Unit	Value
Hardness	Shore D	92
Flexural Strength	MPa	106
Compressive Strength	MPa	120
Thermal Expansion Coefficient	$10^{-6}/^{\circ}\text{C}$	39.4
Thermal Conductivity	W/m-K	1.02
Dielectric Constant @1MHz	-	5.36
Working time at 25°C	min	60
Curing time at 25°C	hour	16-24

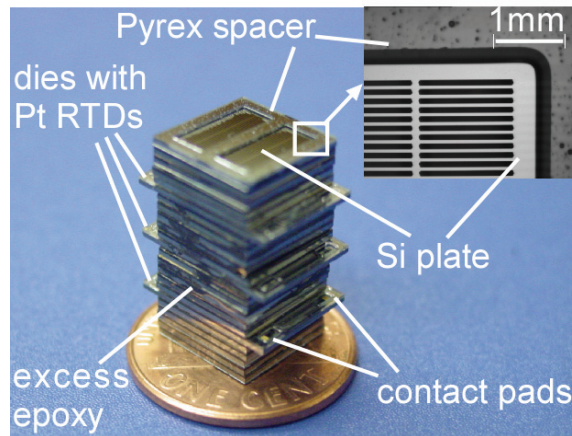


Figure 3.14: Heat exchanger boned by STYCAST 2850FT epoxy. The total length is about 2 cm (25 dies).

In this process, the Si/glass dies are bonded one-by-one after manual alignment. Before the epoxy is cured, a weight of 200 g is added from the top of the stack for epoxy reflow. Simultaneously bonding the Si/glass stack was attempted but resulted in a shift of alignment and occasional leakage on the bonding interfaces because of the limited working time of the epoxy. Hence, bonding the Si/glass dies individually is still the most reliable and consistent way to fabricate the heat exchanger stack.

Figure 3.14 shows a fabricated $1 \times 1 \text{ cm}^2$ heat exchanger with 25 dies bonded by epoxy. The die size of perforated plate micro heat exchanger is $1 \times 1 \text{ cm}^2$. The thickness of the Si plate in each die is $500 \text{ }\mu\text{m}$. The thickness of the Pyrex spacer is $300 \text{ }\mu\text{m}$. Two rows of opening slots are on both high-pressure and low-pressure sides of the Si plate. The slot is $50 \text{ }\mu\text{m}$ wide and $1400 \text{ }\mu\text{m}$ long; there is $50 \text{ }\mu\text{m}$ gap between each slot. Dies with Pt RTDs are selectively bonded to the heat exchanger.

Die-Level Si-Au Eutectic Bonding

Si-Au eutectic bonding [Wol94, Mit05] is another approach to simultaneously bond the Si/glass heat exchanger stack. This requires an additional mask for patterning a Cr/Au layer before dicing but avoids the tedious procedure of bonding Si/glass dies separately. The Si/glass dies are aligned and then stacked together. A weight of 1 kg is applied on the top of the stack before the heat exchanger stack is heated up to $500 \text{ }^\circ\text{C}$ in an oven.

A $1 \times 1 \text{ cm}^2$ heat exchanger (25 dies) integrated with Pt RTDs fabricated by Si-Au bonding is shown in Fig. 3.14. This bonding process is not consistent. First, the pressure applied to the heat exchanger stack is not balanced well. The surfaces on the dies are not

perfect and a small particle on a surface can tilt the entire stack on the top of this surface and results in an unbalanced force applied to the stack. Second, since the Si-Au bonding is not completed in a vacuum environment, the native oxide on the silicon substrate will degrade the quality of the Si-Au eutectic bonding. The bonding temperature is therefore increased to nearly 500 °C, which is much higher than the Si-Au eutectic temperature 363 °C. Moreover, at a higher temperature, gold can reflow and fill the pin holes on the glass wafer and result in a better seal.

Fig. 3.15 shows a Si-Au eutectic bonded heat exchanger (25 dies) with RTDs dies. Many of these Si-Au eutectic bonded heat exchangers have been prone to leaks or lack of strength in the subsequent leak test and pressure test. For these reasons, this die-level Si-Au eutectic bonding process needs further improvement in many different steps.

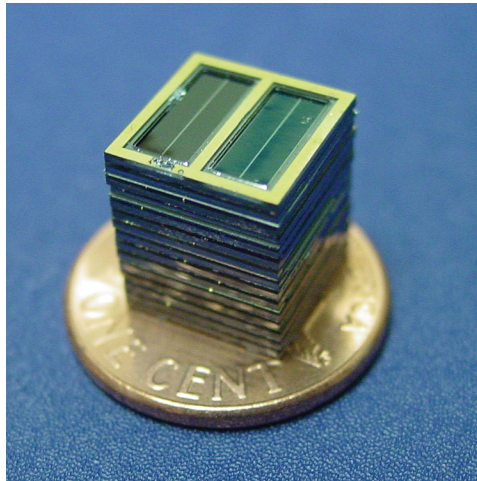


Figure 3.15: A $1 \times 1 \text{ cm}^2$ heat exchanger (without Pt RTDs) fabricated by Si-Au eutectic bonding. The Dies with Pt RTDs are equally distributed across the entire length of the micro heat exchanger. The total length is about 1.6 cm (20 dies).

3.3.3 Discussion of Fabrication

As discussed in the previous sections, several fabrication process steps were developed or improved. These led to a simple and low-cost fabrication process for our

micromachined perforated plate heat exchanger. A new KOH wet etching process on (110) silicon wafers was developed to fabricate slot patterns. The 300 μm thick glass spacer was fabricated by double side HF:HNO₃ wet etching. Finally, two different bonding processes were developed for bonding the heat exchanger stack. The epoxy method has been reliable and consistent although it is tedious. The Si-Au eutectic bonding, which can simultaneously bond the heat exchanger stack, requires further improvement to fabricate a robust and leak tight heat exchanger.

The longest heat exchanger fabricated is a 43 die heat exchanger (3.5 cm long) integrated with Pt RTDs. This heat exchanger was bonded with STYCAST epoxy and has proved to be strong enough to sustain 1 MPa pressure without any internal and external leakage. The experimental results that will be presented in the rest of this chapter have been primarily obtained from this heat exchanger. More details of assembly, installation and tests will be discussed in the following sections.

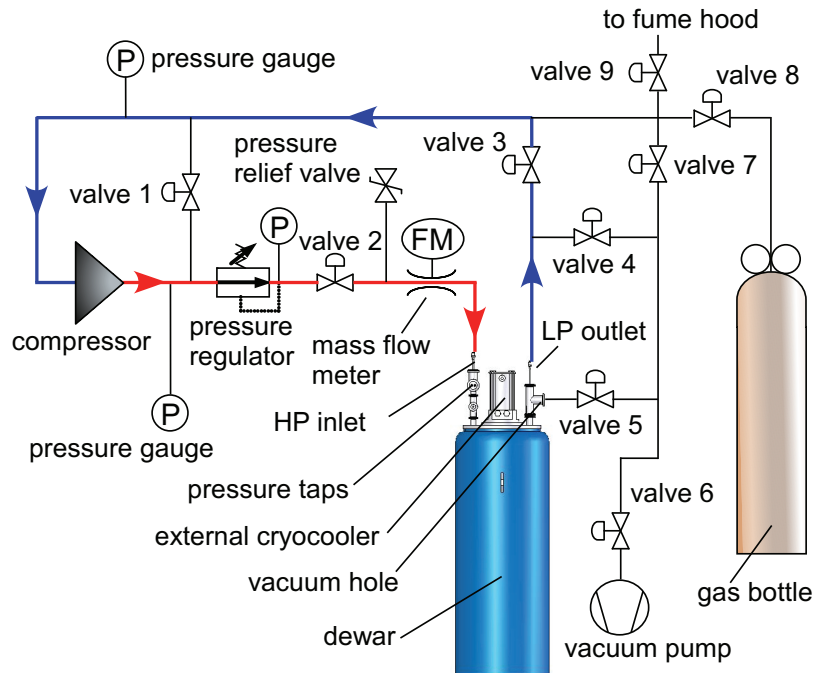


Figure 3.16: Flow schematic of the cryogenic test facility outside the dewar.

3.4 Cryogenic Test Facilities

3.4.1 Schematics and Operation Modes

A comprehensive test facility was designed and assembled for tests of heat exchangers. The flow schematic diagrams of both outside and inside the dewar are shown in Fig. 3.16 and Fig. 3.17. A compressor and a pressure regulator are interfaced with the test facility for a closed loop cycle, and accordingly, provide continuous test data. This closed loop system has been proved to be robust and reliable by more than 240 hours of uninterrupted operation.

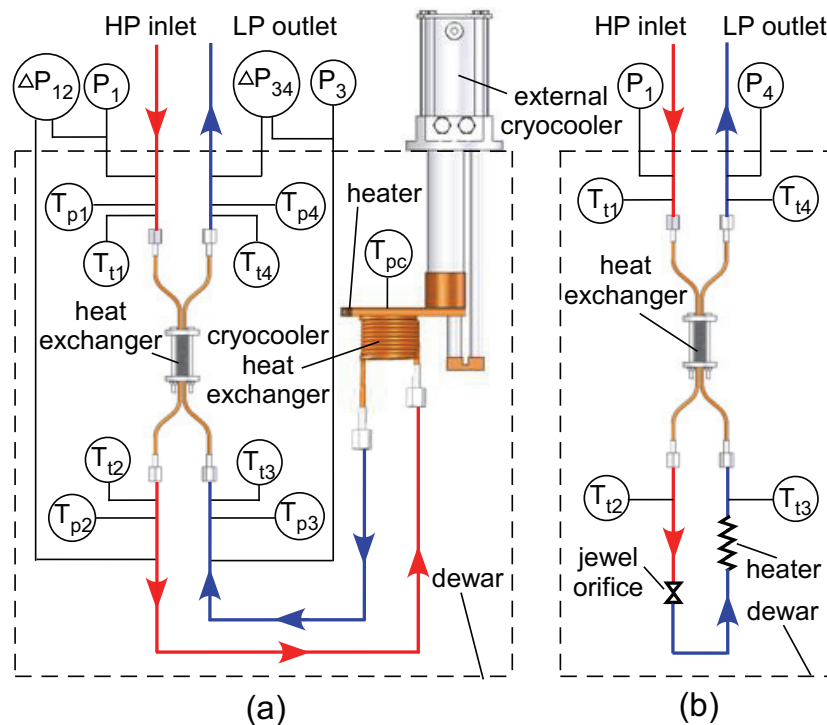


Figure 3.17: Flow schematic of components inside the dewar. (a) Applied cooling mode. Helium gas is used as work fluid. $\Delta P_{12}=P_1-P_2$; $\Delta P_{34}=P_3-P_4$. (b) Self-cooling mode. Ethane is used as the work fluid.

The system is designed for two different operation modes: an applied cooling mode and a self-cooling mode.

1) In the applied cooling mode, shown in Fig. 3.17a, an external cryocooler and a heater are used to acquire large temperature differences across the heat exchanger with minimal pressure differences inside (100-250 kPa) the heat exchanger. Helium is used in this mode. The helium fluid leaving the high-pressure side of the heat exchanger is cooled down to cryogenic temperatures by the external cryocooler before it flows back to the low-pressure side of the heat exchanger. The large temperature differences produced by the external cryocooler enable the effectiveness of the heat exchanger to be accurately measured at low pressures. This minimizes the risk of breaking the heat exchanger at a high gas pressure in the initial testing stage. The effectiveness of the heat exchanger is defined as the ratio of the heat transferred within the heat exchanger to the maximum possible amount of heat that could have been transferred had the heat exchanger been perfect. If we assume that the specific heat is constant across the length of the heat exchanger and there is no internal fluid leakage, the hot and cold side effectiveness ε_h and ε_c can be calculated by equation (3.33) and (3.34):

$$\varepsilon_h = \frac{\dot{q}_{h,net}}{\dot{q}_{max}} = \frac{\dot{C}_h(T_{h,in} - T_{h,out})}{\dot{C}_{min}(T_{h,in} - T_{c,in})} \approx \frac{T_1 - T_2}{T_1 - T_3} \quad (3.33)$$

$$\varepsilon_c = \frac{\dot{q}_{c,net}}{\dot{q}_{max}} = \frac{\dot{C}_c(T_{c,out} - T_{c,in})}{\dot{C}_{min}(T_{h,in} - T_{c,in})} \approx \frac{T_4 - T_3}{T_1 - T_3} \quad (3.34)$$

where $\dot{q}_{h,net}$ is the net heat transfer from the hot fluid; $\dot{q}_{c,net}$ is the net heat transfer to the cold fluid; \dot{q}_{max} is the maximum possible heat transfer in the heat exchanger; $T_{h,out}$ is the hot fluid outlet temperature; $T_{c,out}$ is the cold fluid outlet temperature.

Furthermore, the total uncertainty of the heat exchanger effectiveness on the hot side can be calculated in Eq. (3.35)

$$U_\varepsilon = \sqrt{\left(\frac{\partial \varepsilon_h}{\partial T_{h,in}}\right)^2 (U_{T_{h,in}})^2 + \left(\frac{\partial \varepsilon_h}{\partial T_{h,out}}\right)^2 (U_{T_{h,out}})^2 + \left(\frac{\partial \varepsilon_h}{\partial T_{c,in}}\right)^2 (U_{T_{c,in}})^2} \quad (3.35)$$

where,

$$\frac{\partial \varepsilon_h}{\partial T_{h,in}} = \frac{\dot{C}_h}{\dot{C}_{\min}(T_{h,in} - T_{c,in})} - \frac{\dot{C}_h(T_{h,in} - T_{h,out})}{\dot{C}_{\min}(T_{h,in} - T_{c,in})^2} \quad (3.36)$$

$$\frac{\partial \varepsilon_h}{\partial T_{h,out}} = -\frac{\dot{C}_h}{\dot{C}_{\min}(T_{h,in} - T_{c,in})} \quad (3.37)$$

$$\frac{\partial \varepsilon_h}{\partial T_{c,in}} = \frac{\dot{C}_h(T_{h,in} - T_{h,out})}{\dot{C}_{\min}(T_{h,in} - T_{c,in})^2} \quad (3.38)$$

When the difference between the two fluid inlet temperatures ($T_{h,in} - T_{c,in}$) increases, the partial derivatives on Eq. (3.36)-(3.38) decrease. Therefore, the effectiveness measurements are less sensitive to the uncertainty of temperature measurements at the inlets and outlets, i.e. $U_{T_{h,in}}$, $U_{T_{h,out}}$ and $U_{T_{c,in}}$. Therefore, the effectiveness test at a lower temperature can increase the accuracy of the effectiveness measurements. A similar conclusion can be drawn in the effectiveness measurements on the cold side of the heat exchanger.

2) In the self-cooling mode, shown in Fig.3.17b, a jewel orifice is installed, allowing the work fluid to flow through a very small opening which provides the pressure drop and the J-T effect. The heat exchanger is thus used in a J-T cycle. A heater is also installed in the down-stream of the orifice as a heat load. The inlet pressure is adjusted by the pressure regulator and the external compressor. Gases available in the lab, including N-butane, isobutene, propane, ethane, methane, nitrogen, have been theoretically examined. The major criterion for choosing a single gas is the temperature

drop due to isenthalpic expansion across the orifice or valve. Second, the gas should be able to remain in gas form at high pressure (1-2MPa) in the compressor chamber without condensing at room temperature. Ethane is chosen in this mode in order to provide high cooling power at a relatively low input gas pressure when no condensation occurs in the compressor chamber.

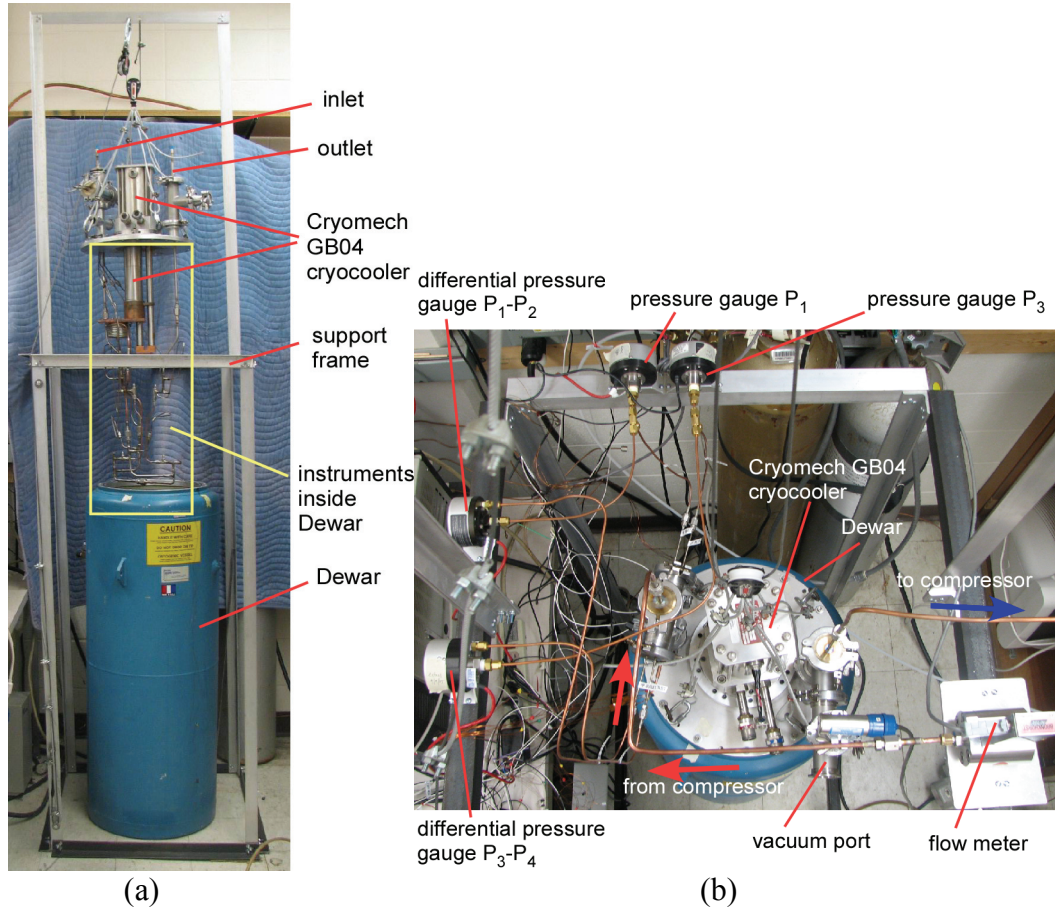


Figure 3.18: (a) Side view and (b) top view of the cryogenic test facility (at UW-Madison).

In both modes, temperatures and pressures at the high-pressure inlet (of the heat exchanger), high-pressure outlet, low-pressure inlet and low-pressure outlet are measured (respectively denoted in Fig. 3.17 by subscripts 1, 2, 3, and 4). Two sets of temperature measurements are recorded simultaneously in the applied cooling mode: A) commercially

available platinum resistance thermometers (PRTs), denoted by T_p ; B) thermocouples, denoted by T_t . The PRTs are calibrated by the manufacturer and their uncertainties are $\pm 0.25\text{K}$. An Agilent 34970A multiplexer with an internal thermistor is used to measure the thermocouple voltages and convert them to temperature readings. Only thermocouples are used in the self-cooling mode due to limited available ports in the multiplexer. The absolute uncertainties of these thermocouples are $\pm 1\text{K}$. The thermocouples are made from the same spool of thermocouple wire. Digital pressure gauges are used to measure the absolute pressure and differential pressures and the gauges have $\pm 0.11\%$ full scale uncertainty.

Figure 3.18 shows (a) the side view of the setup when the dewar is opened and (b) the top view of this cryogenic facility with all pressure gauges and flow meter installed.

Figure 3.19 shows a magnified view of the instrument inside the dewar.

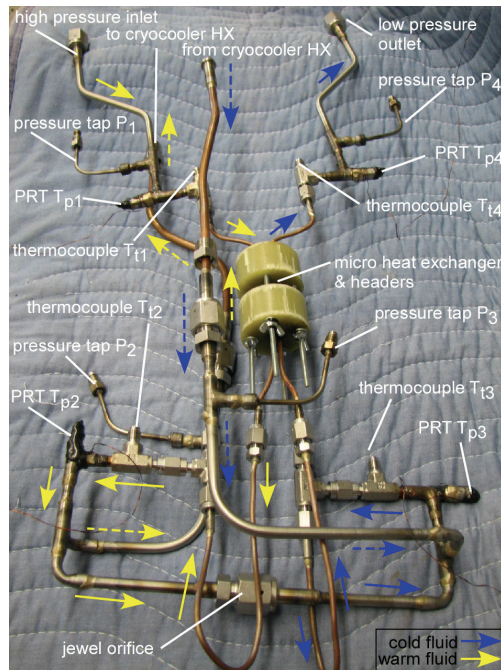


Figure 3.19: Instruments inside the dewar (at UW-Madison).

3.4.2 Major Components and Setups

The compressor used in this test facility is an HC-2D compressor manufactured by APD Cryogenics Inc. It can provide gas pressures up to 2400 kPa. As shown in Fig. 3.20, the compressor is a single stage, water-cooled, oil lubricated rotary compressor that is originally designed to deliver high pressure helium. The oil mixture is absorbed by an absorber before the gas exits the compressor. As a result, the gas is purified before it enters the test facility.



Figure 3.20: HC-2D compressor used in the cryogenic test facility (at UW-Madison).



Figure 3.21: Bronkhorst F-132M mass flow meter (at UW-Madison).

The mass flow rate is measured by a Bronkhorst F-132M mass flow meter, shown in Fig. 3.21, which is calibrated with nitrogen. The mass flow rate reading and its uncertainty are converted to the ones for the corresponding fluid based on formulas recommended by the manufacturer. The meter has an output $V_{signal} = 0-5$ V. The actual mass flow rate \dot{m}_{actual} for a particular gas can be derived from Eq. (3.39).

$$\dot{m}_{actual} = V_{signal} \cdot K \cdot C_{convert} \quad (3.39)$$

where K is the conversion factor from voltage to flow rate (100 standard liters per minute divided by 5 V), $C_{convert}$ is the conversion factor for different gases at different temperatures or pressures, and can be calculated from Eq. (3.40).

$$C_{convert} = \frac{Cp_1 \cdot \rho_1}{Cp_2 \cdot \rho_2} \quad (3.40)$$

where Cp_1 is the specific heat of nitrogen evaluated at 400 bar and 70°C (the calibration temperature plus 50 °C), ρ_1 is the density of nitrogen evaluated at 20°C and 101.325 kPa, Cp_2 is the specific heat of the test fluid evaluated at the inlet pressure and inlet temperature plus 50°C, and ρ_2 is the density of the test fluid evaluated at 20°C and 101.325 kPa. Table 3.3 shows the value of $C_{convert}$ of different gases at different pressures. The percent error associated with the $C_{convert}$ is $(2\%)C_{convert}$ when $C_{convert}$ is larger than 1, $(2\%)/C_{convert}$ when $C_{convert}$ is smaller than 1.

A pressure regulator was installed at the up-stream of the system as shown in Fig. 3.16. The pressure regulator shown in Fig. 3.22 was used in the experiments at gas inlet pressures below 80 psia. An adjustable pressure relief valve is installed to protect the heat exchanger from over-pressured gas. Another pressure regulator (Fig. 2.23) that can regulate higher inlet pressure was used in the experiments at gas inlet pressures above 80

psia.

Table 3.3: Value of $C_{convert}$ of different gases at different pressures [Whi08a]

Gas Type	Pressure			
	1 bar	2 bar	5 bar	10 bar
Helium	1.750	1.750	1.751	1.751
Nitrogen	1.244	1.243	1.239	1.232
Argon	1.746	1.743	1.734	1.720
Methane	0.963	0.961	0.956	0.948
Ethane	0.619	0.616	0.608	0.594
Propane	0.430	0.427	0.417	0.396
Isobutane	0.321	0.318	0.307	0.274
N-butane	0.316	0.312	0.298	0.220

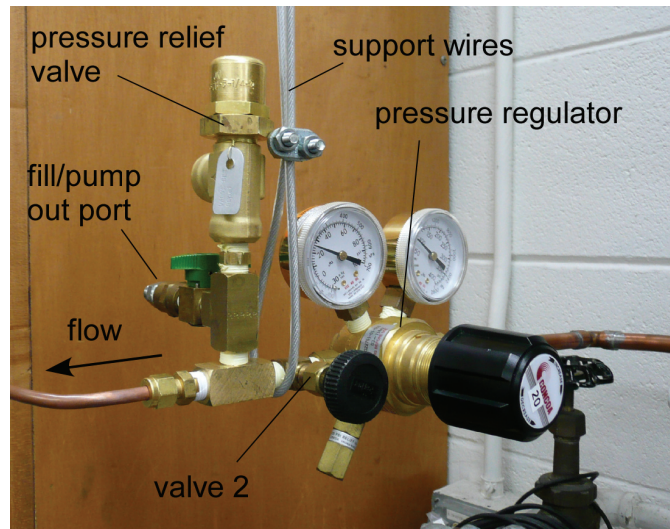


Figure 3.22: Pressure regulator used in the experiments with inlet pressure lower than 80 psia (at UW-Madison).

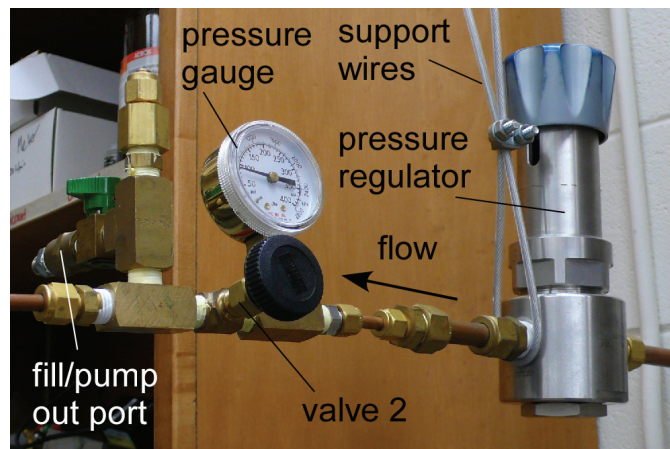


Figure 3.23: Pressure regulator used in the experiments with inlet pressure higher than 80 psia (at UW-Madison).

The heat exchanger, as shown in Fig. 3.24, was mounted to a pair of stainless steel headers and then connected to the test facility by VCR fittings. Four bolts were used to secure the headers and provide enough compressive force to the heat exchanger stack. Generally, this compressive force should be maintained at a level that would not damage the heat exchanger by an unbalance force during the assembly procedure. A layer of STYCAST epoxy was then coated on the surface of the heat exchanger for better thermal insulation. The epoxy on the PRT leads can also protect the solder joints and prevent the PRTs from being shortened during the installation of the heat exchanger. Helium leak tests were performed before and after the installation. High vacuum and Multi-Layer Insulation (MLI) were used to reduce radiation between the assembly and the dewar.

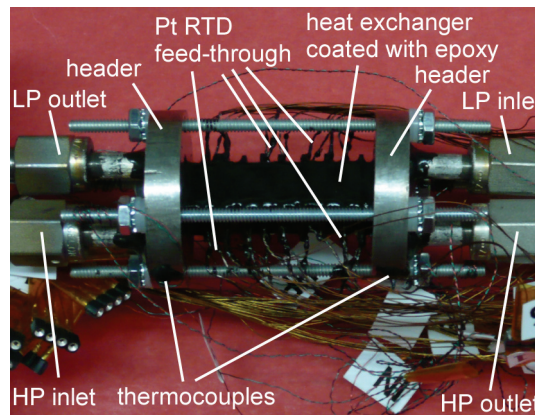


Figure 3.24: A forty-three-die heat exchanger mounted on a pair of headers.

3.4.3 Experimental Setup for Pt RTD Calibration

A simple setup that utilizes the external cryocooler to cool down to cryogenic temperatures is used for calibration of RTDs on single dies. As shown in Fig. 3.25, a copper plate is mounted to the 2nd stage of the external cryocooler. The RTD dies are mounted on the copper plate when a thermocouple is also placed adjacent to those dies. A commercial PRT is also inserted under the copper plate for temperature measurements.

The heater on the copper plate is used as a heat load to control the steady-state temperature of the copper plate. The setup is vacuum insulated inside the dewar during the entire experiment.

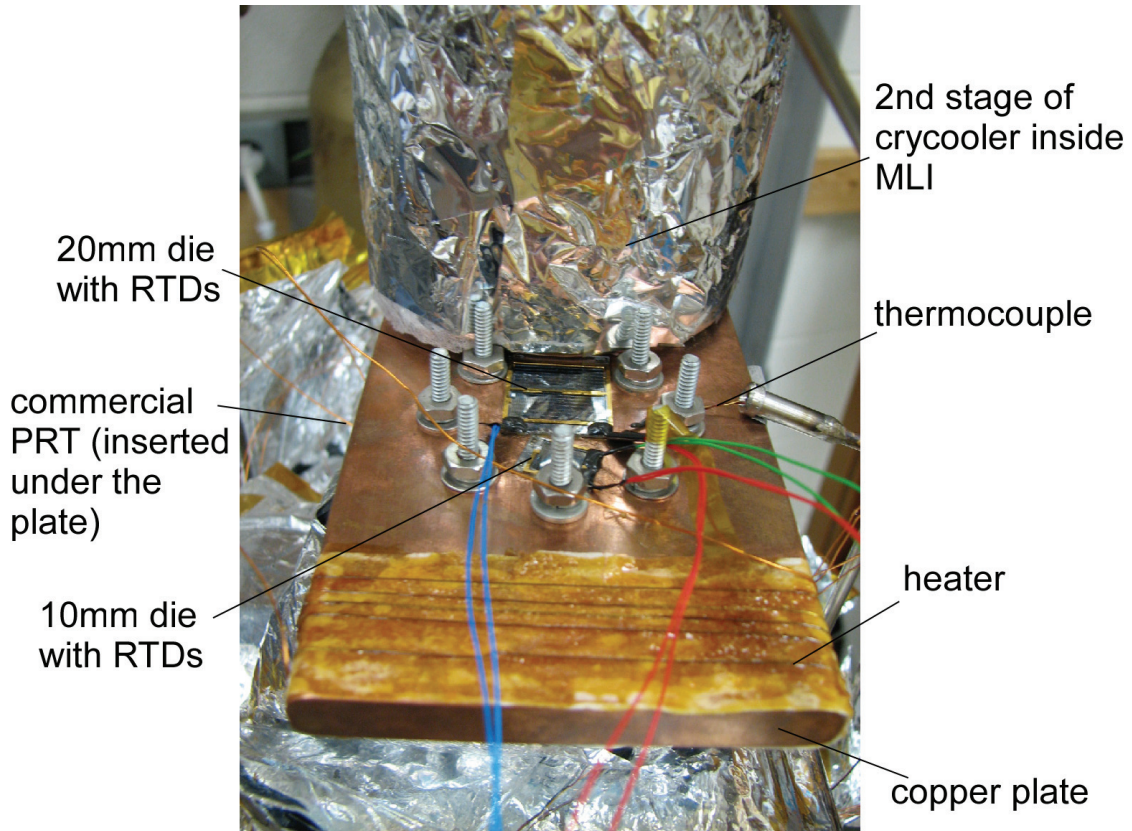


Figure 3.25: Setup for calibration of RTDs on a single die (at UW-Madison).

3.4.4 Improved Self-Cooling Setup

The test setup shown in Fig. 3.19 has a large total thermal mass that slows down the temperature response of the self-cooling test since the cooling power of the micro heat exchanger is limited. As a result, the self-cooling setup was simplified and shown in Fig. 3.26. The original tubing underneath the heat exchanger was replaced by a simple U-shape copper tube to reduce the total thermal mass. A heater was mounted on the U-tube as a heat load.

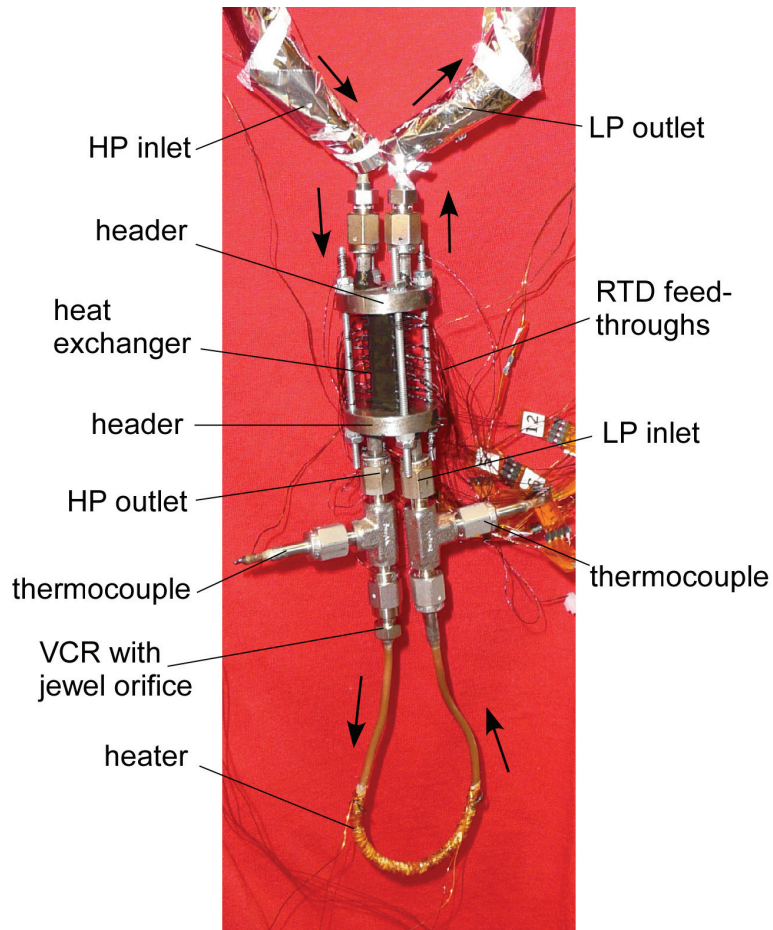


Figure 3.26: Photo of the experimental setup (inside the dewar) for self-cooling test (at UW-Madison).

3.5 Experimental Results

This section presents the experimental results and compares them to the results from the numerical model described in section 3.2. Integrated Pt RTDs are first calibrated in a simple setup on the external cryocooler. Then the effectiveness test with an external cryocooler and self-cooling test with a jewel orifice are completed.

3.5.1 Integrated RTD Calibration

All integrated RTDs in the heat exchanger should be calibrated prior to measurements. For the 10 mm dies, the desired resistance of these RTDs is 1 k Ω .

However, the actual resistance of the fabricated RTDs is in the range of 4-8 k Ω . This is primarily because the photolithography step for patterning these RTD are completed on a silicon substrate with many through-hole slot patterns on it. The reflow of the photoresist in the baking step results in non-uniform thickness of the photoresist layer and consequently non-uniform widths of the Pt metal lines in the photoresist developing step. In some extreme cases, the widths of the lines at certain locations are much smaller than the desired values. As a result, the resistances of these RTDs are inconsistently larger than the design value but remain usable.

Experimental results showed that the temperatures measured by both a commercial PRT and a thermocouple are nearly identical in all temperature ranges. Figure 3.27 shows the measurements of an RTD on a 10 mm die. The resistance remains linear at temperatures above 100 K. The sensitivity of this RTD is 0.26%/K.

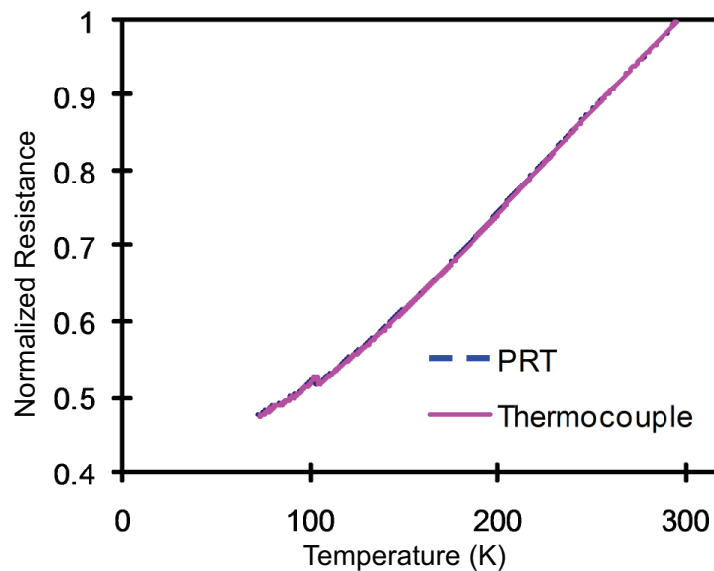


Figure 3.27: Normalized resistance measurement of a Pt RTD on a 10 mm silicon perforated plate as a function of temperature. The temperature is simultaneously measured by a commercial PRT and a thermocouple. The measured resistance at room temperature (296.00 K from PRT, 295.79 K from thermocouple) is 4.287 K Ω . The sensitivity is 0.26%/K. Two measured lines are coincident.

Although this setup is accurate for calibration of RTDs on single dies, it is unfavorable to calibrate multiple PRTs in a long heat exchanger. A test setup modified from the applied cooling mode is constructed to simultaneously calibrate all RTDs on a heat exchanger. The warm helium fluid from the compressor is directed to the external cryocooler with a bypass tube. The cold helium fluid exiting the cryocooler flows through the low-pressure side of the heat exchanger. Since there is no fluid flow through on the high-pressure side of the heat exchanger, only heat conduction in the silicon plates occurs. This results in a uniform temperature across the heat exchanger at steady state. Practically, heat leaks due to heat conduction and radiation from the environment prevents the heat exchanger from being perfectly isothermal. There is about 1.5 K temperature difference between the low-pressure inlet and outlet. For calibration purposes, we simply assume the temperatures inside the heat exchanger are linearly distributed. Accordingly, the temperature at a die could be calculated by Eq. (3.41)

$$T_{die} = T_{lp,out} - \frac{N_{die}}{N_{die,hx}}(T_{lp,out} - T_{lp,in}) \quad (3.41)$$

where $T_{lp,in}$ and $T_{lp,out}$ are the inlet and outlet temperatures on the low-pressure side of the heat exchanger, N_{die} is the number of dies the PRT is from the hot end of the heat exchanger, and $N_{die,hx}$ is the total number of dies in the heat exchanger.

Figure 3.28 shows the RTD calibration on the forty-three die heat exchanger shown in Fig. 3.24. Since the normalized resistance and temperature relationship of Pt RTD is linear, only several temperature points were calibrated. In this experiment, the RTDs are calibrated at 295 K, 270 K, 250 K and 210 K. The sensitivity of the RTDs is in the range of 0.25%/K-0.30%/K.

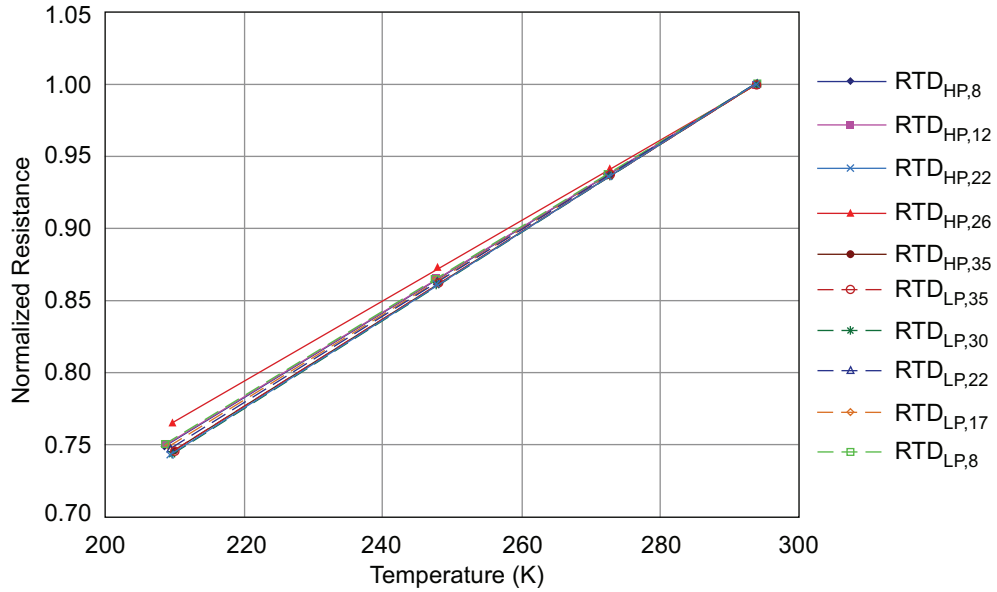


Figure 3.28: Normalized resistances as a function of temperature for the Pt RTDs on the forty-three die 10 mm heat exchanger. The estimated temperature was calculated using Eq. (3.41). The legend shows which side of the heat exchanger the RTD is on, the number of dies the RTD is from the hot end of the heat exchanger.

3.5.2 Effectiveness Test

The forty-three die 10 mm heat exchanger was installed in the test facility and the effectiveness test was completed at a temperature range of 237-252 K. The temperature distribution inside the heat exchanger was also measured. A contamination problem occurred during the test. As the cold end of the heat exchanger reached about 200-220 K, the flow rate started to decrease and an unknown substance solidified and obstructed the flow. When the flow rate decreased, the fluid temperature exiting from the external cryocooler further decreased and the system became unstable. For this reason, the effectiveness test was completed at a temperature range higher than 220 K to avoid this problem. Although this temperature range is not as low as we expected, the temperature gradient across the heat exchanger is still large enough to provide a very accurate measurement of the effectiveness.

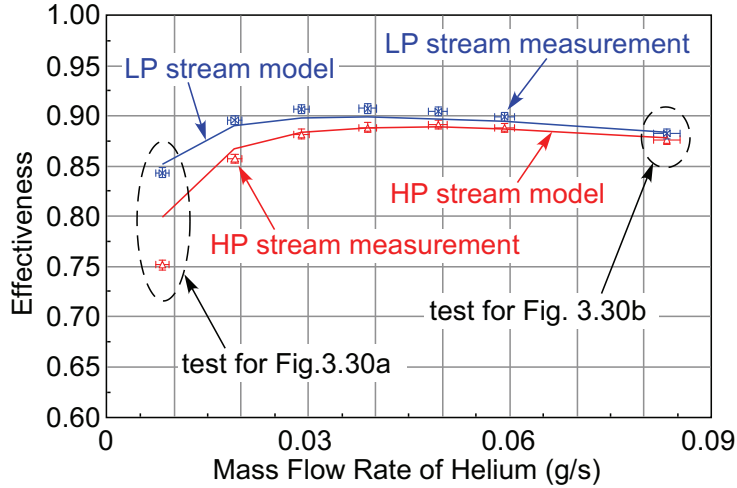
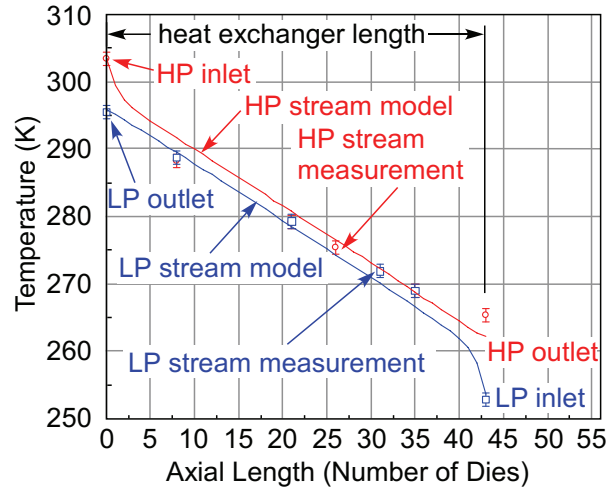


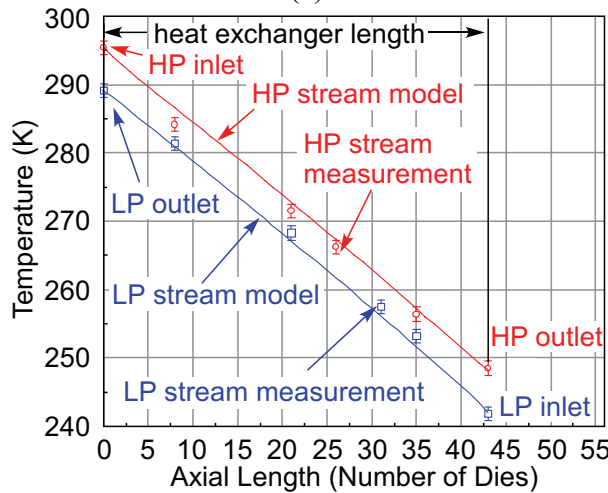
Figure 3.29: Effectiveness measurement at cryogenic temperature range (237-252 K). Two independent sets of data are measured from thermocouples and PRTs. The effectiveness is defined as $(T_1 - T_2)/(T_1 - T_3)$ on high-pressure side and $(T_4 - T_3)/(T_1 - T_3)$ on low-pressure side.

Figure 3.29 shows the measured effectiveness of the heat exchanger as the helium mass flow rate is changed in the applied cooling mode. The hot inlet temperature was maintained at nominally 295-300 K and the cold inlet temperature was maintained at nominally 237-252 K. Hot and cold side effectiveness do not match exactly due to parasitic heat loads on the heat exchanger that cause more heat to be transferred to the low-pressure stream and less heat to be removed from the high-pressure stream. The maximum measured effectiveness of the heat exchanger on the low-pressure stream was 0.912 at a helium mass flow rate of 0.0388 g/s. The parasitic heat loads were nearly constant across all data points in Fig. 3.29 due to the nearly constant inlet conditions. At smaller mass flow rates, the parasitic heat loads are a significant fraction of the total heat transferred between the fluid streams which explains the larger spread between measured effectiveness at lower mass flow rates. The two sets of effectiveness are nearly identical at higher flow rates because the parasitic heat loads are small relative to the heat transferred between the streams at higher flow rates. The numerical model was run for

the same inlet conditions as the experimental data for each steady state condition. The predicted effectiveness is shown by the solid lines in Fig. 3.29. The numerical model is able to accurately predict effectiveness over the range of mass flow rates that were tested.



(a)



(b)

Figure 3.30: The experimentally measured and numerically modeled temperature distributions at a) the lowest and b) the highest mass flow rates in self-cooling test for the forty-three die heat exchanger. Temperature distribution inside the heat exchanger is measured by integrated Pt RTDs.

Figure 3.30 shows the temperature distribution inside the heat exchanger measured by the Pt RTDs in the applied cooing test. Fig. 3.30a shows the temperature distribution at the lowest mass flow rate and Fig. 3.30b shows the temperature distribution at the

highest mass flow rate in the applied cooling test. The inlet and outlet temperatures shown on the plots are measured by the penetration thermocouples and the internal temperatures were measured by the integrated RTDs. The temperature distributions predicted by the numerical model are shown by the solid lines. A similar applied cooling test using ethane was also carried out [Whi08] and the simulation and experimental results are still in good agreement over the range of conditions examined.

3.5.3 Self-cooling Test

The test facility was then changed to the self-cooling mode. Ethane gas was used in this test. Three orifices with different diameter size (0.010 in., 0.015 in. and 0.020 in.) were used. The corresponding opening areas of these three orifices are 0.0507 mm², 0.1140 mm² and 0.2027 mm², respectively. Figure 3.31 shows the measured temperature drop at the orifice as a function of inlet pressure in the self-cooling test without a heat load. Instead of absolute temperatures, temperatures dropped from the high-pressure inlet temperature are used due to fluctuating room temperature. In this test, the low-pressure outlet pressure was maintained at about 10 kPa above the atmosphere pressure. All data recorded in this figure were measured after the entire system reached a steady state. The maximum temperature dropped was 76.1 K from the inlet temperature (actual temperature 218.7K) at 0.269 g/s ethane mass flow rate as the pressure difference between inlet and outlet was 835.8 kPa (121.5 psid). During the test, the heat exchanger could withstand inlet pressure as high as 1 MPa (145 psia) without any internal or external leakage.

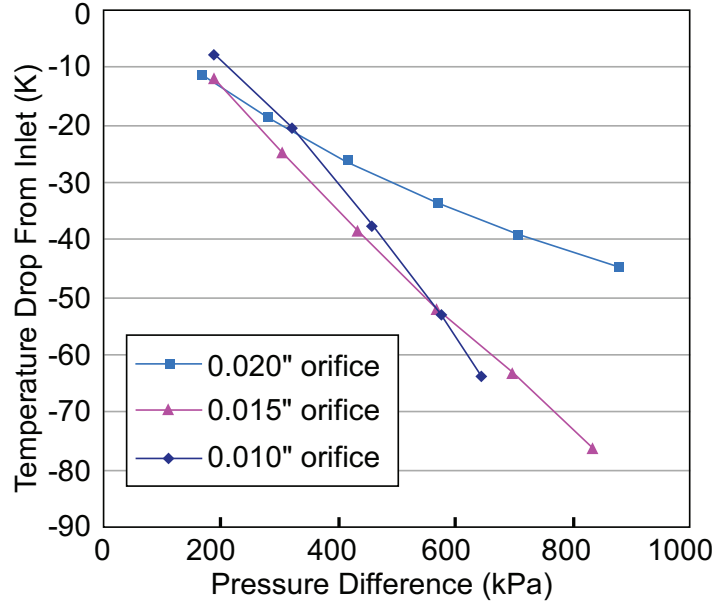


Figure 3.31: Temperature drop at the orifice from inlet temperature as a function of pressure difference between inlet and outlet in the self-cooling test.

Figure 3.32 shows the transient temperature profile as the J-T system installed with a 0.010 in. dia. orifice is cooled down from room temperature. The inlet gas pressure is about 1 MPa. The dynamic response is relatively slow due to the large thermal mass adding to the system through the pipe lines and fittings. Similar to the effectiveness test, during the self-cooling experiment, the system started to clog when the high-pressure outlet temperature reached near 244 K. As the temperature continued to decrease, the mass flow rate of ethane decreased until the flow was completely shut off. The temperature then increased due to parasitic heat load. When the high-pressure outlet temperature increased back to a particular higher temperature, the flow rate started to increase. As a result, the temperature at the low-pressure inlet fluctuated in a temperature range of 230 -240 K. The lowest temperature reached in this transient state was about 200 K. A similar clogging phenomenon was reported by Lerou et al [Ler07a] and

trapped water vapor freezing around the orifice was believed to be the cause of this problem.

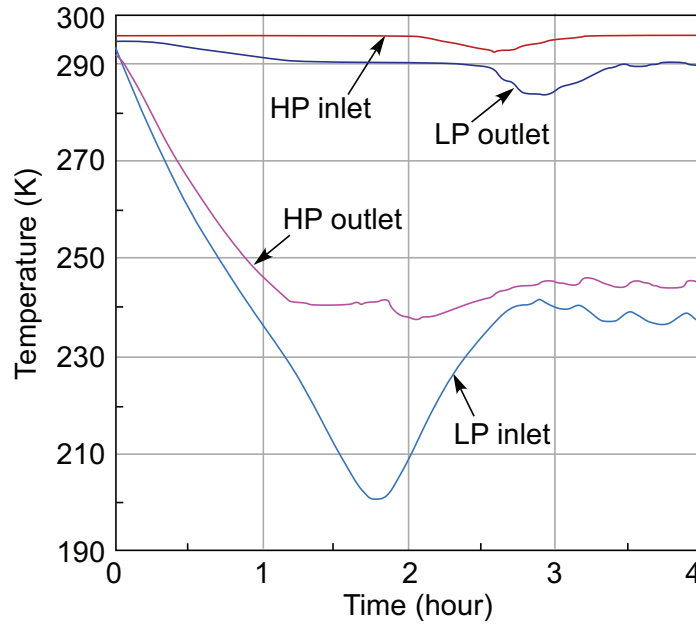


Figure 3.32: Transient temperature profile of the heat exchanger in J-T self-cooling test with 0.010 in. orifice.

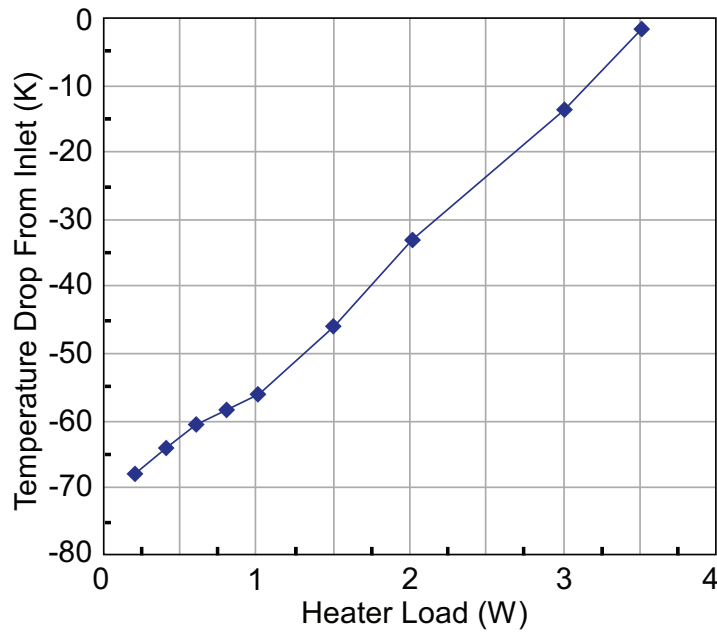


Figure 3.33: Temperature drop at the orifice from inlet temperature as a function of heat load in J-T self-cooling test with 0.015 in. orifice.

There are three significant parasitic heat loads in our tests, including radiation from the vacuum insulated vessel wall, thermal conduction through the headers and the Pt RTDs feed-throughs, and ohmic dissipation from the integrated Pt RTDs. While the radiation can be minimized down to the micro watt range by using MLI as a radiation shield, the thermal conduction and the ohmic dissipation are difficult to eliminate. The total parasitic heat load occurs in the heat exchanger can be estimated based on the enthalpy rise of the fluid in the effectiveness test when the temperatures and pressures are measured on the inlets and outlets of the heat exchanger. The estimated parasitic heat load is about 300-500 mW when the cold end temperature of the heat exchanger is about 210 K.

In order to simulate the actual heat load in practical applications, a load heater was used. Figure 3.33 shows the temperature drop from inlet in J-T self-cooling test with 0.015 in. orifice as the heat load is changed. The system provided 200mW cooling power at 228 K and 1 W at 239 K, when the estimated parasitic heat load was at least 300-500 mW.

3.5.4 Discussion

A multifunctional cryogenic test facility was built for comprehensive experiments of the perforated plate heat exchanger. Although the cryogenic test facility minimizes the heat leaks of the instruments inside the dewar, this comprehensive setup has a large thermal mass. The thermal response in the experiments is therefore slower than that of many other microcoolers. The thermal mass of the heat exchanger is still very small compared to the total thermal mass of the instrument inside the dewar. A much faster

response can be achieved by significantly reducing the total mass of the system. This requires a new design of the test facility. In fact, the heat exchanger and the optimal orifice size or flow restriction can be integrated together in the future. Only one inlet and one outlet port are required to connect this device, and the thermal mass is reduced to minimal.

The heat exchanger demonstrated a high effectiveness of 0.912 in the low-pressure stream in a cryogenic temperature range of 237-252 K and good robustness at high working pressures (up to 1 MPa inlet pressure). The mismatch of effectiveness measurement between the two streams is mainly due to the parasitic heat load on the heat exchanger. Embedded temperature sensors showed consistent sensitivities of 0.26-0.30%/K across a cryogenic temperature range of 205-296 K. Temperature distribution inside the heat exchanger was measured by these sensors. The experimental results validated the numerical model of the heat exchanger which is able to closely predict the performance of the heat exchanger tested over a range of conditions. The lowest temperature in the steady state achieved in the self-cooling tests using ethane as the work fluid was 76.1 K below room temperature (approx. 218.7 K) at 835.8 kPa (121.5 psid) with 0.015 in. dia. (0.1140 mm²) orifice. The system can reach a lower temperature (200 K) in a transient state but started to clog when the high-pressure inlet temperature reached near 244K possibly due to trapped water vapor freezing adjacent to the orifice. The clogging problem is one the drawbacks for using a compressor, because most compressors have oil lubrication systems and the contaminations inside the compressor can potentially clog the heat exchanger or the orifice. Furthermore, in a closed loop system, these trapped impurities will remain in the system and cannot be removed once

the system starts.

The self-cooling test with a heat load shows that the system can provide 200mW cooling power at 228 K and 1 W at 239 K when a 0.015 in. orifice was used. By integrating an orifice or a flow restriction with the heat exchanger and using gas mixture as the work fluid [Lit88, Gon04, Nel05], this perforated plate heat exchanger should be able to provide promising cooling performance suitable for cryosurgery or space applications with portable weight and size.

CHAPTER 4

Flow-Controlled Joule-Thomson Cooling System

This chapter presents a Joule-Thomson cooling system integrated with the perforated plate heat exchanger and a piezoelectrically actuated expansion microvalve [Par08]. The microvalve can control the flow rate at cryogenic temperatures when acting as an expansion valve in the J-T system. Section 4.1 discusses the concept of this J-T system and its potential applications. Section 4.2 summarizes the design, fabrication and experimental results of the micromachined piezoelectric microvalve. Section 4.3 presents the experimental setup of this system, which was modified from the self-cooling mode of the cryogenic test facility. Section 4.4 reports the experimental result of this J-T system and Section 4.5 provides a detailed analysis of the system.

4.1 Concepts

Several cryogenic applications, such as cooling optical detectors in space applications [Col00, Bar02, Gar83] and cryosurgery, demand a cooling system to maintain high stability and a low temperature gradient at cryogenic temperature. Thermodynamic refrigeration cycles are commonly used in these applications due to their high efficiency and refrigeration power. Generally, the cooling temperature at the cold

end is adjusted by a heater. By introducing such an extra heat load, cooling power is wasted and the total energy consumption is increased. This is very critical in space applications where energy consumption should be minimized. Furthermore, when providing enough cooling power, this system should be small and lightweight with a low cost of production and operation to accommodate space applications driven by the cost of the launch and for cryosurgical applications driven by both cost and convenience. Accordingly, the prime objective is to conceive and produce a miniature cryogenic system that can provide sufficient cooling power at cryogenic temperatures and reduce unnecessary energy consumption.

This chapter presents a J-T cryogenic system integrated with a micromachined Si/glass stack recuperative heat exchanger and a piezoelectrically actuated expansion microvalve. This system has the potential to be used in a distributed cooling network for space applications or cryosurgical applications, where no extra heater is needed for temperature control.

A schematic diagram of the J-T cryogenic system in a distributed cooling network is illustrated in Fig. 4.1. In this cycle, cold, high-pressure fluid leaving a recuperative heat exchanger expands through an expansion valve, resulting in a temperature drop if the state of the fluid lies below the inversion curve before expansion. Many similar J-T cooling units can be installed in parallel and refrigerant is distributed to these systems by an external compressor. The expansion microvalve can modulate the flow rate of refrigerant and thus precisely control the local temperature in each cooling unit. This is very cost-effective in space applications that demand multiple cooling units for different locations with different target temperatures because only one compressor system is

necessary and the total size and weight of the systems is tremendously reduced. As an additional benefit, the energy consumption is further reduced by removing the extra heaters. Similarly, a distributed cooling network can be used in cryosurgery, when different cooling temperatures or cooling rates are desired in different locations.

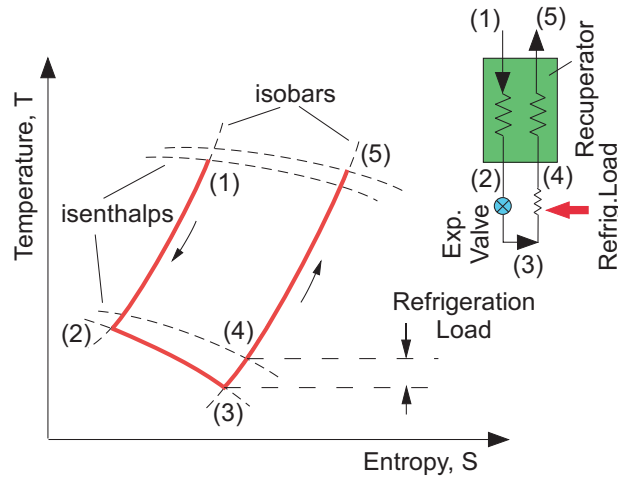


Figure 4.1: Joule-Thomson cooling cycle with an active microvalve for gas expansion.

4.2 Piezoelectric Microvalve³

In order to construct a distributed J-T system, it is essential to have expansion valves that work reliably at cryogenic temperatures and can provide a large flow modulation capability. Furthermore, the active microvalve must have a wide range of operating temperature, and remain functional at cryogenic temperatures during operation, at ambient and even slightly elevated temperature for qualification tests and contamination control processes. Generally, in the J-T cycle, a normally open valve is desirable; the open state is a safe failure mode that does not block refrigerant flow and avoids excessive pressure built up in the system. Finally, it is necessary for the valve to withstand a large pressure difference as the gas expands through the valve and achieves

³ Portions of this effort were reported in abstract form in [Par06,Par07] and journal article form [Park08]

the J–T effect. Several actuation schemes were considered to meet these demands. Several microvalve actuation schemes including electromagnetic actuation [Ter79, Ike97, Shi97, Fu03], electrostatic actuation [Dub01, Col04, Van98, Huf93] and thermal actuation, such as thermopneumatic [Zde87, Ric03], bimetallic [Bar94, Bar94a, Mes98] and shape memory alloy [Koh00], were reported. However, all these schemes have their individual weaknesses, such as high power consumption, small actuating force and low-temperature degradation of performance, that limit their use in the high-pressure, low-temperature flow modulation and the J-T gas expansion. Piezoelectric actuation was chosen in our valve designed because it allows proportional flow control and is capable of generating high force with low power consumption. Figure 4.2 illustrates this piezoelectric actuated microvalve designed by Park et al. [Par08]. The valve operates by pushing a bulk Si micromachined plate against a Corning #7740 Pyrex glass substrate that has the inlet and outlet holes in it. A commercially available multilayered PZT stack is used to drive the silicon valve plate (Physik Instrumente, Germany, PL055). The PZT stack has a footprint of $5 \times 5 \text{ mm}^2$ and a height of 6 mm.

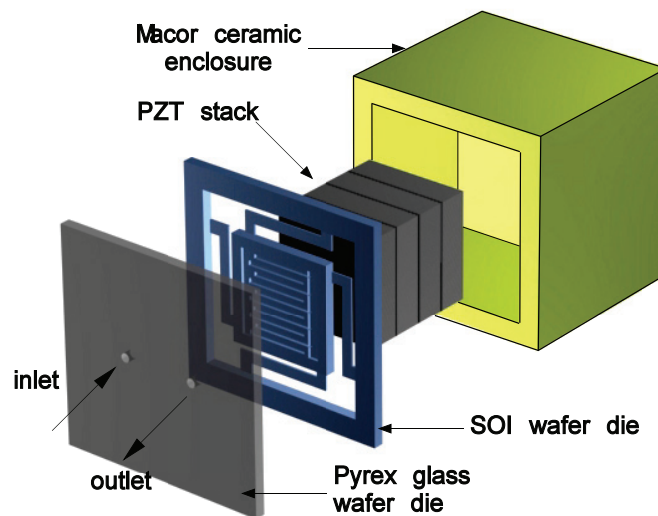
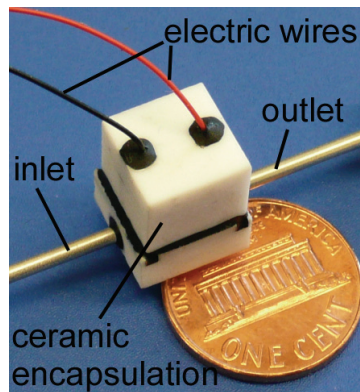
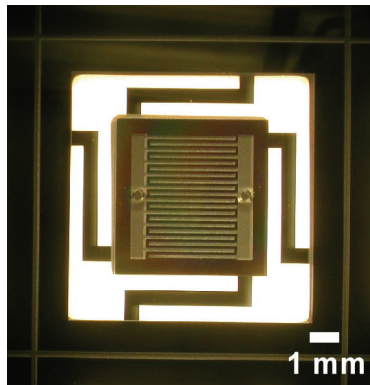


Figure 4.2: Piezoelectric microvalve design [Par08].

The detailed fabrication and assembly processes of this valve are also reported in [Par08]. MacorTM, a machinable glass mica ceramic that has zero porosity, is used for packaging the valve in order to minimize the temperature expansion mismatches between materials and thus avoid inhibition of valve operation. The ceramic enclosure measures $1 \times 1 \times 1 \text{ cm}^3$, and has a 6 mm deep cavity with 1 mm thick walls on all four sides. Figure 4.3 shows this fabricated microvalve.



(a) Microvalve packaged with ceramic housing



(b) Valve seat (glass die on the top and SOI wafer die on the bottom)

Figure 4.3: Photos of (a) the piezoelectric microvalve and (b) valve seat structure. The overall size of the piezoelectric microvalve is $1 \times 1 \times 1 \text{ cm}^3$.

4.3 Experimental Setup

The valve was tested with helium as the work fluid. Since the flow control behavior of ethane is unknown, it was necessary to individually test the valve with ethane.

A simple setup, shown in Fig 4.4 was built for this purpose. The ethane mass flow rate and the pressures at the inlet and outlet of the valve were measured. Input voltage of -30 V to 100 V was applied to the microvalve in order to adjust the flow rate and pressure drop across the valve. The mass flow rate and pressure difference relationship was recorded at room temperature. The experimental results were compared to the commercial available jewel orifice and will be discussed in the next section.

The J-T system experiment setup was modified from the self-cooling mode of the cryogenic system described in section 3.5.3. Figure 4.5 illustrates (a) the schematic of this system inside the dewar and (b) the photo of the finals setup.

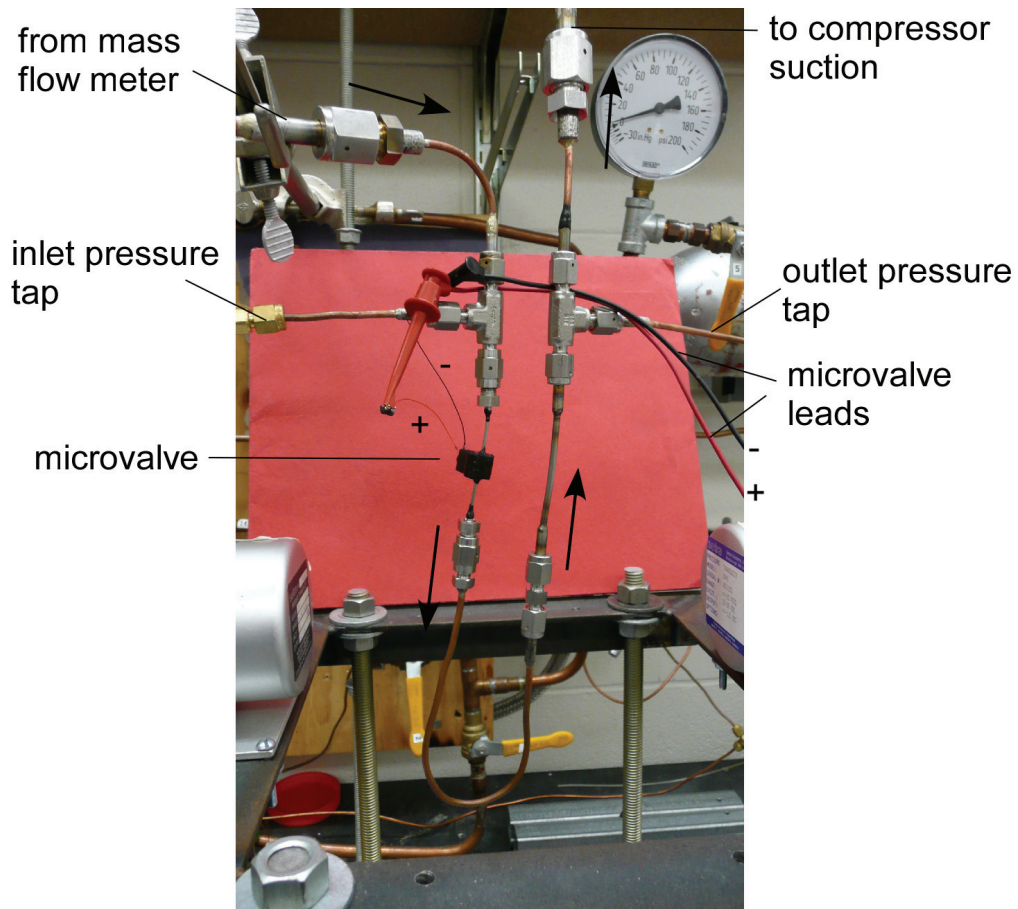


Figure 4.4: Photo of the flow modulation test for microvalve (at UW-Madison).

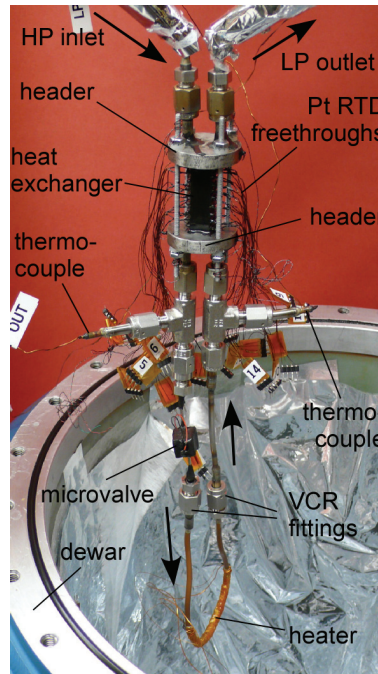
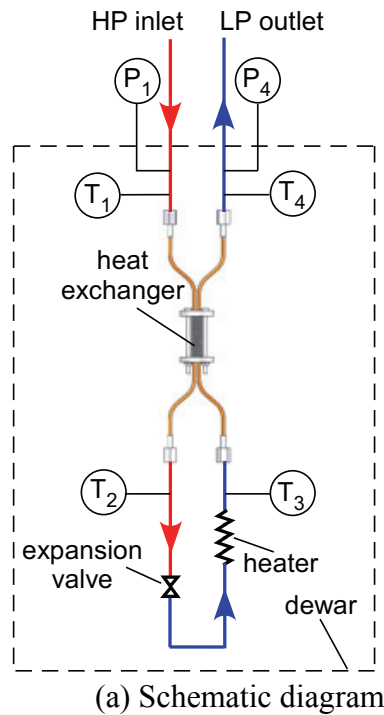


Figure 4.5: Schematic diagram and photo of test setup for the flow-controlled J-T cryogenic system inside the dewar.

The heat exchanger mounted on a pair of headers and the microvalve are connected to the J-T system with VCR fittings. A heater is also attached to the copper tube between the microvalve and the low-pressure side of the heat exchanger. In our experiment, this heat is not used for temperature control, but for simulating a heat load from the cooled object. The flow scheme for this system is identical to the flow scheme shown in Fig. 3.16. The external compressor is used to provide a high-pressure input gas from the low-pressure returning stream, and therefore achieve a closed loop J-T cycle. Ethane is used in our test because it can provide large cooling power, i.e. larger J-T coefficient at the operating pressure (0-1 MPa)

Similar to the experimental setup described in the previous chapter, temperatures and pressures at the HP inlet (of the heat exchanger), HP outlet, LP inlet and LP outlet are measured (respectively denoted in Fig. 4.5a by subscripts 1, 2, 3, and 4). Type E

thermocouples are used for temperature measurements. An Agilent 34970A multiplexer with an internal thermistor was used to measure the thermocouple voltages and convert them to temperature readings. The absolute uncertainties of these thermocouples are $\pm 1\text{K}$. The thermocouples are made from the same spool of thermocouple wire. Before the work fluid flows into the HP inlet of the heat exchanger, the mass flow rate of this fluid is measured at room temperature by a Bronkhorst F-132M mass flow meter. Digital pressure gauges are used to measure the absolute pressure and differential pressures and the gauges have $\pm 0.11\%$ full scale uncertainty.

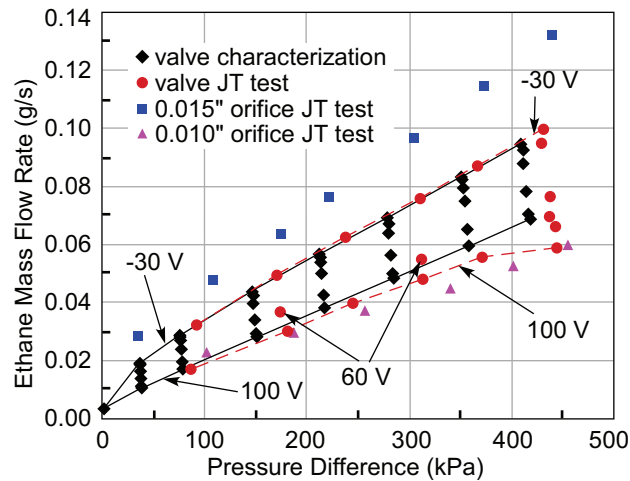


Figure 4.6: Ethane mass flow rate as a function of pressure difference in valve characterization test and J-T tests. -30 V, 0 V, 30 V 60 V, 80 V and 100 V were used as input voltage. The mass flow rate is measured at room temperature in all tests.

4.4 Experimental Results

The pressure drop results of the microvalves at room temperature and in the J-T system are shown in Fig.4.6. The input voltage range of the valve is from -30 V to 100 V. The mass flow rate and pressure difference relationship of commercially available jewel orifices are also included in this plot. This data is obtained from the J-T self-cooling test of the heat exchanger. As shown in the plot, the range of opening of the microvalve is

equivalent to 0.010-0.013 inch diameter jewel orifices. At 100 V and the same pressure difference, the mass flow rate in the J-T test is smaller than in the characterization test because a heat exchanger is added into the system and causes an additional pressure drop. Thus, the actual pressure difference across the microvalve in the J-T test is smaller. However, when the input voltage is -30 V and thus the flow rate is higher, the effect is negligible and the relationships in both tests are almost identical. In addition, the flow rate that the microvalve can modulate is less than 0.02 g/s at the measured pressure range. With a fixed actuating distance of the PZT stack in the given input voltage range, a larger valve seat that allows more flow to pass through is desired.

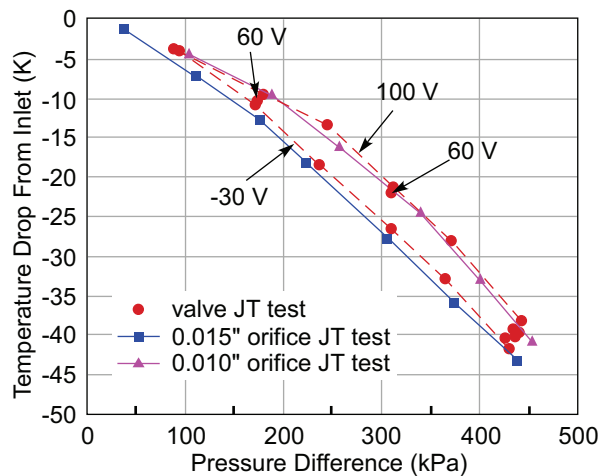


Figure 4.7: Temperature drop at the valve or orifice from inlet temperature as a function of pressure difference between inlet and outlet in the J-T test. Since the input voltage of the microvalve is -30 V to 100 V, the region between two dash lines is the temperature region that the J-T system can control at a given input pressure.

Figure 4.7 shows the temperature drop from the inlet as a function of inlet gas pressure in the J-T test. Data was recorded when the system reached a steady state. At a certain inlet gas pressure, the temperature can be adjusted by the flow modulation of the microvalve. However, the extent to which the temperature range can be modulated is

limited to not more than 5-8 degrees because of the small flow modulation of the microvalve. The lowest steady-state temperature the system can achieve at the cold end of the valve in our test is about 254.5 K at 430 kPa pressure difference between the HP inlet and the LP outlet as the input voltage is -30 V. In fact, the system is able to reach lower temperatures at higher inlet gas pressure. So far, the system has proved to be able to sustain as high as 1 MPa inlet gas pressure without leakage.

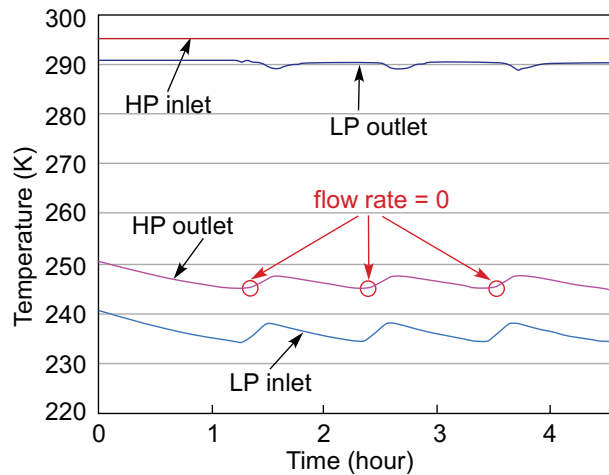


Figure 4.8: Transient response of the J-T cycle when it is cooling down. The gas flow is shut off as the temperature reaches around 244 K at the HP outlet, which is very close to the microvalve. This is mainly due to the impurities freezing around the microvalve.

Similar to the J-T self-cooling test discussed in the previous chapter, due to impurities freezing inside the system, the flow could be shut off when the HP outlet temperature around the valve reaches 244 K. Figure 4.8 shows the transient response of this J-T system at pressure difference 710 kPa and illustrates the clogging problem. As the HP inlet temperature reaches 244 K, the flow rate is shut off and the temperature increases due to parasitic heat lost. Finally, when the system warms up to 246 K and the impurities melt, the flow can pass through the valve and the temperature of the system decreases again. The system thus reaches a repeat cooling cycle and the LP inlet

temperature fluctuates between 234 K and 236.5 K. As shown in Fig. 4.8, the cooling rate of this J-T system is very slow mainly because the thermal mass of the entire system including the metal components such as tubing and VCR fittings is too large. For these reasons, the heat exchanger and the microvalve should be integrated together in the future to eliminate all unnecessary tubing and fittings and consequently reduce the thermal mass to a much lower level. Ideally, the system should be able to reach a desired temperature within tens of minutes.

4.5 Discussion

The experiments have demonstrated a closed loop J-T cryogenic system using a micromachined perforated plate Si/glass heat exchanger and a piezoelectric expansion microvalve for modulating the work flow thereby cooling temperature. The heat exchanger and microvalve have been successfully fabricated. The system is robust enough to sustain inlet pressures as high as 1 MPa without either internal or external leakage. The microvalve has an input voltage from -30 V to 100 V for minimum to maximum opening. It was characterized and the opening is equivalent to a commercially available jewel orifice with diameter ranging from 0.010 in. to approximately 0.013 in. A high vacuum insulated test facility was built for testing the J-T system at low temperature when parasitic heat lost is minimized. Experiments showed that the system could achieve 254.5 K at 430 kPa pressure difference at steady state and 234 K at 710 kPa in a transient state. Due to impurities freezing around the valve, the system was clogged as the HP outlet pressure reached near 244 K. The system should be further integrated in order to reduce the thermal mass and increase the cool down rate. A cold trap can be added to

remove the impurities inside the system and a much low temperature could be achieved. The system successfully demonstrated a J-T system with a microvalve modulating refrigerant flow and thus the cooling temperature of the cold end and the temperature remained very stable. In the future, after further integration, the system could be used in a distributed cooling network that provides promising cooling power when the temperature could be precisely controlled by the piezoelectric microvalve.

CHAPTER 5

Conclusion and Future Work

This chapter summarizes the results presented in previous chapters and outlines the future work of this research.

4.1 Conclusion

This research effort has resulted in the successful design, model, fabrication and tests of two generations of heat exchangers used in micromachined J-T coolers. The primary goal of this work has been to develop a micromachined heat exchanger with high effectiveness (>0.90) and robustness (>1 MPa gas pressure), which is suitable for cryogenic applications that demand high cooling power (in watt range) at a moderate cryogenic temperature range (200-225 K). Another goal was to integrate the temperature sensors along the length of the heat exchanger to elucidate the performance and specifications of the heat exchanger. Many of these goals have been achieved by the perforated plate Si/glass heat exchanger.

First, the micromachined perforated plate Si/glass heat exchanger integrated with Pt RTDs was successfully designed and fabricated in a lithography-compatible micromachining process. The fabricated heat exchanger has a footprint of 1×1 cm², and

length of up to 3.5 cm. Based on the initial lessons learned from the design, fabrication and experiments of our planar heat exchanger, several fabrication processes, including KOH through-wafer etching on (110) silicon wafers, HF:HNO₃ through-wafer glass etching and die level Si/glass stack bonding, were explored to ensure low cost and high yield in each major process step.

Second, the perforated plate heat exchangers were successfully tested in a multifunctional cryogenic test facility in two different modes. The heat exchanger demonstrated high effectiveness 0.912 in the low-pressure stream in a cryogenic temperature range of 237-252 K in the applied cooling mode and good robustness at high working pressures (up to 1 MPa inlet pressure) in the preliminary pressure test and the self-cooling mode. The mismatch of effectiveness measurement between the two streams is mainly due to the parasitic heat load on the heat exchanger. Temperature distribution inside the heat exchanger is measured by embedded temperature sensors that have consistent sensitivity 0.26-0.30%/K across cryogenic temperature range of 205-296 K. In the self-cooling test with ethane as the work fluid, the lowest steady-state temperature that the J-T system achieved was 76.1 K below room temperature (approx. 218.7 K) at 835.8 kPa (121.5 psid) when using a 0.015 in. dia. (0.1140 mm²) orifice. Self-cooling tests with a heat load showed that the system can provide 200mW cooling power at 228 K and 1 W at 239 K. Also, the system reached even a lower temperature (200 K) in a transient state, but could not maintain that temperature due to impurities that clogged the system.

Third, the numerical model of the perforated plate heat exchanger was validated by the experimental results obtained from the cryogenic test. The model was able to closely

predict the performance of the heat exchanger tested over a range of conditions. It can serve as a useful tool for designing perforated plate micro heat exchangers in the future.

Fourth, a closed loop J-T cryogenic system using a micromachined perforated plate Si/glass heat exchanger and a piezoelectric expansion microvalve was demonstrated. The fluid flow was modulated by the microvalve, thereby adjusting the cooling temperature in the J-T cycle. The normally open microvalve has an input voltage from -30 V to 100 V for minimum to maximum opening. It was characterized and the opening is equivalent to a commercially available jewel orifice with diameter ranging from 0.010 in. to approximately 0.013 in. Experiments showed that the system could achieve 254.5 K at 430 kPa pressure difference at steady state and 234 K at 710 kPa in a transient state. This system successfully demonstrated that the cooling temperatures at the cold end were modulated by the microvalve and remained very stable as the input voltage remained unchanged. In the future, the system could be used in a distributed cooling network that provides promising cooling power when the temperature can be precisely controlled by the piezoelectric microvalve.

Finally, a creative design and a fabrication process for the Si/glass planar heat exchanger were developed. It has a size of $60 \times 15 \times 2.5 \text{ mm}^3$. This silicon and glass hybrid design fully utilizes the thermal properties of these two materials. While the high conductivity silicon fin structure can transfer heat very effectively between the heat exchanger and fluid, the low conductivity glass base plate serves as a very good intermediate layer for heat transfer between streams. Several fabrication processes were optimized and some new processes and equipment were developed. A two-step DRIE process was designed to etch the silicon fin structure and diminish the effects from non-

uniformity, footing effect and micro-loading effect of DRIE. Several wafer bonding techniques including wafer-level Si/glass/Si anodic bonding, die-level and wafer-level glass frit bonding using commercially available glass frit tape were investigated. A low-cost ECDM machine was constructed to precisely drill inlet and outlet holes on the glass substrate.

While many goals were achieved in this research work, several difficult lessons were learned as well. First, the robustness of the planar heat exchanger is not high enough to provide enough cooling power in a J-T cycle due to the fragility of the unsupported thin glass base plate. Originally the glass base plate was designed to be supported by the silicon fin structures when the fins are closely attached to the glass caps. However, the large tolerance of the HF wet etching process on the glass caps resulted in leaving the fin structures detached from the glass cap and caused a large deflection on the base plate when pressure difference between two streams was high. It was determined that the present construction of the planar heat exchanger is limited in its capability to handle pressure difference greater than 70 kPa. It was also noted that the use of sapphire as a replacement for the glass base plate can improve the thickness of the base plate and consequently the robustness of the heat exchanger.

Additionally, during the self-cooling test in the cryogenic test facility, the J-T system was clogged when the high-pressure inlet temperature reached 244 K possibly due to trapped water vapor freezing around the orifice. This is a fundamental problem for a miniature closed loop J-T system when an external compressor is used. Impurities trapped inside the compressor are very difficult to remove. Finally, the internal instrument of the cryogenic test facility had a large total thermal mass and slowed down

the response of our experiments. A more compact test setup should be developed to achieve the rapid cooling of our micromachined heat exchanger.

In conclusion, this research effort has resulted in a successful development of compact micromachined Si/glass heat exchangers with good robustness and high effectiveness. In a J-T system, this heat exchanger can achieve a high heat transfer per volume and consequently provide a large cooling power with a relatively low input gas pressure (1 MPa). This is particularly suitable for a fully micromachined closed loop J-T cooler that demands low input gas pressure due to the limited gas pressure available by micromachined compressors. By replacing the traditional cryocooler to a fully micromachined cryocooler that can provide a comparable cooling capacity when the size and weight are significantly reduced, many of these potential applications including cryosurgery, cooling infrared detectors for space applications and night vision devices will significantly benefit from this research and proceed to a new era.

4.2 Future Work

There are several improvements to be addressed in design, fabrication and testing of the heat exchanger and its J-T system.

Although the perforated plate heat exchanger was successfully fabricated and the yield of Si/glass die is high, the final stack bonding process still requires further improvement. Si-Au eutectic bonding can simultaneously assemble the stack and the strength of the bond has proved to be strong and leak tight in many other MEMS packaging applications. The effect of the thermal mismatch of the gold layer at cryogenic temperature is unknown. Further characterization at cryogenic temperature of

this bonding technique is necessary.

As mentioned in Chapter 3, the deposition of Pt RTDs was not consistent because it is very difficult to pattern the RTD on a substrate that has many through-wafer slots after a KOH process. A feasible solution is to pattern the Pt RTDs before the KOH process. However, extra caution should be taken to protect metal patterns during the KOH process. Further investigation on these processes should be completed.

The next major step for this research work should be integration of the J-T microcooler. Heat exchanger, flow restriction or microvalve, temperature, pressure and flow sensors can be integrated into a single microcooler design. The total thermal mass of the system would therefore be significantly reduced. The cooling rate of the device would dramatically increase and meet the requirements of target applications. In the future, mixed gas will be used in the J-T system. In fact, according to the previous research [Kep04, Nel05] and the preliminary results from Hoch's model, the J-T system integrated with a 10 mm perforated plate heat exchanger may be able to provide approximately 5-10 W in a temperature range of 150-200 K when using mixed gas at 2 MPa.

The occurrence of impurity clogging was problematic in our J-T self-cooling tests. This issue needs to be further investigated. A cold trap in the experimental setup can eliminate this problem, but is not an ultimate solution since the cold trap cannot be easily integrated into a microcooler. Consequently, steps to clean up and vacuum the system before experiments are very critical. A more effective way to remove the water vapor and other impurities is also necessary.

Toward the application goals, the micromachined J-T system should be developed

as an instrument for particular applications such as a portable cryosurgical probe or a cooling unit that can be mounted on night vision devices. A packaging technique with superb thermal insulation will be critical for this device to be able to provide enough cooling power in a practical environment when the parasitic heat leak is minimized.

This thesis has demonstrated that high-efficiency micro heat exchanger for high cooling capacity can be designed and fabricated with high-precision lithographical processes. The embedded sensors and flow modulation with micromachined valve demonstrated capability to facilitate a servo-controlled operation in the J-T system in the future.

APPENDIX A

Design, Fabrication and Tests of a 20 mm Perforated Plate Heat Exchanger

In the design stage of the perforated plate heat exchanger, a heat exchanger with $20 \times 20 \text{ mm}^2$ cross section was also designed. However, due to fabrication limits, this large heat exchanger had significant internal leakages and therefore, did not provide acceptable results in our experiments. This section describes some details about the design, fabrication and experimental results of this heat exchanger.

Table A.1: Summary of geometric parameters of 20 mm perforated plate heat exchanger

Si plate			Glass spacer		
Description	Variables	Dimension	Description	Variables	Dimension
Width of die	W_{die}	19770 μm	Width of die	W_{die}	19770 μm
Height of die	H_{die}	19770 μm	Height of die	H_{die}	19770 μm
Width between stream on Si die	$W_{\text{si,stream}}$	1700 μm	Width between stream on glass die	$W_{\text{g,stream}}$	700 μm
Width of Si slot	W_{duct}	1000 μm	Width of glass window	W_{gw}	8600 μm
Height of Si slot	H_{duct}	50 μm	Height of glass window	H_{gw}	17850 μm
Width of Si web	W_{web}	10 μm	Thickness of glass spacer	t_{sp}	300 μm
Width of each Si fin row	W_{fin}	7600 μm			
Height of each Si fin row	H_{fin}	50 μm			
Thickness of Si die	t_{fin}	500 μm			
Number of slot column	N_{column}	7			
Number of slot row	N_{row}	169			

A.1 Design

The structure of the 20 mm perforated plate heat exchanger is very similar to its 10 mm counterpart. The die geometric parameters are listed in Table A.1. Pt RTDs are also

integrated into the 20 mm heat exchanger. Figure A.1 shows the layout design of these RTDs. Similarly, normal RTDs are used for measurement of average temperature in the fluid streams and reference RTDs outside the heat exchanger are included on each side.

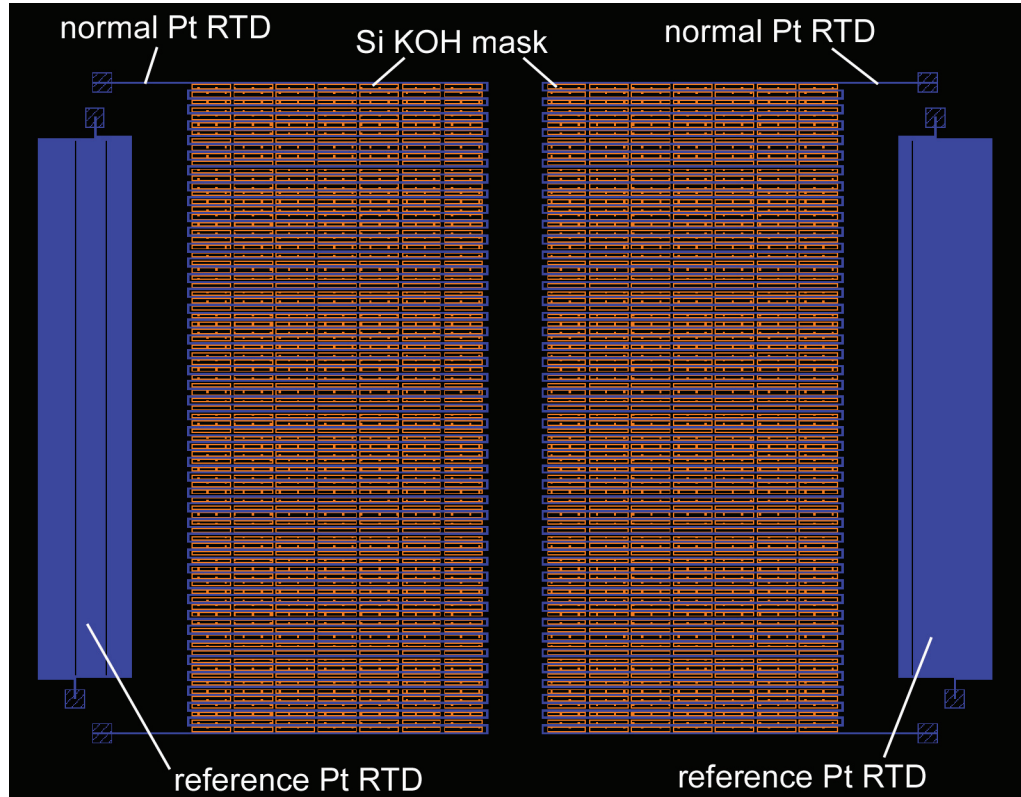


Figure A.1: Mask layouts of silicon KOH and Pt RTDs in 20 mm perforated plate heat exchanger.

A.2 Fabrication

The fabrication of the 20 mm heat exchanger is identical to the 10 mm version. These two patterns are included in the same mask layout and fabricated together. The detailed fabrication process was discussed in section 3.3. Similar to the RTDs on 10 mm heat exchanger, the actual resistances of these RTDs are almost five times larger than the design value due to the issues in photolithography. In the stage of heat exchanger assembly, both epoxy and Si-Au eutectic bonding were attempted. However, the bond

quality and bond strength are not sufficient for the 20 mm heat exchanger because of its larger footprint and bonding area. This is partially due to the force applied to the heat exchanger stack are not uniform such that the Si-Au eutectic bonding interfaces in many locations along the bonding strip are weak. As a result, the 20 mm heat exchanger only fabricated with epoxy, as shown in Fig. A.2.

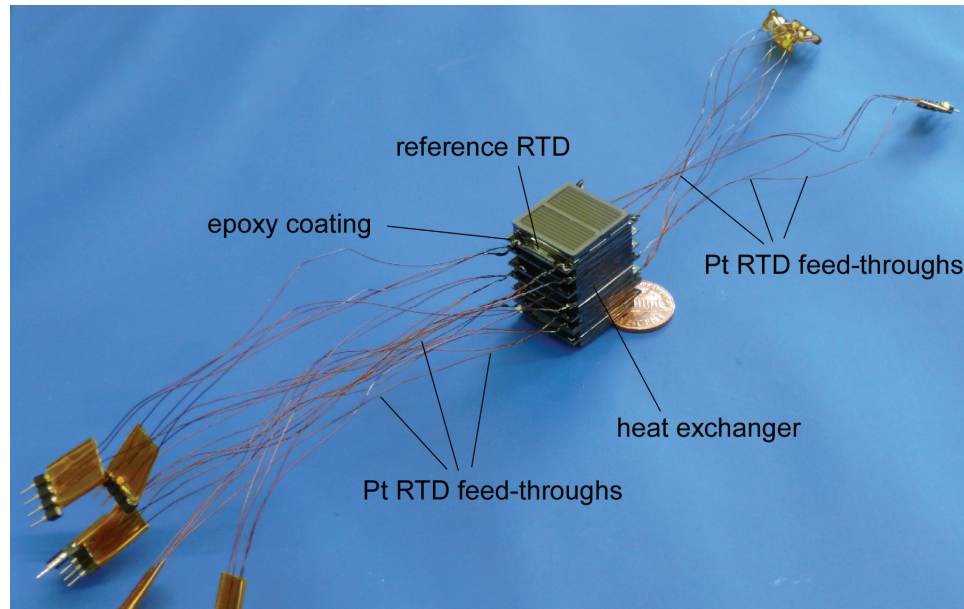


Figure A.2: Photograph of 20 mm heat exchanger with 37 dies epoxy together. Feed-through wires are soldered to the RTDs for four point measurement.

APPENDIX B

Misalignments and Defects in the KOH Process on a (110) Silicon Wafer

The mechanism and fabrication process of the KOH on (110) silicon wafers were discussed in Section 3.3.2.1. In the initial stage of fabrication, the effect of misalignments between the pattern and the actual silicon (111) crystal plane was unknown. This section discusses the misalignment issue in our fabrication process and the results.

B.1 Type of Misalignment

There are two major types of misalignment between patterns and the silicon crystal plane discussed as follow.

B.1.1 Manufacture Tolerance of Crystal Orientation

The tolerance of crystal orientation is $\pm 1^\circ$ in all directions. This factor alone is not a major problem since the hole will only offset about $500 \mu\text{m}$ (thickness of Si wafer) $\times \sin 1^\circ \approx 8.7 \mu\text{m}$ at the bottom surface. In this case, the sidewalls, which are vertical to Si surface in the ideal case, will also have 1° error in a random direction.

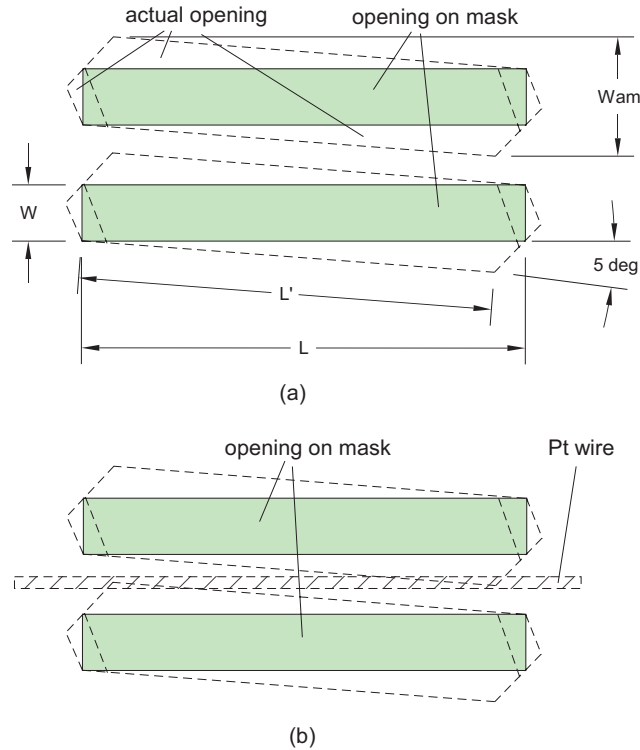


Figure B.1: Misalignment with 5°. (a) without Pt wire; (b) with Pt wire.

B.1.2 Misalignment between Mask and Wafer Flats

The primary flat and secondary flat on the (110) wafer are used as references for alignment. Both of them are $\langle 111 \rangle$ direction and have an ideal angle 70.53° with each other. The alignment is manually done in an aligner, thus results in an error approximately up to 5° (combined with the manufacture tolerance mentioned above). Figure B.1a shows the actual opening with 5° misalignment. The actual width with misalignment $W_{am} = W + 2L \times \sin 5^\circ$ (assuming $L \gg W$, $L \approx L'$). When L is large, W_{am} could be several times larger than W . This is safe as long as the distance between openings on the mask is larger than $L \times \sin 5^\circ$. Otherwise, the actual opening will reach the opening next to it. However, if Pt RTDs (Pt wires) are added between slots, some opening areas will overlap Pt wire as shown in Fig. B.1b. This implies that Pt metal layer will not be

deposited in those overlap areas and thus will be disconnected. The length of the slot opening, L , plays an important role in this misalignment. A smaller L will reduce the effect of this misalignment. As a result, a long slot opening is divided into two or more shorter openings in our design. However, this will reduce the total open area of the silicon perforated plate, thus affect heat transfer and pressure drop in the heat exchanger.

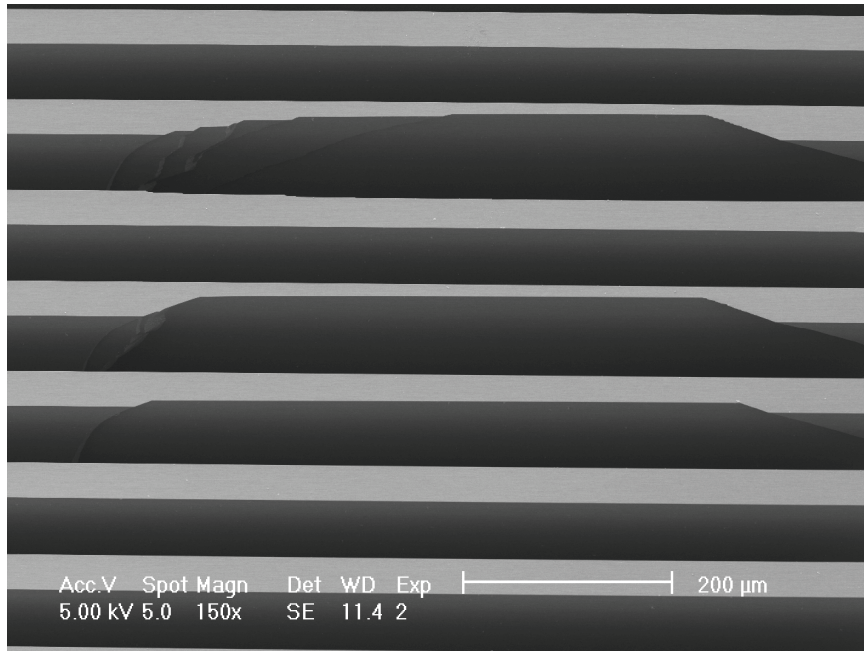
B.2 Distance between Silicon Slots

The silicon area between two silicon slots forms a long supported silicon beam. If the beam is too long, the fluid passing through the slot structure may create an unbalance pressure on the beam and damage the beam due to a large deflection. This is another important reason to divide a long silicon slots into two or more shorter slots.

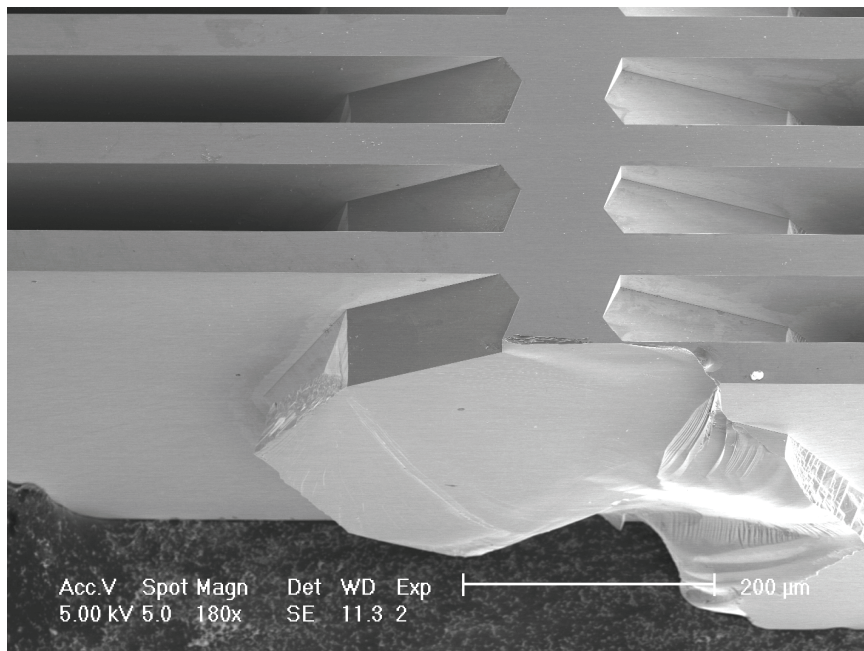
B.3 Etch Results

Preliminary etch results showed that the misalignment between the mask and the crystal orientation was not large enough to affect our pattern (major design geometries are listed in Table 3.1). It is sufficient to cautiously align the mask with the major flat on the (110) wafer in the lithography steps. The successful fabricated silicon slot structure is shown in Fig. 3.11.

Damages were found on the silicon slot structure after a long through-wafer KOH etching. Figure B.2a and B.2b show the SEM photos of partially and completely damaged silicon slot structure. The formation of these damaged silicon slot structures are



(a) Partially damaged structure



(b) Completely damage structure

Figure B.2: SEM of damaged silicon structure after KOH process.

primarily because the etch mask—silicon oxide/nitride layers are damaged or flushed away after a long etch. Pin holes on the oxide/nitride thin film layer are major causes for this. A thicker silicon oxide/nitride layer can be used in a long KOH etching. However,

a thicker mask layer requires a longer etch time for patterning the mask in the previous dry etching step. A long dry etching step may result in photoresist burnt out and consequently damages of the pattern. Furthermore, stress created in the deposition may damage the thin film layers. Careful attention is necessary to determine the thickness of the oxide/nitride etch mask. 8000/2000 Å oxide/nitride layer was used in our final process. As shown in Fig. B.3, limited damages were found in most dies across the wafers after the KOH process. These dies can be used for assembly of a heat exchanger although the heat transfer performance will slightly degrade. As a result, the yield of this KOH step is close to 100%. The edge of the wafer was unavoidably damaged from the side by the KOH solution. However, these damages do not affect the patterns on the silicon wafer.

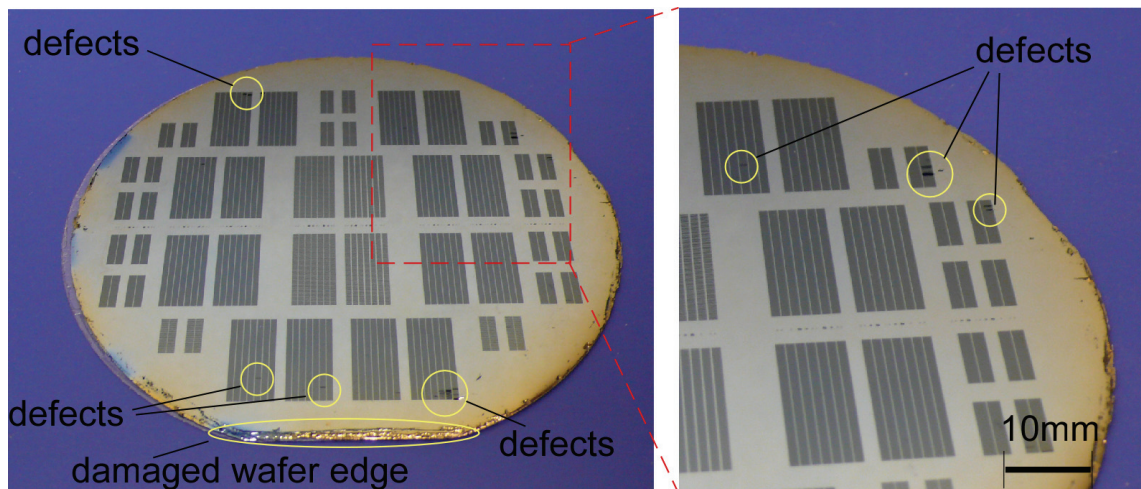


Figure B.3: Damaged silicon defects on a processed four inch wafer after KOH.

SEMs in Fig B.2 also indicate that surfaces on both etched Si sidewalls and the top of wafer covered by oxide/nitride mask are very smooth. Not many pin holes are founded on the top surface. Hence, metal line used for Pt RTDs can be deposited on the top or bottom surface of the silicon wafer.

APPENDIX C

Pressure Drop Test of the Perforated Plate Heat Exchangers

The major disadvantage of the perforated plate heat exchanger is leakage between the silicon plates and glass spacers. Both internal and external leakage may exist. When the external leakage can be easily fixed, internal leakage in the heat exchanger is impossible to repair. As a result, the fluid flows from the high-pressure side of the heat exchanger to the low-pressure side without passing through the gas expansion orifice or valve in the J-T cycle. Furthermore, the pressure drop across the heat exchanger should be minimal to ensure the pressure drop across the expansion orifice/valve and consequently the temperature drop to be maximized.

A simple test facility, as shown in Fig. C.1, is built for a preliminary pressure drop test on the heat exchangers. Previous experiment showed that the pressure drop behaviors with different gases are very similar. Compressed air at room temperature (about 20 °C) was used for this test. The heat exchanger was installed to a U-tube mounted with a VCR fitting in which the gasket can be changed during the pressure test. Mass flow rate, inlet pressure and outlet pressure are measured in the locations illustrated in this figure. Three different gaskets were used in the pressure drop test. First, a blank gasket was used and the flow to the low-pressure side of heat exchanger is blocked. The air can pass through the heat exchanger only there is internal leakage. Second, a gasket

glued with a jewel orifice was used. This is very similar to the self-cooling J-T test. Gas expanded through the orifice and resulted in pressure drop. However, the J-T effect for air was not significant in this test. Third, a through gasket was used while a large amount of air travelled through the gasket without too much pressure drop. This is very similar to the effectiveness test in which the pressure drop only occurs across the heat exchanger.

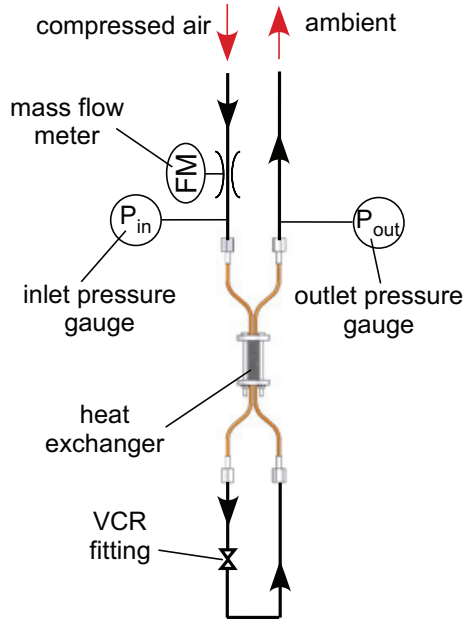


Figure C.1: Schematic diagram of the pressure drop test facility.

Figure C.2 shows the results of the pressure drop test for the 43 die 10 mm heat exchanger presented in Chapter 3. When the blank gasket is used, the mass flow is almost zero. This indicates no internal leakage inside the heat exchanger. The result is consistent to the helium leak test performed on this heat exchanger.

Figure C.3 shows the results of pressure drop test for the 37 die 20 mm heat exchanger presented in Appendix A. The results from the helium leak test and pressure drop test agreed with each other well that the heat exchanger has significant internal leakage. As shown in this figure, the curve for 0.013" orifice is very close to the curve

for blank gasket because there are much more air travelling through the internal leakage of the heat exchanger than through the orifice.

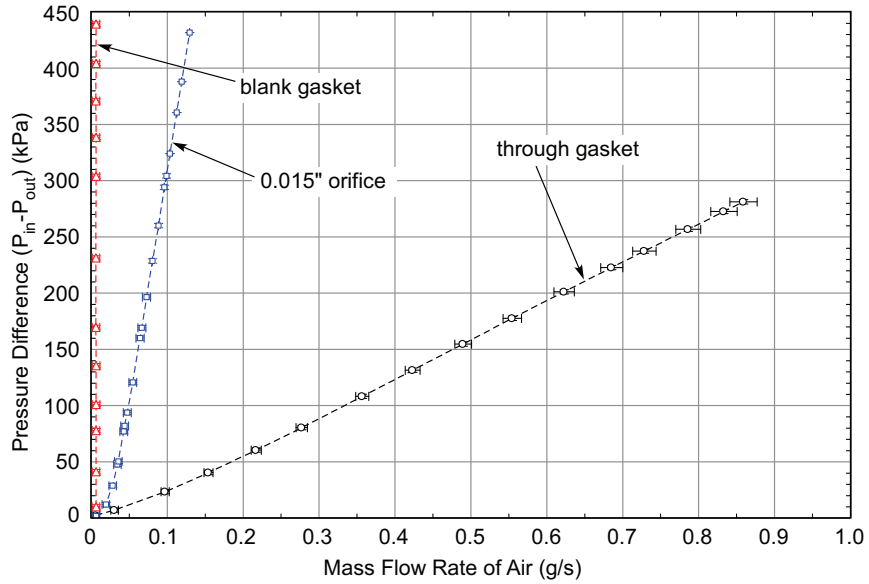


Figure C.2: Pressure drop across the 43 die 10 mm heat exchanger for different configurations.

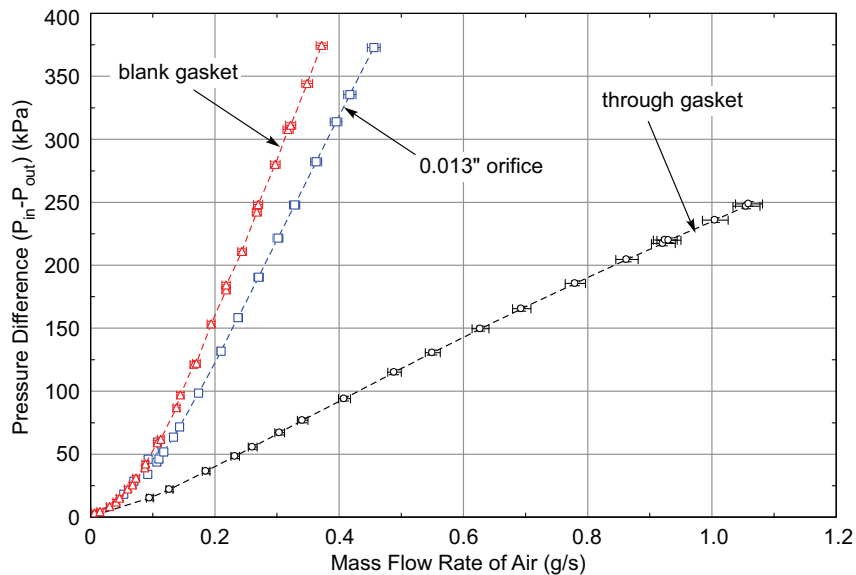


Figure C.3: Pressure drop across the 37 die 20 mm heat exchanger for different configurations.

APPENDIX D

Preliminary Results of a Cryosurgical Instrument Prototype

A cryosurgical probe prototype was designed to implement the heat exchanger and the orifice/microvalve in a J-T cycle. Originally, this prototype is intended for cooling down targets at room temperature. However, due to the heat conduction loss of the system, the temperature cooled down at the probe tip of the setup is not sufficient. Further improvement is required for this prototype. This section describes this prototype and its preliminary experimental results.

D.1 Prototype Setup

The flow scheme of this cryosurgical instrument prototype is very similar to the cryogenic test facility presented in Chapter 3. As shown in Fig. D.1, the dewar is replaced by the cryosurgical probe insulation housing. All other components outside the housing are identical to those in the cryogenic test facility. The insulation is made of stainless steel. Although it is relatively heavy, the housing can withstand a very high pressure if the components inside start to leak during the operation. Ethane is used in our experiments. Figure D.2 shows the schematic diagram inside the insulation housing. The flow scheme is very similar to the J-T self-cooling test. A microvalve and a VCR fitting for installing jewel orifice are connected in parallel. Both can be used for gas expansion

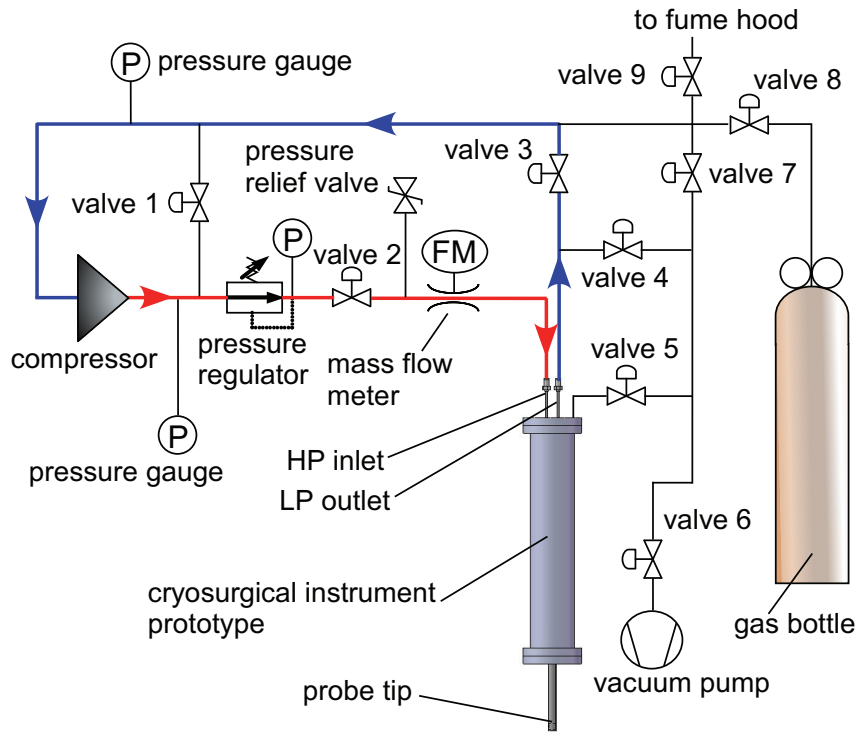


Figure D.1: Schematic diagram of the cryosurgical instrument prototype.

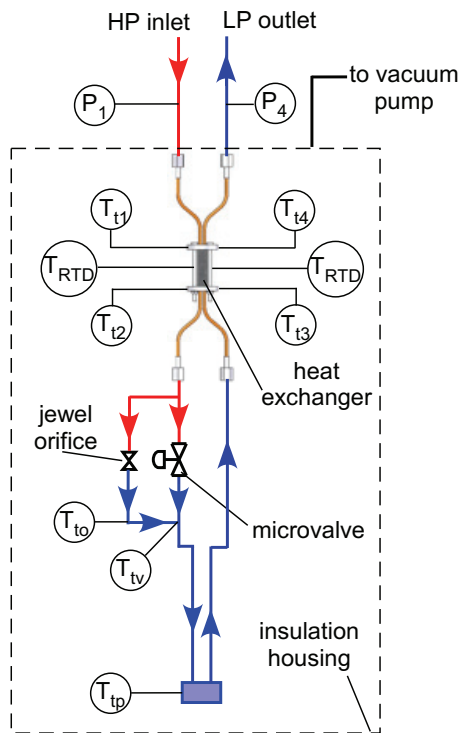


Figure D.2: Schematic diagram inside the insulation housing.

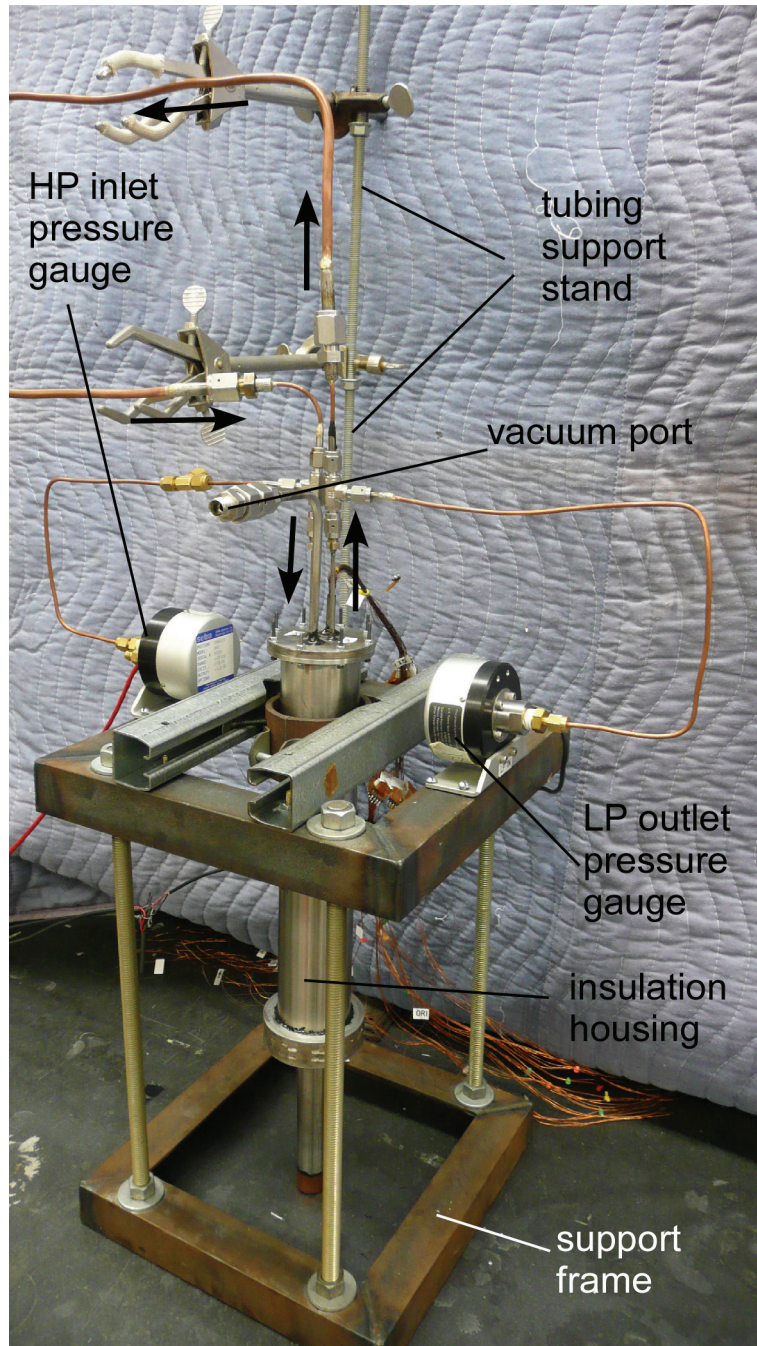


Figure D.3: Photograph of cryosurgical instrument prototype setup (at UW-Madison).

and thus produce J-T effect. When the microvalve is used to modulate the flow, a blank gasket can be installed into the VCR fitting and block the flow in its path. Similarly, when an orifice is desired, the microvalve can be removed. Since the heat load will be on the tool tip, no extra heater is necessary in this setup. The thermocouples are inserted

into the tubing and heat exchanger headers to precisely measure the temperature of the flow. The pressure inside the housing is vacuumed down to the mTorr range for a thermal insulation during the experiment.

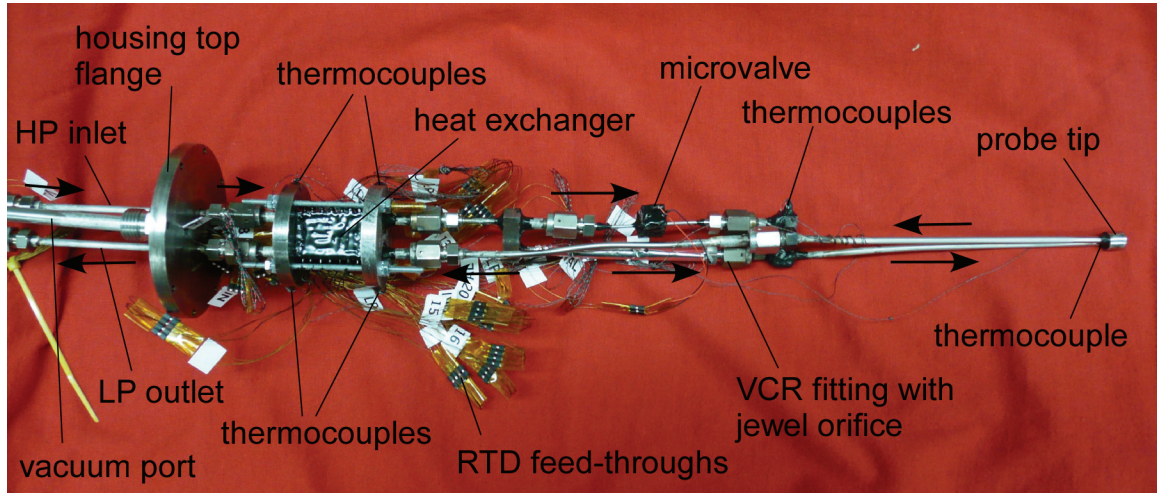


Figure D.4: Photograph of the cryosurgical instrument inside insulation housing (at UW-Madison).

Figure D.4 shows a photograph of the cryosurgical instrument inside the housing. The structure is very compact in order to enable future development of a portable cryosurgical probe. The diameter of the entire housing is about 3 inch and the length is about 12 inch. In our preliminary test, the tool tip is enclosed inside the housing with vacuum insulation.

D.2 Experimental Results

This section only discusses the experimental result obtained from the 43 die 10 mm heat exchanger. The prototype was tested with three different orifice diameters (0.010", 0.013", 0.015") and the piezoelectric microvalve with input voltage from -30 V to 100 V. As shown in Fig. D.5, the optimal orifice is 0.015" since the cooling temperature reaches lowest when the pressure difference is the same. However, the cooling temperature at the

tool tip is much smaller than the results obtained from the cryogenic test facility because of large heat conduction between the inner tubing and housing. The tubing was designed not to have any contact with the insulation housing such that the heat conduction is eliminated at the cold end in vacuum. In reality, due to the fabrication limits, the tubing cannot be adjusted to the desired angle and consequently touches the housing at certain locations. As a result, the heat conduction loss dominated and the J-T system cannot be cooled down to a low temperature.

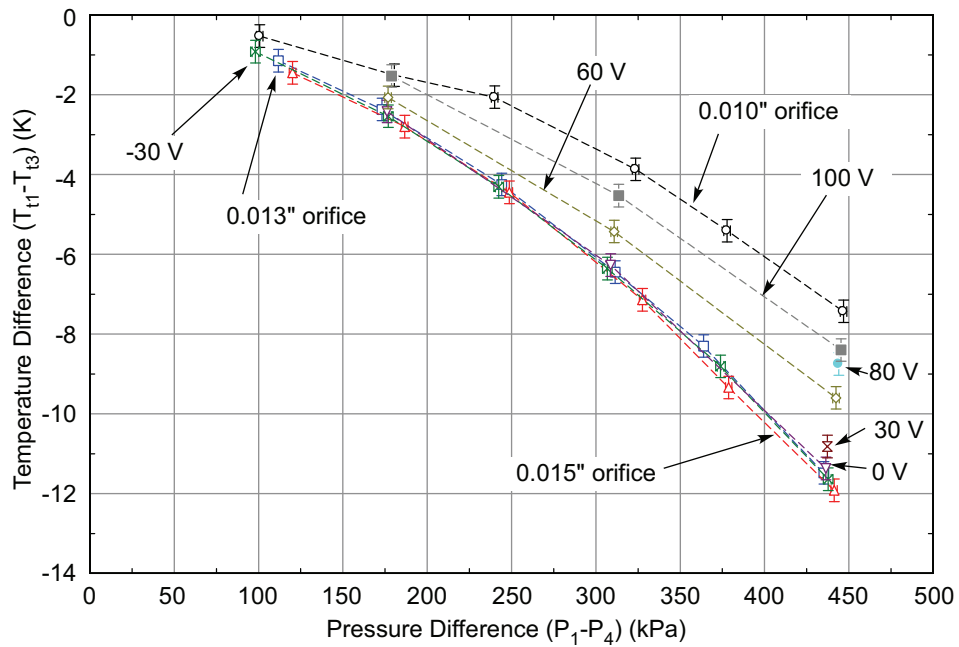


Figure D.5: Self-cooling test of the cryosurgical instrument prototype with different orifices and microvalve input voltages.

The effectiveness of the heat exchanger is also calculated based on the inlet and outlet temperatures (Fig. D.6). The results are slightly larger than the results reported in Chapter 3. However, as mentioned before, a smaller temperature difference will result in larger uncertainties of measurements.

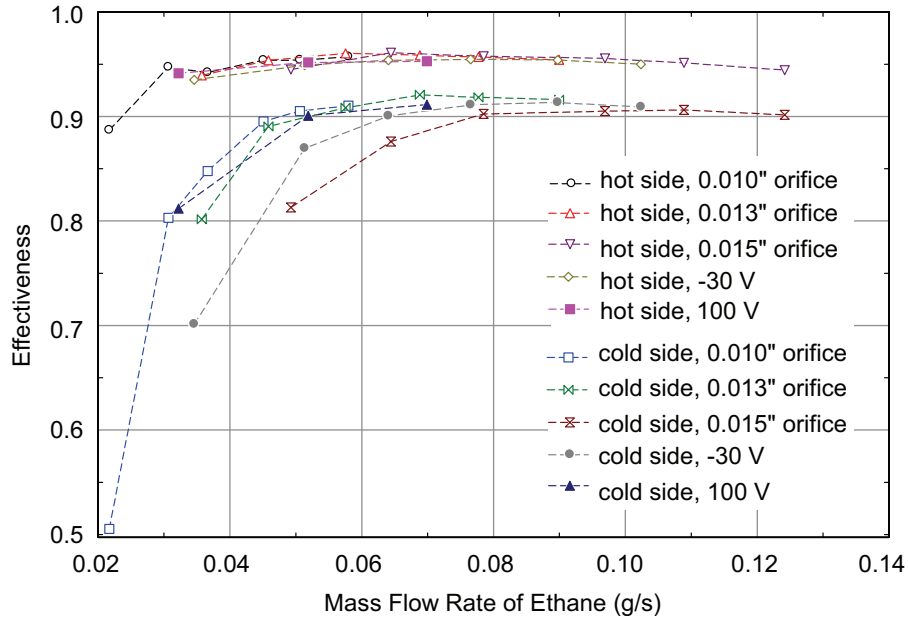


Figure D.6: Effectiveness measurement of the cryosurgical instrument prototype with different orifice size and microvalve input voltage.

D.3 Discussion

A cryosurgical instrument prototype that integrates the perforated plate heat exchanger, the jewel orifice and the microvalve was built. Comprehensive experiments on this prototype were completed. The effectiveness of heat exchanger was calculated and matched up with the experimental results obtained from the cryogenic test facility presented in Chapter 3. Due to the large heat conduction loss between the inner tubing and housing, the temperature of the probe tip did not reach a desired temperature. Further improvements to reduce the heat conduction loss are necessary.

APPENDIX E

List of Publications Related to This Dissertation

W. Zhu, M. J. White, G. F. Nellis, S. A. Klein, and Y. B. Gianchandani, "A Perforated Plate Stacked Si/Glass Heat Exchanger with In-situ Temperature Sensing for Joule-Thomson Coolers," *Proc. IEEE MEMS*, Tucson, Arizona, USA, pp. 844-847, Jan 2008.

W. Zhu, M. J. White, D. W. Hoch, G. F. Nellis, S. A. Klein, and Y. B. Gianchandani, "Two Approaches to Micromachining Si Heat Exchangers for Joule-Thomson Cryosurgical Probes," *Proc. IEEE MEMS*, Kobe, Japan, pp. 317-320, Jan 2007.

W. Zhu, D. W. Hoch, G. F. Nellis, S. A. Klein, and Y. B. Gianchandani, "A Planar Glass/Si Micromachining Process for the Heat Exchanger in a J-T Cryosurgical Probe," *Proc. Solid State Sensors, Actuators and Microsystems Workshop*, Hilton Head, pp.51-55, 2006.

W. Zhu, Yogesh B. Gianchandani, Gregory F. Nellis, Sanford A. Klein, "Micromachined Heat Exchanger for a Cryosurgical Probe," *International Workshop on Thermal Investigations of ICs and Systems (THERMINIC'05)*, Belgirate, Italy, pp. 112-116, September 2005.

M.J. White, W. Zhu, G.F. Nellis, S.A. Klein and Y.B. Gianchandani, "Performance of a MEMS Heat Exchanger for a Cryosurgical Probe," *Proc. the 15th International Cryocoolers Conference*, to be published, Long Beach, California, 2008.

D. W. Hoch, W. Zhu, G. F. Nellis, S. D. Schuetter, S. A. Klein, and Y. B. Gianchandani, "Progress Towards a Micromachined Heat Exchanger for a Cryosurgical Probe," *Proc. the 14th International Cryocoolers Conference*, pp. 505-514, Annapolis, Maryland, 2006.

BIBLIOGRAPHY

- [Alf74] V. N. Alfeev. et al., Great Britain Patent # 1,336,892, 1974.
- [Bar99] R. F. Barron, *Cryogenic Heat Transfer*, Taylor & Francis, 1999.
- [Bis93] J. Bischoff, K. Christov, and B. A. Rubinsky, "Morphological Study of Cooling Response in Normal and Neoplastic Human Liver Tissue: Cryosurgical Implications," *Cryobiology*, 30, pp. 482-492, 1993.
- [Boi98] M. Boiarski, A. Khatri and V. Kovalenko, "Design Optimization of the Throttle-Cycle Cooler with Mixed Refrigerant", *Cryocoolers* 10, pp. 457-465, Kluwer Academy: New York, 1998.
- [Bra02] H. J. M. ter Brake and G. F. M. Wiegerinck, "Low-Power Cryocooler Survey," *Cryogenics*, vol. 42, pp. 705-718, 2002.
- [Bra08] P. E. Bradley, R. Radebaugh, M. Huber, M.-H. Lin, and Y. C. Lee, "Development of a Mixed-Refrigerant Joule-Thomson Microcryocooler," *Proc. the 15th International Cryocoolers Conference*, to be published, Long Beach, California, 2008.
- [Bru99] J. L. Bruning, R. Torrison, R. Radebaugh, and M. Nisenoff, "Survey of Cryocoolers for Electronic Applications (C-SEA)," *Cryocoolers 10*. New York: Plenum, pp. 829–835, 1999.
- [Bur01] J. Burger, H. Holland, E. Berenschot, J.-H. Seppenwoolde, M. ter Brake, H. Gardeniers, and M. Elwenspoek, "169 Kelvin Cryogenic Microcooler Employing a Condenser, Evaporator, Flow Restriction and Counterflow Heat Exchangers" *Proc. IEEE MEMS*, pp. 418-421, 2001.
- [Bur01a] J. Burger, H. Holland, J. Seppenwoolde, E. Berenschot, H. ter Brake, J. Gardeniers, M. Elwenspoek and H. Rogalla, "165 K Microcooler Operating with a Sorption Compressor and a Micromachined Cold Stage," *Cryocoolers*, vol 11, Kluwer Academic/Plenum, New York, pp 551–560, 2001
- [Cha93] Z. H. Chang, J. J. Finkelstein, J. G. Baust, "Optimization of Cryosurgical Instrumentation for use in Minimally Invasive Prostate Surgery," *ASME Heat Transfer Div Publ HTD*, v 267, pp. 45-55, 1993.

- [Cha00] M. Chabloz, J. Jiao, Y. Yoshida, T. Matsuura, K. Tsutsumi, "A Method to Evade Microloading Effect in Deep Reactive Ion Etching for Anodically Bonded Glass-silicon Structures," *IEEE Intl. Conf. on Micro Electro Mechanical Systems (MEMS'00)*, Miyazaki, Japan, pp. 283-287, 2000.
- [Chi99] F. S.-S. Chien, C.-L. Wu, Y.-C. Chou, T. T. Chen, S. Gwob, and W.-F. Hsieh, "Nanomachining of (110)-Oriented Silicon by Scanning Probe Lithography and Anisotropic Wet Etching," *Applied Physics Letters*, vol. 75, no. 16, pp. 2429-2431, Oct. 1999.
- [Coh94] J. K. Cohen, R. J. Miller, "Thermal Protection of Urethra during Cryosurgery of the Prostate," *Cryobiology*, 31, pp. 313-316, 1994.
- [Col00] B. Collaudin and N. Rando, "Cryogenics in Space: a Review of the Missions and of the Technologies," *Cryogenics*, vol. 40, pp. 797-819, 2000.
- [Coo01] Cooper, S.M., "The History of Cryosurgery," *Journal of the Royal Society of Medicine*, Vol. 94, April, pp. 196-201, 2001.
- [Dob94] J. Dobak, X. Yu, and K. Ghaerzadeh, "A Novel Closed Loop Cryosurgical Device," *Advances in Cryogenic Engineering*, 43, pp. 897-902, 1998
- [Dob98] J. Dobak, "A Review of Cryobiology and Cryosurgery," *Advances in Cryogenic Engineering*, 43, pp. 889-896, 1998.
- [Dob98a] J. Dobak, X. Yu and K. Ghaerzadeh, "A Novel Closed Loop Cryosurgical Device," *Advances in Cryogenic Engineering*, 43, pp. 897-902, 1998.
- [Esa90] M. Esashi and S. Shoji, "Photoetching and Electrochemical Discharge Drilling of Pyrex Glass," *Technical Digest of the 9th Sensor Symposium*, pp. 27-30, 1990
- [Fas99] V. Fascio, R. Wüthrich, D. Viquerat, H. Langen, "3D Microstructuring of Glass Using Electrochemical Discharge Machining (ECDM)," *International Symposium on Micromechatronics and Human Science*, pp. 179-183, 1999.
- [Fra04] M. Frank, *Recuperative Heat Exchanger for a MEMS Cryoprobe*, M.S. Thesis, Univ. Wisconsin, Dept. of Mechanical Engineering, 2004.
- [Fre04] K. Fredrickson, *Optimization of Cryosurgical Probes for Cancer Treatment*, M.S. Thesis, Univ. Wisconsin, Dept. of Mechanical Engineering, 2004.
- [Fu03] C. Fu, Z. Rummler and W. Schomburg, "Magnetically driven micro ball valves fabricated by multilayer adhesive film bonding," *J. Micromech. Microeng.*, 13, S96-102, 2003.
- [Gag76] A. Gage, "Five-year Survival Following Cryosurgery for Oral Cancer," *Archives of Surgery*, 111, pp. 990-994, 1976.

- [Gag82] A. Gage, J. A. Caruana and M. Montes, "Critical Temperature for Skin Necrosis in Experimental Cryosurgery," *Cryobiology*, 19, pp. 273-282, 1982.
- [Gag85] A. Gage, K. Guest, M. Montes, A. Caruana and D. A. Whalen, "Effect of Varying Freezing and Thawing Rates in Experimental Cryosurgery," *Cryobiology*, Vol. 22, pp. 175-182, 1985.
- [Gag92] A. A. Gage, "Cryosurgery in the Treatment of Cancer," *Surgery, Gynecology & Obstetrics*, 174, pp. 73-92, 1992.
- [Gag98] A., Gage, "History of Cryosurgery," *Seminars in Surgical Oncology*, vol. 14, pp. 99-109, Wiley-Liss, Inc., 1998.
- [Gar83] S. Garvey, S. Logan, R. Rowe, and W. A. Little, "Performance Characteristics of a Low-Flow Rate 25 mW, LN2 Joule-Thomson Refrigerator Fabricated by Photolithographic Means," *Applied Physics Letter*, vol. 42, no. 12, pp. 1048-1050, 1983.
- [Gav83] S. Garvey, S. Logan, R. Rowe, and W. A. Little, "Performance Characteristics of a Low-Flow Rate 25 mW, LN2 Joule-Thomson Refrigerator Fabricated by Photolithographic Means," *Applied Physics Letter*, vol. 42, no. 12, pp. 1048-1050, 1983.
- [Gni76] V. Gnielinski, "Equations for Heat and Mass Transfer in Turbulent Pipe and Channel Flow," *Int. Chem. Eng.*, Vol. 16, pp. 359-368, 1976.
- [Gon04] M. Q. Gong, J. F. Wu and E. G. Luo, "Performances of the Mixed-Gases Joule-Thomson Refrigeration Cycles for Cooling Fixed-Temperature Heat Loads," *Cryogenics*, vol. 44, pp. 847-857, Dec. 2004.
- [Ham93] A. Hamilton, and J. Hu, "An Electronic Cryoprobe for Cryosurgery Using Heat Pipes and Thermoelectric Coolers: a Preliminary Report," *J. Med Eng Tech.*, 17(3), pp. 104-109, May-Jun 1993.
- [Hoc06] D. W. Hoch, W. Zhu, G. F. Nellis, S. D. Schuetter, S. A. Klein, and Y. B. Gianchandani, "Progress Towards a Micromachined Heat Exchanger for a Cryosurgical Probe," *Proc. the 14th International Cryocoolers Conference*, pp. 505-514, Annapolis, Maryland, 2006.
- [Ike97] T. Ikehara, H. Yamagishi, and K. Ikeda, "Electromagnetically driven silicon microvalve for large-flow pneumatic Controls," *Proc. SPIE—The Int. Soc. Opt. Eng.* 3242, pp. 136-44, 1997.
- [Inc96] F. P. Incropera and D. P. DeWitt, *Fundamentals of Heat and Mass Transfer*, 4th ed., Wiley, New York, 1996.

- [Ish99] K. Ishihara, C. F. Tung, A. A. Ayón, “An Inertial Sensor Technology Using DRIE and Wafer Bonding with Interconnecting Capability,” *J. Micromech. Sys.*, 8 (4), pp. 403-408, 1999.
- [Kak87] S. Kakac, R. K. Shah, W. Aung, *Handbook of Single-Phase Convective Heat Transfer*, John Wiley & Sons, 1987
- [Kan90] Y. Kanda, K. Matsuda, C. Murayama, J. Sugaya, “The Mechanism of Field-Assisted Silicon-Glass Bonding,” *Sensors and Actuators A (Physical)*, vol. 23, no. 1-3, pp. 939-943, 1990.
- [Kep04] F. Keppler, G. Nellis, and S. Klein, “Optimization of the Composition of a Gas Mixture in a Joule-Thomson Cycle,” *International Journal of Heating, Ventilation, Air Conditioning, and Refrigeration Research*, Vol. 10, No. 2, pp. 213-230, 2004.
- [Kla00] M. Klauda, T. Kässer, B. Mayer, C. Neumann, F. Schnell, B. Aminov, A. Baumfalk, H. Chaloupka, S. Kolesov, H. Piel, N. Klein, S. Schornstein and M. Bareiss, “Superconductors and Cryogenics for Future Communication Systems,” *IEEE Transactions on Microwave Theory and Techniques*, vol. 48, no. 7, July 2000.
- [Kle59] A. P. Kleemenko, “One Flow Cascade Cycle,” *Proceedings of the Xth International Congress on Refrigeration*, Copenhagen, 1, pp. 34-39, London: Pergamon Press, 1959.
- [Kle02] S.A. Klein and F.L.Alvarado, EES-Engineering Equation Solver, *F-Chart Software*, <http://www.fchart.com>, 2002.
- [Küh98] K. Kühn, S. Vogel, U. Schaber, R. Schafflik, B. Hillerich, “Advanced Silicon Trench Etching in MEMS Applications,” *SPIE*, vol. 3511, Santa Clara, California, pp. 97-105, 1998.
- [Lee87] W. Y. Lee, F. Sequeda, J. Salem, D. Chapman, “Field-Assisted Bonding below 200°C Using Metal and Glass Thin-Film Interlayers,” *Applied Physics Letters*, vol. 50, no. 9, pp. 522-524, 1987.
- [Ler06] P. Lerou, G. Venhorst, C. Berends, T. Veenstra, M. Blom, J. Burger, H. ter Brake and H. Rogalla, “Fabrication of a Micro Cryogenic Cold Stage Using MEMS-Technology,” *J. Micromech. Microeng.* 16, pp.1919–1925, 2006.
- [Ler07] P. P. P. M. Lerou, H. J. M. Ter Brake, J. F. Burger, H. J. Holland, and H. Rogalla, “Characterization of Micromachined Cryogenic Coolers,” *Journal of Micromechanics and Microengineering*, vol. 17, no. 10, pp. 1956-1960, Oct 2007.

- [Ler07a] P. Lerou, H. Ter Brake, H. Holland, J. Burger and H. Rogalla. "Insight into Clogging of Micromachined Cryogenic Coolers" *Applied Physics Letters*, vol. 90, no. 6, pp 064102, 2007.
- [Lit97] W. A. Little, Method for Efficient Countercurrent Heat Exchange Using Optimized Mixtures, US Patent #5,644,592, 1997.
- [Lit82] W. A. Little, "Microminiature Refrigeration-Small is Better," *Physica 109 & 110B*, pp. 2001-2009, 1982.
- [Lit88] W. A. Little, "Recent Developments in Joule-Thomson Cooling: Gases Coolers and Compressors", *Proceeding of the 5th International Cryocoolers Conference*, pp. 3-11., 1988
- [Luo00] E. C. Luo, M. Q. Gong, Y. Zhou, J. T. Liang and L. Zhang, "The Research and Development of Cryogenic Mixed-Refrigerant Joule-Thomson Cryocoolers in CL/CAS", *Advances in Cryogenic Engineering*, Vol. 45 Part A, pp. 299-306, Kluwer Press: New York, 2000.
- [Mad97] M. Madou, *Fundamentals of Microfabrication*, CRC Press, Boca Raton, 1997.
- [Mar98] E.D. Marquardt, R. Radebaugh and J. Dobak, "A Cryogenic Catheter for Treating Heart Arrhythmia," *Advances in Cryogenic Engineering*, 43, pp. 903-910, 1998.
- [Mat92] R. Matsumoto, K. Oshio and F. Jolesz, "Monitoring of Laser and Freezing-Induced Ablation in the Liver with T1-Weighted MR Imaging," *Journal of Magnetic Resonance Imaging*, Vol. 2, pp. 555-562, 1992.
- [May98] B. Z. Maytal, "Fast Joule-Thomson Cryocycling Device for Cryosurgical Applications," *Advances in Cryogenic Engineering*, 43, pp.911-917, 1998.
- [McK70] A. K. McKurdy, H. J. Maris and C. Elbaum, "Anisotropic Heat Conduction in Cubic Crystals in the Boundary Scattering Regime," *Physical Review B*, Vol. 2, No.10, 1970.
- [Mil76] R. Miller and P. Mazur, "Survival of Frozen-Thawed Human Red Cells as a Function of Cooling and Warming Velocities" *Cryobiology*, Vol. 13, pp. 404-414, 1976.
- [Mit05] J. Mitchell, G. R. Lahiji, K. Najafi, "Encapsulation of Vacuum Sensors in a Wafer Level Package Using a Gold-Silicon Eutectic," *Transducers'05*, vol. 1, pp.928-931, June 2005.
- [Mmr08] MMR technologies Inc., <http://www.MMR.com/>, 2008.

- [Nel03] G. F. Nellis, "A Heat Exchanger Model that Includes Axial Conduction, Parasitic Heat Loads, and Property Variations," *Cryogenics*, vol. 43, pp. 523-538, 2003.
- [Nel05] G. F. Nellis, C. B. Hughes and J. M. Pfothenhauer, "Heat Transfer Coefficient Measurements for Mixed Gas Working Fluids at Cryogenic Temperatures," *Cryogenics*, Vol. 45, No. 8, pp. 546-556, August, 2005.
- [Nel06] G. F. Nellis and S. A. Klein, "Approximate Solution for Rectangular Fins in Contact with Flowing Fluid," *UW-Madison Internal Technical Report*, 2006
- [Oni84] G. Onik, C. Cooper, H. I. Goldberg, A. A. Moss, B. Rubinsky and M. Christianson, "Ultrasonic Characteristics of Frozen Liver," *Cryobiology*, Vol. 21, pp 321-328, 1984.
- [Par06] M. J. Park, R. P. Taylor, A. T. Evans, T. R. Brosten, G. F. Nellis, S. A. Klein, J. R. Feller, L. Salerno and Y. B. Gianchandani, "A Piezoelectrically Actuated Ceramic-Si-Glass Microvalve for Distributed Cooling Systems," *Solid-State Sensor and Actuator Workshop (Hilton Head '06)*, Hilton Head Island, South Carolina, pp 248-51, June 2006.
- [Par07] J. M. Park, T. R. Brosten, A. T. Evans, K. Rasmussen, G. F. Nellis, S. A. Klein, J. R. Feller, L. Salerno and Y. B. Gianchandani, "A Piezoelectric Microvalve with Integrated Sensors for Cryogenic Applications," *Proc. of the IEEE MEMS'07*, Kobe, Japan, p 647-650, 2007.
- [Par08] J. M. Park, R. P. Taylor, A. T. Evans, T. R. Brosten, G. F. Nellis, S. A. Klein, J. R. Feller, L. Salerno and Y. B. Gianchandani, "A Piezoelectric Microvalve for Cryogenic Applications," *J. Micromech. Microeng.*, v 18, n 1, p 015023 (10 pp.), Jan. 2008.
- [Pea95] G. Pease, S. Wong, M. Roos and B. Rubinsky, "MR Image-Guided Control of Cryosurgery", *Journal of Magnetic Resonance Imaging*, Vol. 5, pp. 753-760, 1995.
- [Pet70] B. S. Pethukhov, T. F. Irvine and J. P. Hartnett, *Advances in Heat Transfer*, Vol. 6, Academic Press, NY, 1970.
- [Qi05] S. L. Qi, P. Zhang, A. L. Zhang, R. Z. Wang and L. X. Xu., "Performance Evaluation of a Novel Liquid Nitrogen Cryoprobe," *Prof. of the 2005 IEEE Engineering in Medicine and Biology 27th Annual Conference*, Shanghai, China, pp. 486-389, Sep 2005.
- [Rad04] R. Radebaugh, "Refrigeration for Superconductors," *Proc. IEEE, Special Issue on Applications of Superconductivity*, vol. 92, pp. 1719-1734, 2004.
- [Roh98] W. M. Rohsenow, J. P. Hartnett and Y. I. Cho, *Handbook of Heat Transfer*, McGraw-Hill, New York, 1998.

- [Rub93] B. Rubinsky, J. C. Gilbert, G.M. Onik, M.S. Roos, S.T. Wong, K.M. Brennan, "Monitoring Cryosurgery in the Brain and Prostate with Proton NMR," *Cryobiology*, 30, pp. 191-199, 1993.
- [Sal95] J. C. Saliken, J. Cohen, R. Miller and M. Rothert, "Laboratory Evaluation of Ice Formation around a 3-mm AccuProbe," *Cryobiology*, Vol. 32, pp. 285-295, 1995.
- [Sel01] J. C. Selby, M. L. Philpott, M. A. Shannon, "Fabrication of Mesoscopic, Flexible, High Pressure, Microchannel Heat Exchangers (MHEX)," *Trans of NAMRI/SME*, Vol. 29, pp. 469-476, 2001.
- [Sha78] R. K Shah and A. L. London, "Laminar Flow Forced Convection in Ducts", *Supplement 1 to Advances in Heat Transfer*, New York: Academic Press, 1978.
- [Shi97] Y. Shinozawa, T. Abe and T. Kondo "A proportional microvalve using a bistable magnetic actuator," *IEEE Int. Workshop on Micro Electro Mechanical Systems (MEMS '97)*, Nagoya, Japan, pp 233-7, January 1997.
- [Sky09] Private conversation with Harrison Skye and Gregory Nellis, 2009.
- [Ter79] S. C. Terry, J. H. Jerman and J. B. Angell, "A gas chromatographic air analyzer fabricated on a silicon wafer," *IEEE Trans. Electron Dev. ED-26*, pp. 1880-6, 1979.
- [Tor75] D., Torre, "Alternate Cryogens of Cryosurgery," *Journal of Dermatological Surgery*, Vol. 1, pp. 56-58, 1975.
- [Tou70] Y. S. Touloukian, R. W. Powell, C.Y. Ho and P. G. Klemens, "Thermophysical Properties of Matter Volume 1: Thermal Conductivity-Metallic Elements and Alloys," *IFI/Plenum*, 1970.
- [Uni08] University of Wisconsin-Madison General Surgery Website, <http://www.surgery.wisc.edu/general/patients/uwmhpscryo.shtml>, 2008
- [Whi08] M.J. White, W. Zhu, G.F. Nellis, S.A. Klein and Y.B. Gianchandani, "Performance of a MEMS Heat Exchanger for a Cryosurgical Probe," *Proc. the 15th International Cryocoolers Conference*, to be published, Long Beach, California, 2008.
- [Whi08a] M. J. White, *Performance of a MEMS Heat Exchanger for a Cryosurgical Probe*, M.S. Thesis, University of Wisconsin-Madison, 2008.
- [Wol94] R. F. Wolffenbuttel and K. D. Wise, "Low Temperature Silicon Wafer-to-Wafer Bonding Using Gold at Eutectic Temperature," *Sensors and Actuators*, vol. A43, pp.223-229, 1994.

- [Wüt05] R. Wüthrich and V. Fascio, “Machining of Non-Conducting Materials Using Electrochemical Discharge Phenomenon—an Overview,” *International Journal of Machine Tools & Manufacture*, 45, pp. 1095-1108, 2005
- [Zhu05] W. Zhu, Yogesh B. Gianchandani, Gregory F. Nellis, Sanford A. Klein, “Micromachined Heat Exchanger for a Cryosurgical Probe,” *International Workshop on Thermal Investigations of ICs and Systems (THERMINIC’05)*, Belgirate, Italy, pp. 112-116, September 2005.
- [Zhu06] W. Zhu, D. W. Hoch, G. F. Nellis, S. A. Klein, and Y. B. Gianchandani, “A Planar Glass/Si Micromachining Process for the Heat Exchanger in a J-T Cryosurgical Probe,” *Proc. Solid State Sensors, Actuators and Microsystems Workshop*, Hilton Head, pp.51-55, 2006.
- [Zhu07] W. Zhu, M. J. White, D. W. Hoch, G. F. Nellis, S. A. Klein, and Y. B. Gianchandani, “Two Approaches to Micromachining Si Heat Exchangers for Joule-Thomson Cryosurgical Probes,” *Proc. IEEE MEMS*, Kobe, Japan, pp. 317-320, Jan 2007.
- [Zhu08] W. Zhu, M. J. White, G. F. Nellis, S. A. Klein, and Y. B. Gianchandani, “A Perforated Plate Stacked Si/Glass Heat Exchanger with In-situ Temperature Sensing for Joule-Thomson Coolers,” *Proc. IEEE MEMS*, Tucson, Arizona, USA, pp. 844-847, Jan 2008.